[Catégorie]

ETUDE DE FAISABILITE D'UTILISER DES DONNEES SAR ET RADAR HF POUR LE CALCUL DE TOPOGRAPHIES DYNAMIQUES MOYENNES REGIONALES

Référence :	CLS-DOS-NT-2014-196
Nomenclature :	-
Version :	1. 0
Date :	**03/11/2014**

Aucune partie de ce document ne peut être reproduite sous quelque forme que ce soit,
ni communiquée, ni utilisée, sans l'accord préalable de CLS.

Historique des versions :			
Version :	Date :	Objet :	Auteur
1-0	03/11/2014	Création du document	M-H Rio C. Dufau R. Husson

Acteurs de la présente version :		
Rédigé par (*) :	M-H Rio C. Dufau R. Husson	Date + Signature:(visa ou réf)
Approuvé par (*) :		Date + Signature:(visa ou réf)
Application autorisée par (*) :		Date + Signature:(visa ou réf)

**Dans la case ci-contre : Nom et prénom de la personne + de l'organisme si différent de CLS*

Analyse documentaire :	
Situation du document :	
Mots-clés :	[Mots clés]
Liens hypertexte :	

Liste de diffusion :		
Organisme	Format de diffusion	Destinataires
CLS	Notification	Gilles Larnicol Gérald Dibarboure
CNES	Fichier éléctronique	Emilie Bronner Nicolas Picot Amandine Guillot

Aucune partie de ce document ne peut être reproduite sous quelque forme que ce soit, ni communiquée, ni utilisée, sans l'accord préalable de CLS.

Liste des tableaux et figures

Liste des figures :

Aucune partie de ce document ne peut être reproduite sous quelque forme que ce soit,
ni communiquée, ni utilisée, sans l'accord préalable de CLS.

Aucune partie de ce document ne peut être reproduite sous quelque forme que ce soit,
ni communiquée, ni utilisée, sans l'accord préalable de CLS.

Aucune partie de ce document ne peut être reproduite sous quelque forme que ce soit,
ni communiquée, ni utilisée, sans l'accord préalable de CLS.

Liste des documents de référence

DR 1 Elaboration d'une nouvelle Topographie Dynamique Moyenne Globale. Proposition de CLS en réponse à la consultation N°DA0010089945

DR 2 Elaboration d'une nouvelle Topographie Dynamique Moyenne Globale. Rapport final. Note technique CLS-DOS-NT-2013-243.

DR 3 ETUDE DE FAISABILITE D'UTILISER DES DONNEES SAR ET RADAR HF POUR LE CALCUL DE TOPOGRAPHIES DYNAMIQUES MOYENNES REGIONALES

DR 4 Computation of a new Mean Dynamic Topography for the Mediterranean Sea from model outputs, altimeter measurements and oceanographic in-situ data. Final Report. Note technique CLS-DOS-NT-2012-96.

Aucune partie de ce document ne peut être reproduite sous quelque forme que ce soit, ni communiquée, ni utilisée, sans l'accord préalable de CLS.

Sommaire

Aucune partie de ce document ne peut être reproduite sous quelque forme que ce soit,
ni communiquée, ni utilisée, sans l'accord préalable de CLS.

Aucune partie de ce document ne peut être reproduite sous quelque forme que ce soit,
ni communiquée, ni utilisée, sans l'accord préalable de CLS.

SUMMARY

The feasibility of using HF-radar velocities and SAR Doppler velocities to improve regionally the ocean Mean Dynamic Topography has been investigated.

The MDT calculation method from Rio et al (2014) implies that mean geostrophic velocities are extracted from the measured velocities. This implies removing the ageostrophic current components and the time variable current (relative to the 1993-2012 reference time period).

A careful analysis has therefore been done of the ageostrophic signal contained in the velocities measured by HF radar and spaceborne SAR.

HF-radar measured velocities are quite consistent with drifting buoy velocities, already used for the CNES-CLS13 MDT calculation. They contain the geostrophic current component as well as the tidal currents, the inertial currents, the Ekman currents, and part of the Stokes drift. However, the Eulerian character of the measurement makes it much easier to remove some of these ageostrophic components (namely the inertial oscillations and the tidal currents) than for the Lagrangian drifter velocities. Indeed, for drifters, a 3 days low pass filter is applied along the drifter trajectory, that also acts as a spatial filter. In the case of HF radar velocities, a simple temporal averaging of the hourly values at each point removes these ageostrophic components from the mean. Ekman and Stokes drift components can then be removed using the model by Rio et al (2014), that works reasonably well over the MAB area even though improvements could be made in the future.

Regarding the SAR velocities, the processing applied to retrieve the surface currents remove all wind/wave driven components of the current, including the Ekman currents and the Stokes drift. Tidal currents and inertial oscillations however are contained in the measured SAR velocities, and cannot be filtered out since the temporal resolution of SAR images is only 2-3 days. These signal should therefore be modelled and removed (feasible for tidal currents, more complicated for inertial oscillations), or their variance should be accounted for in the error calculation.

A second issue that has been investigated is the capability of using altimeter velocity anomalies to remove the temporal variability from the observed means. While the method is reasonably efficient in the Agulhas Current, it is problematic in the MAB area, and this definitively calls for improved high resolution coastal altimetry. Meanwhile, accurate prescription of the induced error on the calculated mean should be done.

In case of both HF radar and SAR system, measured velocities are in the system range direction, and only the combination of two range velocities (ideally perpendicular) can give the zonal and meridional components of the total current. In the case of HF radar coastal systems, systems have been designed to cope for this, and in some part of the covered area the total velocity can be reasonably calculated. In other parts higher errors should be prescribed. They depend on the system geometry and are therefore known. The situation is more complicated for SAR velocities. Radial velocities from ENVISAT ascending and descending paths may be combined to reconstruct the total current vector. However, both paths are obviously not simultaneous, which prevents from reconstructing instantaneous velocity vectors from SAR data. The objective being to reconstruct mean currents, mean radial velocities can be estimated from ascending paths data and descending paths data separately and combined in a successive step. The two paths are not perpendicular and form anangle of 30° in the Agulhas current area. This results in strong uncertainties on the reconstructed velocities (mainly the meridional component, due to the polar orbit of the satellite). A method has been proposed that combines the altimeter direction information to the SAR velocity amplitude to overcome this issue.

Then, mean velocities have been calculated in both areas and compared to the mean drifter velocities used for the CNES-CLS13 MDT calculation, and to the CNES-CLS13 mean velocities. In both areas, for different reasons, a strong impact can be expected from the use of these novel data for higher resolution MDT calculation. In the Agulhas current area, SAR velocities are very consistent with drifter velocities in the main core of the current, and both are much stronger than altimeter velocities. In the MAB area, drifter velocities appear to be quite noisy. It may be due to the difficulty to properly extract the ageostrophic component from the drifter velocities, and the difficulty to remove the temporal variability. HF radar velocities resolve much higher and coherent signal that should be exploited to improve the MDT in this area (maybe discarding the drifter velocities...).

In both areas, we expect these new measurements to provide significant information at resolution of around 1/10°-1/8°.

Aucune partie de ce document ne peut être reproduite sous quelque forme que ce soit,
ni communiquée, ni utilisée, sans l'accord préalable de CLS.

1. Introduction

The objective of this work is to investigate the potential contribution of novel measurements of ocean surface currents to improve regionally the ocean Mean Dynamic Topography. It was proposed as optional tasks of the study regarding the calculation of the new global CNES-CLS13 Mean Dynamic Topography (DR2). Two observation systems have been identified that could bring significant additional information, the HF-radar observing systems in the Mid-Atlantic Bight area (Figure 1a), and the spaceborne SAR system in the Agulhas Current area (Figure 1b).

These areas have in common to be coastal areas, and therefore challenging both for the altimeter measurement system, and for the physical processes dominating the surface circulation. While in the open ocean geostrophy and Ekman currents are dominant in a first approximation, other phenomena (tides, wave-induced stokes drift...) may dominate in coastal areas. The two regions are complementary because they feature two different dynamics. In the Mid-Atlantic Bight area, North of the Gulfstream, the mean circulation is relatively weak, while the Agulhas Current area is characterized by an intense Western Boundary Current (the Agulhas Current) flowing along the African coasts.

In section 2 we analyse the global CNES-CLS13 MDT solution in our two study areas. Then in section 3 we carefully analyse the issues that may arise to calculate mean synthetic geostrophic velocities from these new observing systems. In particular we try to quantify the potential signature of ageostrophic signal in multi-year means over these areas, and some discussion is provided on how to best remove them.

Sections 4 and 5 are then dedicated to the analysis of velocity dataset from HF-radar systems in the MAB (section 4) and SAR measurements in the Agulhas Current (section 5), comparison to altimeter data and drifter velocities is done, and their potential use for future regional MDT calculation is discussed.

a-

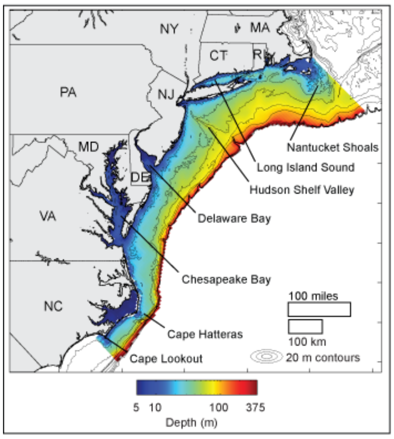

b-

Figure 1 : a-The Mid-Atlantic Bight area; b-The South African coast

2. Analysis of the CNES-CLS13 MDT solution in the two test areas

The CNES-CLS13 MDT and associated mean geostrophic circulation are calculated on a ¼° grid starting from a large scale first guess based on the filtered difference between an altimeter Mean Sea Surface (MSS) and a GOCE geoid. The resulting mean velocities are shown on Figure 2a for the Agulhas Current and on Figure 4 for the MAB area. On Figure 4, the color scale is saturated to better visualize the circulation north of the Gulfream (where velocities are much higher than 15 cm/s). Strong Southeastward velocities are obtained in the Chesapeake Bay (see Figure 1a for location), for which we might wonder if this is real signal or noise due to less accurate altimeter MSS in such locations. Figure 2b and Figure 4b shows the mean geostrophic velocities calculated from surface

Aucune partie de ce document ne peut être reproduite sous quelque forme que ce soit, ni communiquée, ni utilisée, sans l'accord préalable de CLS.

drifters, averaged into ¼° boxes. In the Agulhas Current area, these velocities resolve very nicely the Agulhas coastal current, with velocities exceeding 1.8 m/s, much stronger than the first guess velocities. As a result, the CNES-CLS13 MDT (Figure 2c) also feature a more intense Agulhas current than the GOCE based first guess. However, in the Agulhas bank south of Mossel Bay (see Figure 1b for location), currents are weak (the Agulhas current has detached at the level of Port Elizabeth and is flowing toward the south west), and we have no drifter information in the area (Figure 2b), because all drifters are advected by the strong Agulhas current. As a result, the estimated CNES-CLS13 current error is higher in that area (Figure 2d), and also along the coast, in the Agulhas Current jet, where variability is high and altimeter data less accurate. We can therefore expect that using other velocity data in this area could improve the mean circulation. In particular, we see that the mean velocities in the Agulhas current are lower in the CNES-CLS13 MDT (1.4 m/s) than in the drifter velocities used as input (greater than 1.8 m/s). This is somehow expected because the drifter velocities are then injected into a multivariate objective analysis for the CNES-CLS13 MDT calculation, which result in some smoothing. However, we expect that the mean Agulhas current may be actually stronger than in the CNES-CLS13 MDT, which justify the need for a regional, higher resolution solution. In CNES-CLS13 MDT, the synthetic mean velocities are calculated in ¼° boxes before inversion. However, coherent signal is observed in 1/8° boxes (Figure 3a) and we could expect to be able to calculate an improved, higher resolution (1/8°) MDT in the area. However, the MDT obtained using these 1/8° mean boxes as input is much smoother (Figure 3b). This is due to the associated errors. Errors on the mean synthetic velocities are calculated as the box variance divided by the number of observations. There are much more observations in ¼° boxes than in 1/8° boxes, so that the errors on the 1/8° box means are much larger (see Figure 3d compared to Figure 3c), which result in a smoothing of the output MDT. This means that it is important to have additional, consistent information in the area to lower the error level in order to correctly take into account this high resolution signal. The methodology of error calculation as done for the CNES-CLS13 MDT might also be revised to tackle this issue.

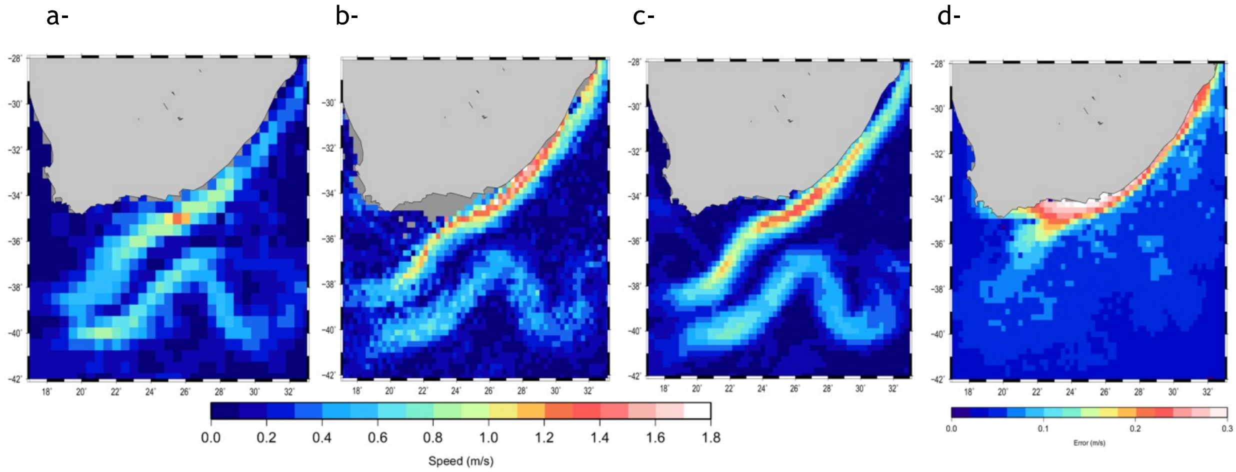

Figure 2 : Calculation of the CNES-CLS13 MDT in the Agulhas Current Area : a- the GOCE based first guess b- the mean drifter velocities c- the CNES-CLS13 mean geostrophic velocities d- the CNES-CLS13 mean geostrophic velocity errors

Aucune partie de ce document ne peut être reproduite sous quelque forme que ce soit, ni communiquée, ni utilisée, sans l'accord préalable de CLS.

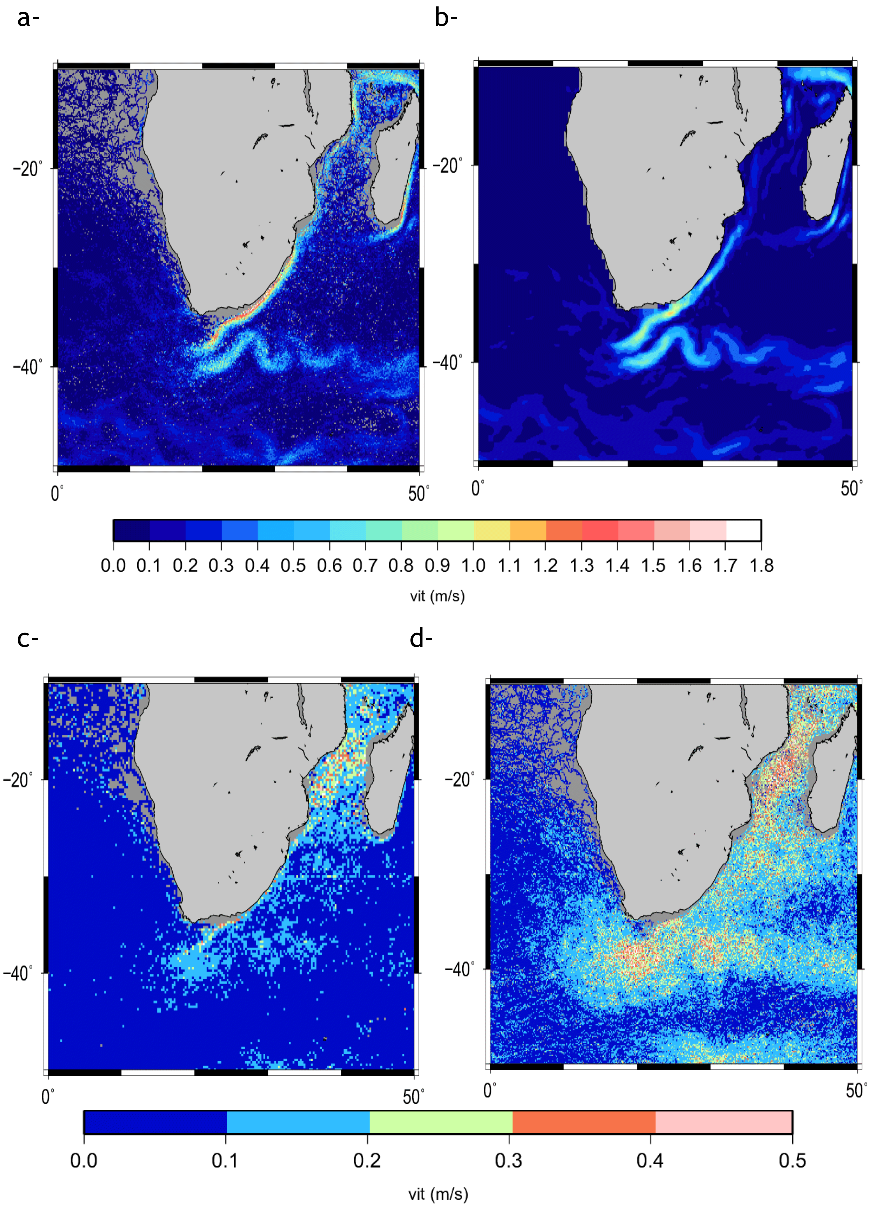

Figure 3 : a- mean synthetic velocities calculated from drifter data in 1/8° boxes ; b- mean velocities obtained after multivariate objective analysis using the 1/8° mean boxes as input ; c errors associated to the ¼° boxes mean synthetic velocities ; d- errors associated to the 1//8° boxes mean velocities.

In the Mid-Atlantic Bight, the situation is different. The mean drifter velocities appear to be somewhat noisier than in the Agulhas current area. Velocity intensities are weaker, and the circulation on the continental shelf might be dominated by ageostrophic signals that may have not been fully or properly removed from the drifter velocities. As a result the CNES-CLS13 MDT velocities also appear to be somewhat noisy (Figure 4c) and strong errors are obtained very close to the coast (Figure 4d). We therefore expect that the use of additional, high resolution velocity observations may bring significant information to improve the CNES-CLS13 MDT in the area.

Aucune partie de ce document ne peut être reproduite sous quelque forme que ce soit,
ni communiquée, ni utilisée, sans l'accord préalable de CLS.

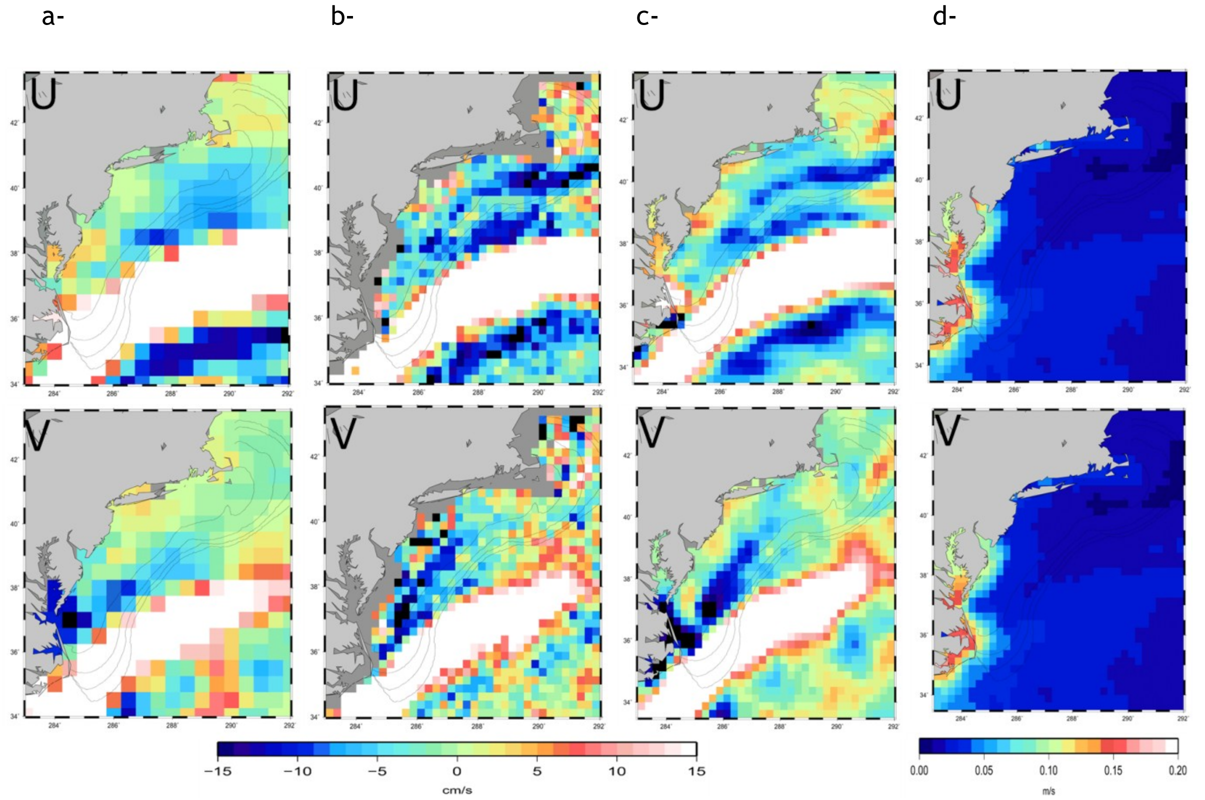

Figure 4 : Calculation of the CNES-CLS13 MDT in the Mid-Atlantic Bight Area : a- the GOCE based first guess b- the mean drifter velocities c- the CNES-CLS13 mean geostrophic velocities d- the CNES-CLS13 mean geostrophic velocity errors

3. Calculation of mean geostrophic velocities

3.1. Method

The method used in Rio et al (2011, 2014) to calculate estimates of the mean geostrophic circulation ($\overline{U}_{1993\text{-}2012}, \overline{V}_{1993\text{-}2012}$) from the combination of surface drifter velocities and altimeter data may be applied to other types of current velocities, as the SAR derived velocities and the HF radar measurements. The method consists in:

- Extracting from the velocity measurement the only geostrophic component (Equation 1)

$$U_{obs}^{geo}(t,x,y) = U_{obs}(t,x,y) - U_{ageo}(t,x,y)$$

$$V_{obs}^{geo}(t,x,y) = V_{obs}(t,x,y) - V_{ageo}(t,x,y)$$

Equation 1

Depending on the geophysical signal measured by an observing system, the ageostrophic components U_{ageo},V_{ageo} may differ. For instance, in the case of drifting buoy velocities, the ageostrophic components contained in the measured velocities include the Ekman currents, the Stokes drift, the tidal currents, the inertial oscillations...This is the same from the velocities measured by HF radars. In the case of SAR derived velocities however, we will see in section 3.1 that the processing of the SAR Doppler anomaly applied to extract the surface current implies the removal of all wind-wave driven effects, including in particular the Stokes drift and the Ekman

Aucune partie de ce document ne peut être reproduite sous quelque forme que ce soit, ni communiquée, ni utilisée, sans l'accord préalable de CLS.

currents. In that case, only the contributions of inertial and tidal currents need to be removed to extract the geostrophic current.

In section 3.1 we try to quantify the intensity of these different ageostrophic contributions in multi-year mean currents and discuss the different methods that may be applied to remove these currents from the velocity measurements (section 3.2).

- Removing the temporal variability of the geostrophic velocity as measured by altimetry. (Equation 2). Altimeter anomalies are referenced to a given time period (1993-2012) in the case of the last SSALTO-DUACS reprocessing. The obtained mean velocities are consequently representative of the same reference period.

$$\overline{U}_{1993\text{-}2012}(t,x,y) = U_{obs}^{geo}(t,x,y) - U'_{alti/(1993\text{-}2012)}(t,x,y)$$

$$\overline{V}_{1993\text{-}2012}(t,x,y) = V_{obs}^{geo}(t,x,y) - V'_{alti/(1993\text{-}2012)}(t,x,y)$$

Equation 2

The main issue of this processing step is the different spatial and temporal resolution of the measured velocities and the altimeter velocity anomalies. Indeed, the spatial and temporal scales resolved should be exactly the same in order to correctly remove the variable velocity component from the measured instantaneous velocity. The effective temporal and spatial resolution of the obtained altimeter current maps at one time depends on the altimeter satellite constellation. For example, considering a 10 days temporal resolution, spatial scales of the order of 150km (resp. 100 km) are resolved with 2 (resp. 3) satellites (Pujol et al, 2012). Further improvements are expected with the launch in 2020 of the SWOT (Surface Water and Ocean Topography) mission, whose wide-swath altimeter will enable to resolve 1km spatial scale structures in a 120 km wide swath along the satellite path (Fu and Rodriguez, 2004). However, the mesoscale mapping capability of SWOT will differ from regions with high temporal sampling (in these areas SWOT will be equivalent to a 4 classical altimeters constellation) to regions with low temporal sampling (equivalent to a 2 classical altimeters constellation). HF radar velocity measurements have a much higher spatial (6 km) and temporal (1 hour) resolution than the altimeter system. For the SAR measurements, the spatial resolution is much higher (4-8 km) and the temporal resolution (2-3 days) is also somewhat higher. The difficulty then is that not all the spatio-temporal variability of a measured velocity is removed through Equation 2, and some residual signal pollutes the mean estimate. In addition, in coastal areas, altimeter measurements are less accurate, so that the use of altimeter data in Equation 2 may result in additional noise instead of removing geophysical signal. A simple approach allowing to check for this issue, and to quantify the amount of signal variability removed by the method, is to calculate the variance of the measured velocities in small boxes and compare it to the variance of the synthetic mean velocities. If the methodology is efficient to remove the temporal variability, the variance should be reduced. In section 3.3 we check the validity of this approach in our two areas.

- The mean velocities are then used through a multivariate objective analysis to improve a Mean Dynamic Topography first guess. This is feasible because mean geostrophic velocities and mean dynamic heights are linearly related (through the derivative operator of the geostrophic approximation). The method requires an accurate prescription of the mean velocities error.

3.2. Characterization of the multi-year mean of the main ageostrophic currents

As discussed above, a number of ageostrophic currents are measured by the various velocity observing systems in addition to geostrophy. They have to be removed, and in the specific case of coastal regions, their contribution to the total current is quite significant. By chance, as we are speaking about Mean Dynamic Topography, what is of interest to us is the mean contribution of these effects on the mean current, which may be of course a lot reduced compared to the instantaneous value. In the case of tidal currents for instance, if an observing system measures the surface currents at the same point with a temporal resolution better than one hour, the tidal currents will average to zero when calculating the mean currents. To a certain extent, this is the

Aucune partie de ce document ne peut être reproduite sous quelque forme que ce soit,
ni communiquée, ni utilisée, sans l'accord préalable de CLS.

case for HF radar measurements (when there is no gap in the time series at a given point). Other, non periodic currents, won't average to zero, but, due to the high variability of these currents, their mean amplitude will of course be much lower than their instantaneous value. In this section, we aim at giving an idea of the mean amplitude of those currents. This information may be used to give a maximum error level when using measurements of the ocean surface velocity to calculate the Mean Dynamic Topography without first correcting them for the unwanted ageostrophic signal.

The surface currents are coupled to the atmosphere by wind stress and momentum transfer, and to the deep ocean by eddy viscosity and momentum transfer. The main physical processes that determine the speed and direction of currents at and near the surface are **Stokes drift**, resulting from nonlinearities in the surface gravity waves, and **Ekman dynamics**, resulting from viscosity and Coriolis forces related to the rotation of the earth. The former is explained by Ekman theory (Ekman, 1905) and indicates a quadratic relation between the surface wind drift currents and the wind; the latter is caused by the nonlinear character of waves generated by wind and indicates a linear relation between the Stokes drift and the wind. The momentum transfer from the wind into the ocean is through both wind shear stress and wave generation. Therefore, these two components are independent of each other but work together to generate the current response.

3.2.1. Ekman currents

Ekman's theory predicts that the angle between the wind-driven surface current vector and the wind vector is 45°. This is derived under the assumption of a constant vertical eddy viscosity for steady wind-driven currents in an infinitely homogenous ocean. The shortcomings of a constant vertical eddy viscosity have long been recognized, and as a result the simple Ekman model has been extended to include variable eddy viscosity as well as boundary layers.

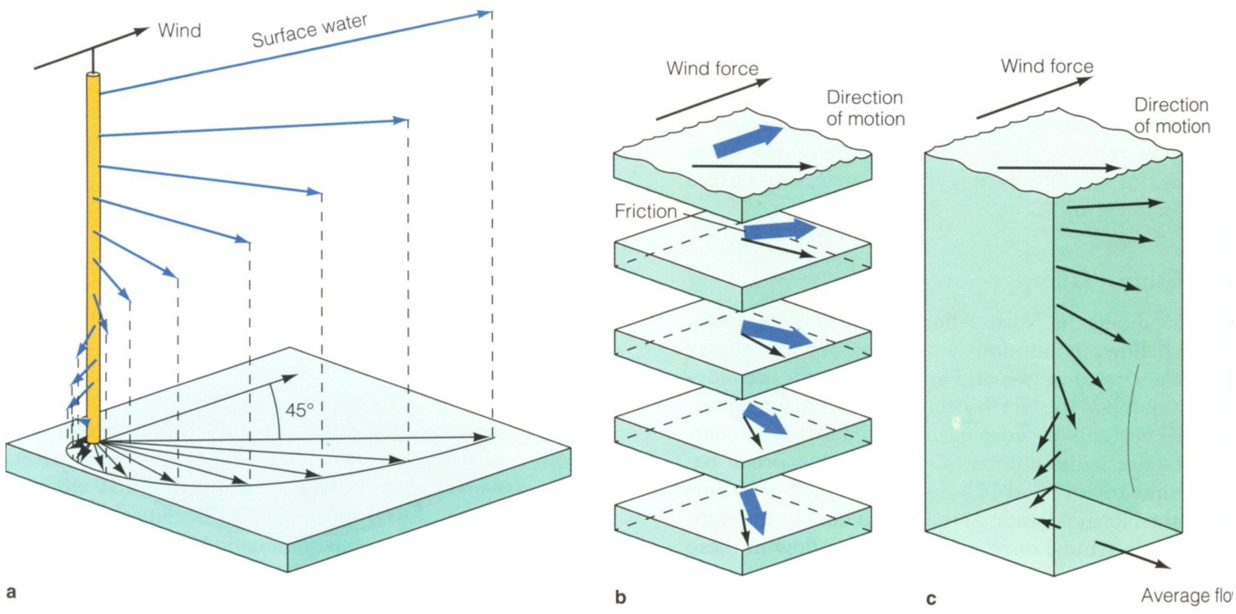

Figure 5: Current profile in the upper layer induced by the Ekman spiral.

In Rio et al (2011, 2014), the Ekman currents are removed from the drifting buoy velocities using a model by Rio et al (2012, 2014). Figure 6 shows the mean Ekman currents calculated at the surface using the model by Rio et al (2014) for the Agulhas current area and for the Mid-Atlantic Bight area over the 2009-2011 time period. In the Agulhas Current area, the mean Ekman currents are of the order of 2-3 cm/s, they are stronger (6-8 cm/s) in the Mid-Atlantic Bight area. In both areas, Ekman

Aucune partie de ce document ne peut être reproduite sous quelque forme que ce soit, ni communiquée, ni utilisée, sans l'accord préalable de CLS.

currents feature large spatial scales (this is partly due to the low spatial resolution (75 km) of the ERA INTERIM wind products used to calculate those currents).

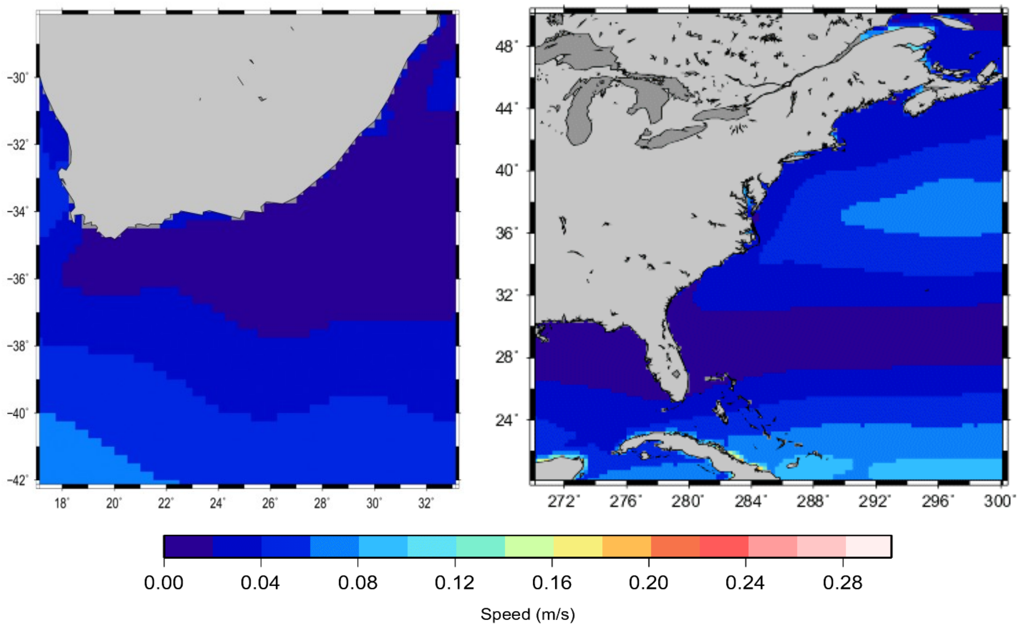

Figure 6 : Mean Ekman currents in the Aghulas Current area for the period 2009-2011 (left) and in the Mid-Atlantic Bight area for the period 2009-2013 (right)

3.2.2. Stokes drift

However, Stokes drift generated by waves also has an effect on the angle relation between the total surface drift currents and the wind. As waves travel, the water particles that make up the waves do not travel in a straight line, but rather in orbital motions). While investigating oscillatory waves, G.G. Stokes (1847) discovered that water particles do not move over a closed orbital path. Instead, Stokes found that water particles have an additional movement in the direction of wave propagation. As the particles progress in an orbital motion, their movement is enhanced at the top of the orbit and slowed slightly at the bottom (Figure 7)

The result is a net forward motion of water particles, referred to as Stokes drift.

$$\overline{u}_S \approx \omega\, k\, a^2\, \mathrm{e}^{2kz} = \frac{4\pi^2\, a^2}{\lambda\, T}\, \mathrm{e}^{4\pi\, z/\lambda}.$$

with

a is the wave amplitude, *k* is the wave number: $k = 2\pi / \lambda$,

ω is the angular frequency: $\omega = 2\pi / T$,

z is the vertical coordinate, with positive *z* pointing out of the fluid layer,

λ is the wave length and *T* is the wave period

Aucune partie de ce document ne peut être reproduite sous quelque forme que ce soit,
ni communiquée, ni utilisée, sans l'accord préalable de CLS.

Depending on sea state, the stoke drift depends on wave development regime and duration. Mao and Heron (2008) showed that in case of short-fetch regime both Stokes drift and wind stress contribute to surface current whereas Stokes drift dominates in long-fetch situation.

In short-fetch regime, the wave growth rate is high, the angle between the surface current and wind is bigger (24.4°) and the Stokes drift is about 1.5% of the wind speed

In long-fetch (open ocean), transition waves are encountered and the angle between the surface current and wind is smaller (14.4°). The Stokes drift is about 2.1% of the wind speed in this case.

In Chapron et al (2005), a typical value for the Stokes drift is given that ranges from 1.25% to 1.6% of the wind speed.

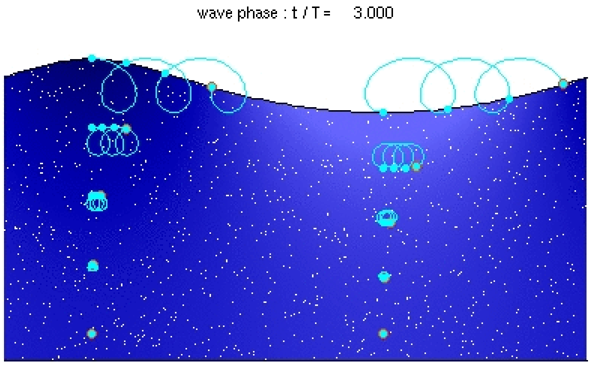

Figure 7 : Stokes drift in deep water wave

Figure 8 shows the mean amplitude obtained from this model over one month (September) in 2009 for our two study areas. Figure 9 shows the mean amplitude of this component calculated over the Agulhas Current and the Mid-Atlantic Bight area using both values and ECMWF wind analysis. Surface Stokes drift can also be computed from a global wave model. The WaveWatch3 model for instance from Rascle and Ardhuin (2013) provides hourly estimates of the Stokes drift.

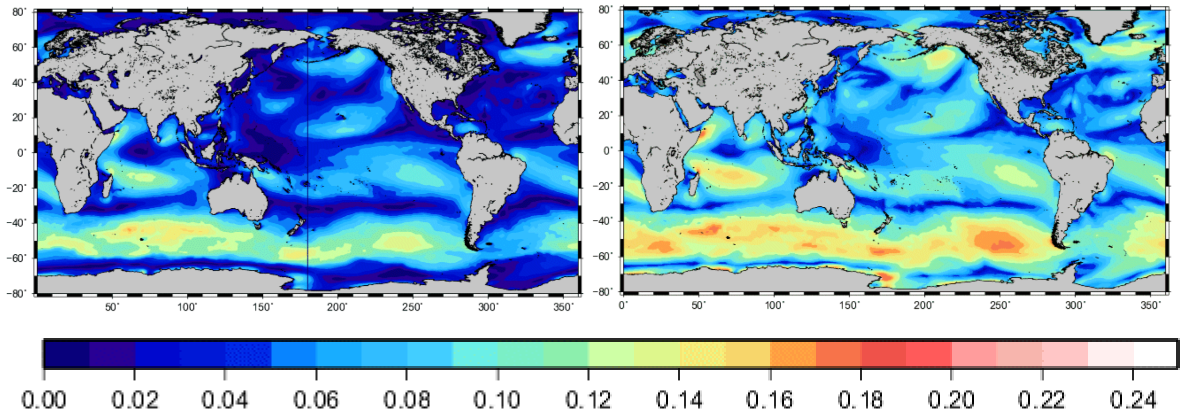

Figure 8 : Mean Stokes drift over one month (September 2009) calculated (left) from the WW3 model, and (right) using the 1.25% wind value.

Aucune partie de ce document ne peut être reproduite sous quelque forme que ce soit,
ni communiquée, ni utilisée, sans l'accord préalable de CLS.

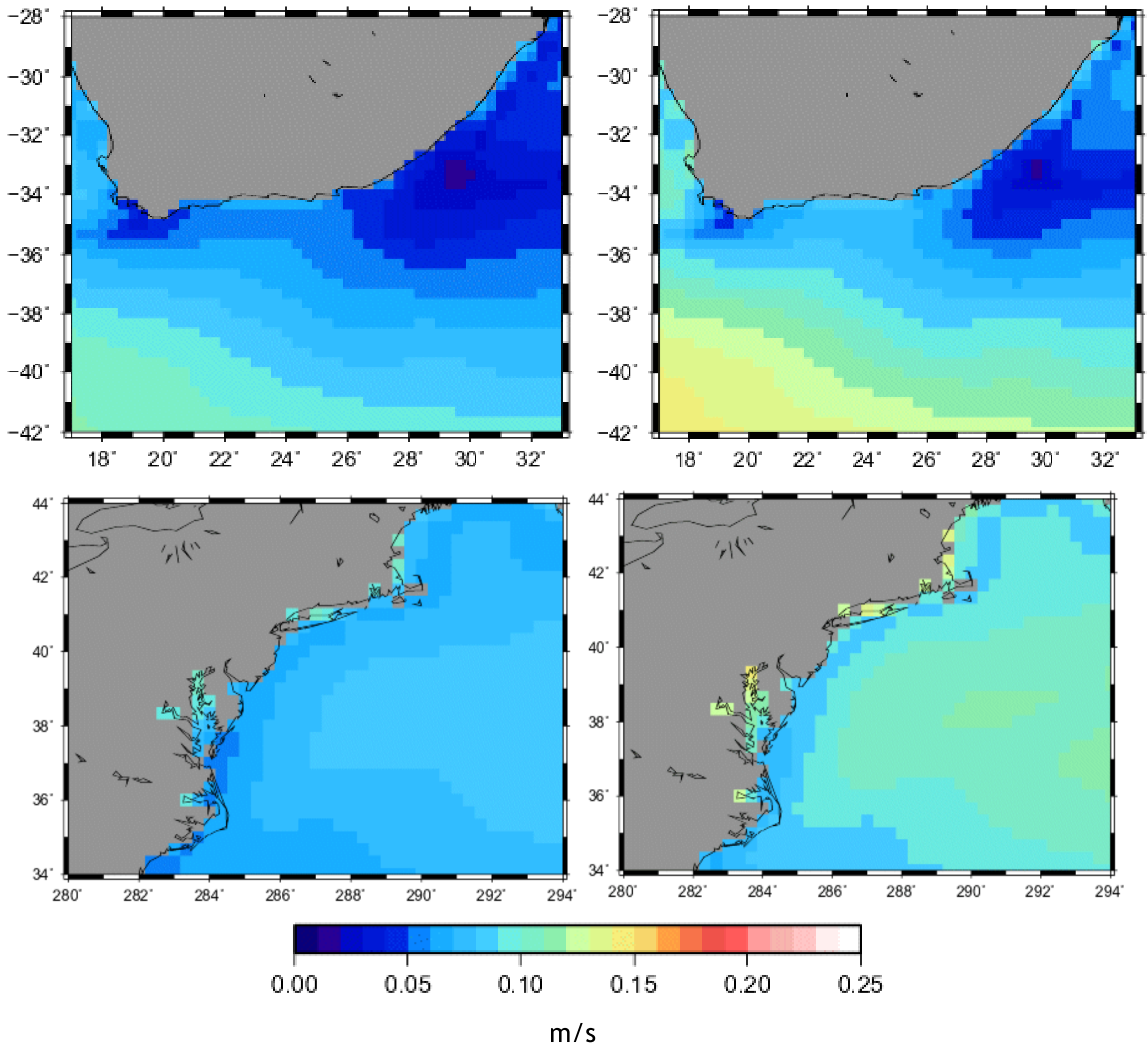

Figure 9 : Mean Stokes drift for the 2009-2013 time period calculated as 1.25% (left) or 1.6% (right) of the Wind value over the Aghulas Current area (top) and the Mid-Atlantic Bight Area (bottom).

3.2.3. Inertial oscillations

When wind and wave forces that have set upper ocean motions cease to strongly act, water will not rest immediately. Energy imparted by the wind and waves takes time to fully dissipate. The Coriolis force will then continue to apply as a **centripetal force**, leading to **rotational flows**, referred as **inertial currents**. The period of rotation will vary with the local Coriolis parameter f (e.g. latitude dependent). The solution (u_i,v_i) to the equation of motion for a frictionless ocean is simply:

$u_i=V\cos ft$

$v_i=V\sin ft$

As friction cannot be completely neglected, inertial oscillations in the real ocean decay in a few days. The amplitude of the inertial motion is proportional to the cumulative wind forcing term and inversely proportional to the water density and thickness of the mixed layer (Park et al, 2005).

Analyzing Argo floats surface velocities, Park et al (2005) found that the distribution of inertial amplitudes is non-Gaussian in the range 0-80 cm/sec with an average value of 13.7 cm/sec. The

Aucune partie de ce document ne peut être reproduite sous quelque forme que ce soit, ni communiquée, ni utilisée, sans l'accord préalable de CLS.

inertial amplitude in the mid-latitude (30-45°N) band exceeds those in both the low (15-30°N) and high (45-60°N) latitude bands. In three basins, the amplitude in summer is greater than that in winter by 15%-25%. Using drifting buoy data, Chaigneau et al (2008) calculated a climatology of near inertial current characteristics. We reproduce on Figure 10 their map of inertial oscillation amplitude. In the Mid Atlantic Bight areas, as well as in the Aghulas Current, the amplitude of the inertial oscillations is about 10 to 15 cm/s. Important to note is that those values refer to the mean amplitude of the inertial oscillations, and not to the amplitude of the mean (which may be less).

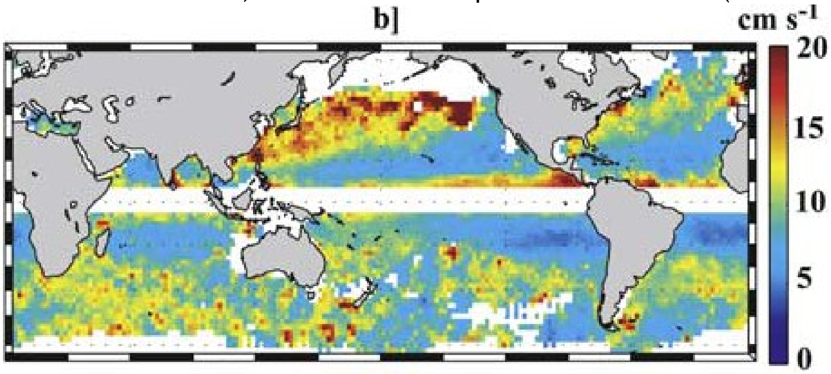

Figure 10 : Inertial current amplitude from surface drifters. From Chaigneau et al (2008).

3.2.4. Tidal currents

Tides are related to gravitational variations associated to the Sun and Moon alignments, resulting in periodical changes in water levels.
As already mentioned, well sampled tidal currents average to zero. However, depending on the temporal resolution of observed velocity measurements, tidal currents may be aliased into the mean. The amplitude of the residual mean current will strictly depend on the temporal sampling of the observing system.

3.2.5. Intensity of ageostrophic signal in the drifting buoy velocities used for the CNES-CLS13 MDT calculation

For calculating the synthetic mean velocities in the CNES-CLS13 MDT (Rio et al, 2014), drifting buoy velocities are processed as follow: first the Ekman current contribution is calculated and subtracted and a further 3 days low pass filter is applied along the buoy trajectory to get rid of the ageostrophic currents listed above: tidal current, stokes drift, inertial oscillations and any residual Ekman current not well resolved by the model used. It is therefore interesting in order to quantify the intensity of the cumulated tidal, stokes and inertial currents (and residual Ekman) to calculate the difference between the filtered and unfiltered drifting buoy velocities. Mean and standard deviation of the differences calculated in 1/8° boxes are shown on Figure 11. Note that in that case, the time period covered in each box may be different, due to the inhomogeneous sampling of the drifting buoys.

Results are shown both for drogued drifters (left plots) and undrogued drifters (right plots). Outside the strong western boundary currents (the Gulfstream, the Aghulas current), the mean velocity difference is of the order of 2-3 cm/s, while it can get quite large in the strong currents (10 to 20 cm/s). The variance of the difference is of the order of 4 cm/s in the Mid-Atlantic Bight, and quite larger in the Aghulas Current area (more than 10 cm/s locally).

Aucune partie de ce document ne peut être reproduite sous quelque forme que ce soit,
ni communiquée, ni utilisée, sans l'accord préalable de CLS.

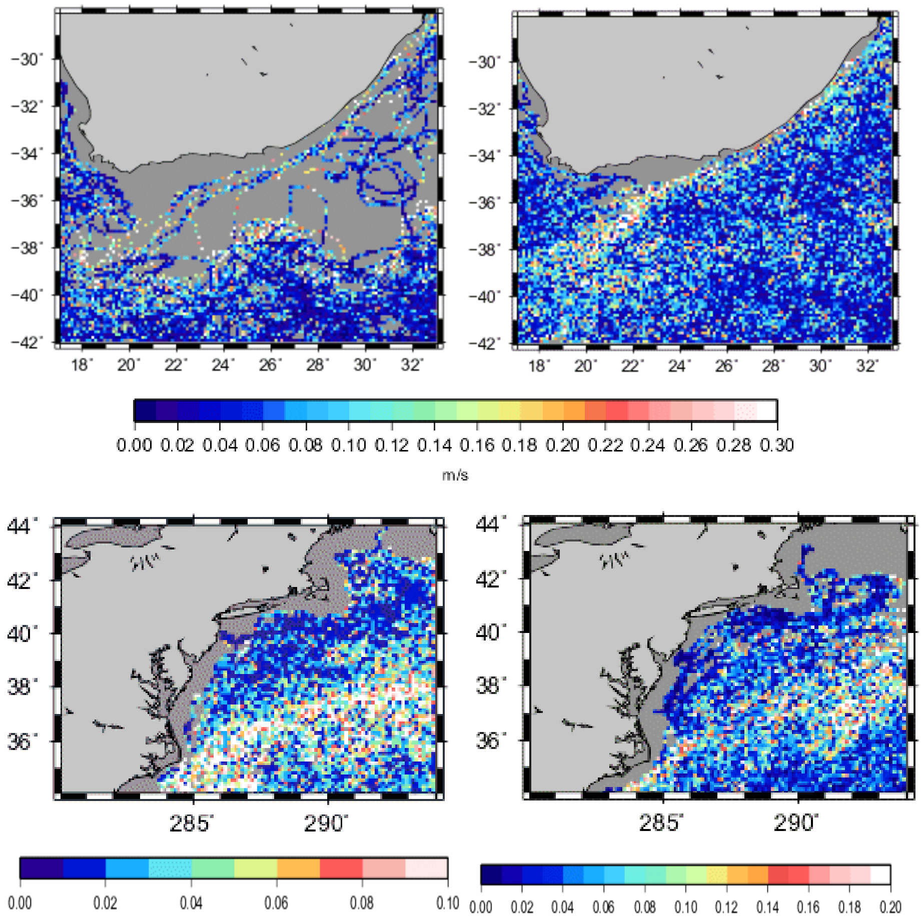

Figure 11 : Mean velocity difference between unfiltered and filtered drifting buoy velocities (Ekman currents have been removed) for drogued (left) and undrogued (right) drifters in the Aghulas Current area (top) and the Mid-Atlantic Bight (bottom)

Aucune partie de ce document ne peut être reproduite sous quelque forme que ce soit, ni communiquée, ni utilisée, sans l'accord préalable de CLS.

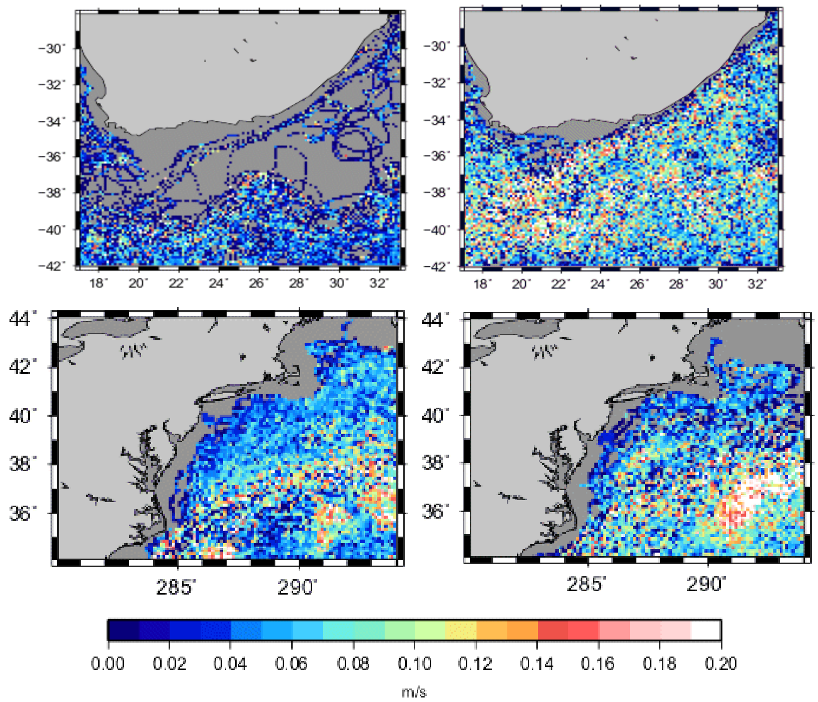

Figure 12 : Variance of the zonal velocity difference between unfiltered and filtered drifting buoy velocities (Ekman currents have been removed) for drogued (left) and undrogued (right) drifters in the Aghulas Current area (top) and the Mid-Atlantic Bight (bottom)

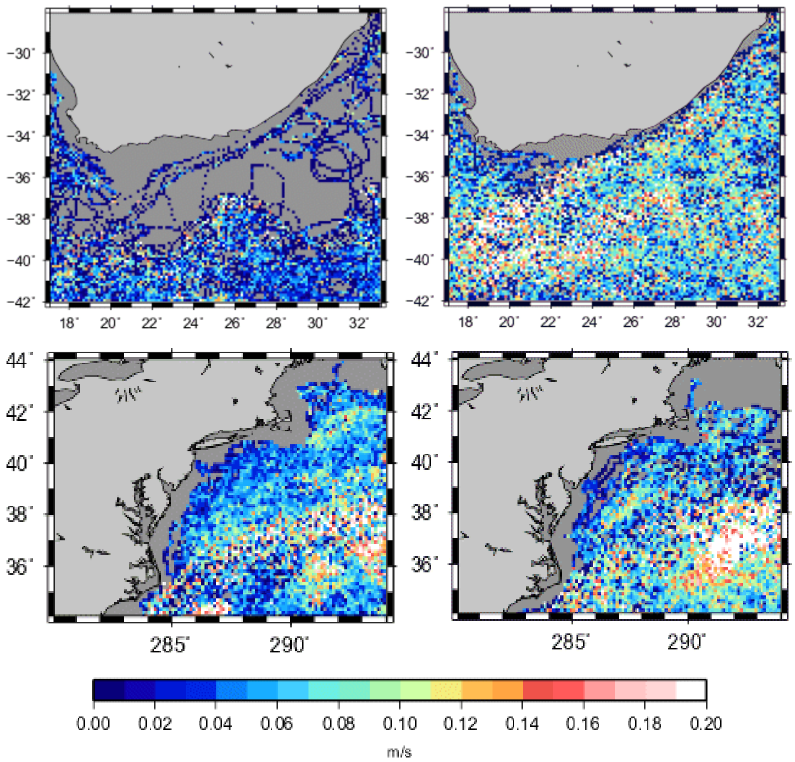

Figure 13 : Variance of the meridional velocity difference between unfiltered and filtered drifting buoy velocities (Ekman currents have been removed) for drogued (left) and undrogued (right) drifters in the Aghulas Current area (top) and the Mid-Atlantic Bight (bottom)

Aucune partie de ce document ne peut être reproduite sous quelque forme que ce soit, ni communiquée, ni utilisée, sans l'accord préalable de CLS.

The large differences obtained in strong currents between the filtered and unfiltered velocities are not due to a stronger ageostrophic signal in those currents (although in those currents, an additional ageostrophic signal, cyclostrophy, should be taken into account), but to the lagrangian nature of the surface drifters: a drifter covers a certain distance in 3 days, much greater obviously in strong currents than in low currents areas. As a consequence, a 3 day temporal low pass filter will also act as a spatial filter. On Figure 14 we show the distance covered by a drifter in 3 days using the mean geostrophic velocities from the CNES-CLS13 MDT solution.

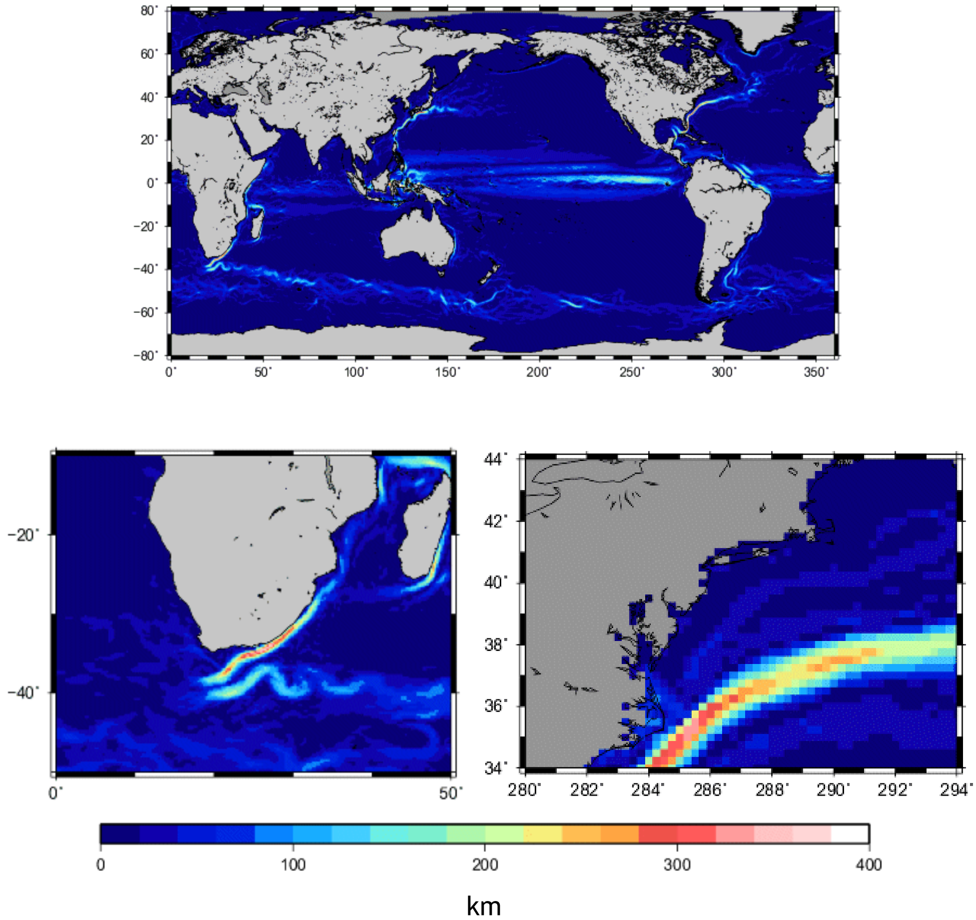

Figure 14 : Mean distance covered by a surface drifter in 3 days (calculated using the mean velocities from the CNES-CLS13 MDT)

3.3. Methods to remove the ageostrophic component from the measured velocities

Two main approaches may be used to remove the unwanted ageostrophic currents from the observed total surface currents: either filtering out the signal, or estimate it (thanks to observations, or models) and subtract it from the total velocity.

To filter out the signal, it is mandatory however to have a velocity time series with adequate temporal resolution. This is the case for HF radar velocities, for which measurements are available hourly. The tidal currents and inertial oscillations can therefore be filtered out using a temporal low pass filter or a simple temporal mean. In the Mid-Atlantic Bight Area, the inertial period varies between 18.5 hours (42°N) and 20 hours (36°N). Averaging the HF radar velocity time series at each

Aucune partie de ce document ne peut être reproduite sous quelque forme que ce soit,
ni communiquée, ni utilisée, sans l'accord préalable de CLS.

point will also remove the high frequency signals. The Stokes drift could be removed at each velocity measurement using the WWIII model outputs.

The strong advantage of the HF radar velocity system over the drifter velocities lies in the availability of long time series of velocities at fixed points. Pure temporal filtering can therefore be applied, while we have seen in the previous section that filtering time drifter velocities also result in spatial filtering. HF radar velocities may therefore help resolve the very short spatial scales of the mean current.

Such temporal filtering cannot be applied on SAR velocities time series as SAR images of the same area are available only every 2-3 days. Stokes drift and Ekman currents are removed in the SAR processing, so the only remaining ageostrophic components are the inertial oscillations and the tides.

Tidal currents may be removed using a tidal model, for instance FES2012 (Stammer et al, 2014). The mean contribution of the inertial oscillations to the surface current will therefore remain in the mean SAR velocity.

3.4. Testing the capability of altimeter measurements to remove the velocity temporal variability from the instantaneous measured velocities

HF radar velocity measurements have a much higher spatial (6 km) and temporal (1 hour) resolution than the altimeter system. For the SAR measurements, the spatial resolution is much higher (4-8 km) and the temporal resolution (2-3 days) is also somewhat higher. The difficulty then is that not all the spatio-temporal variability of a measured velocity is removed through Equation 2, and some residual signal pollutes the mean estimate. In addition, in coastal areas, altimeter measurements are less accurate, so that the use of altimeter data in Equation 2 may result in additional noise instead of removing geophysical signal. A simple approach allowing to check for this issue, and to quantify the amount of signal variability removed by the method, is to calculate the variance of the measured velocities in small boxes and compare it to the variance of the synthetic mean velocities. If the methodology is efficient to remove the temporal variability, the variance should be reduced. In this section we test the ability of altimetry to remove the temporal signal in our two test cases.

We have used all drifting buoy velocities available in the area from 1993 to 2012 and calculated the variance of the buoy velocities in ¼° boxes on one hand, and on the other hand the variance of the buoy velocity from which the temporal variability from the altimetry has been removed. The difference between the two values should be positive, otherwise it means that removing the altimeter measurements has added noise instead of removing geophysical signal. Figure 15 and Figure 16 show the obtained results for the MAB and the Agulhas Current area respectively. In both areas, strong positive values are obtained in the open ocean, but values get closer to / lower than zero when approaching the coast. In the MAB area, slightly negative values (around -5cm/s) are obtained everywhere; this highlights the poor efficiency of using altimeter measurements to remove the temporal variability of the ocean currents in this area. In the Agulhas current, a higher number of negative values is also obtained when getting closer to the coast, but restricted to a narrower band. Note that in the computation of the CNES-CLS13 MDT, altimeter data are not used to remove the variability in such cases, but a mere average of the velocities is performed.

Aucune partie de ce document ne peut être reproduite sous quelque forme que ce soit,
ni communiquée, ni utilisée, sans l'accord préalable de CLS.

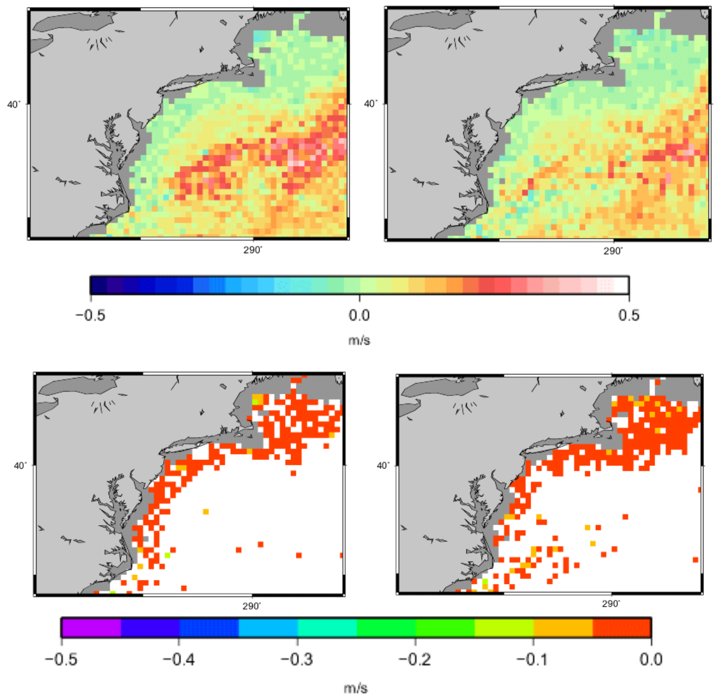

Figure 15 : Difference between the variance of the drifter velocity calculated in ¼° boxes and the variance of the drifter velocities from which the altimeter velocity anomaly has been removed. Left: for the zonal component; Right: for the meridional component. Bottom: Same as top with only negative values colored (white values are all positive)

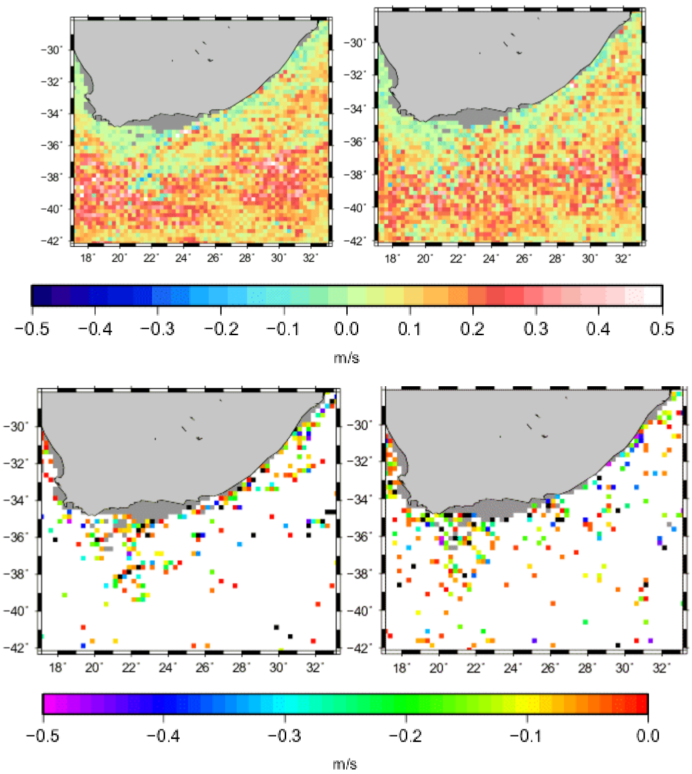

Figure 16 : Same as Figure 9 for the Aghulas Current area.

Aucune partie de ce document ne peut être reproduite sous quelque forme que ce soit, ni communiquée, ni utilisée, sans l'accord préalable de CLS.

4. Feasibility study of using HF radar velocity measurements for the calculation of regional mean dynamic topographies

4.1. Principle of the HF radar measurement

High Frequency (HF) radar ocean current systems (systems that operate in the HF band from 3 to 30 MHz) provide the ability to probe the near-surface ocean currents in the coastal region. The measurements provide synoptic current maps over a few to several thousand square kilometers of the ocean surface.An efficient worldwide HF radar network exists : mainly along US coasts (**Figure 17**) but also in Spain (**Figure 18**), Australia (**Figure 19**) and in some other locations (**Figure 20**).

Figure 17 : Maps of the american HF radar network

Figure 18 : Maps of the spanish HF radar network

Aucune partie de ce document ne peut être reproduite sous quelque forme que ce soit, ni communiquée, ni utilisée, sans l'accord préalable de CLS.

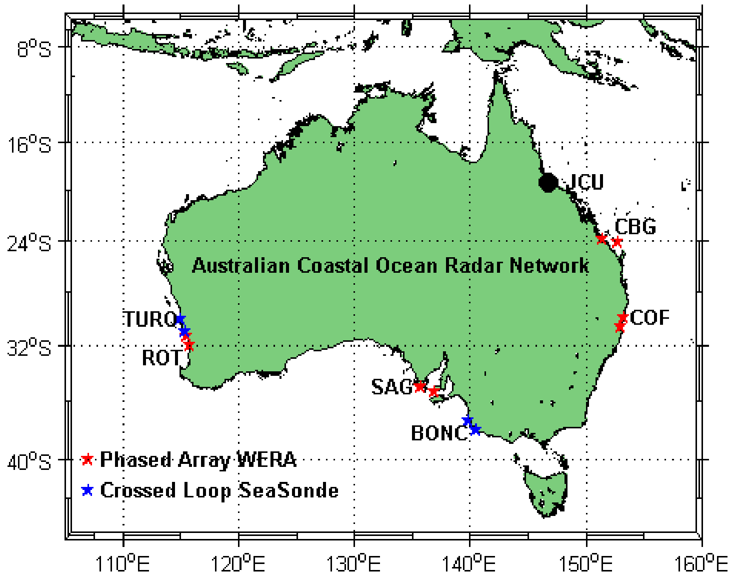

Figure 19 : Maps of the australian HF radar network

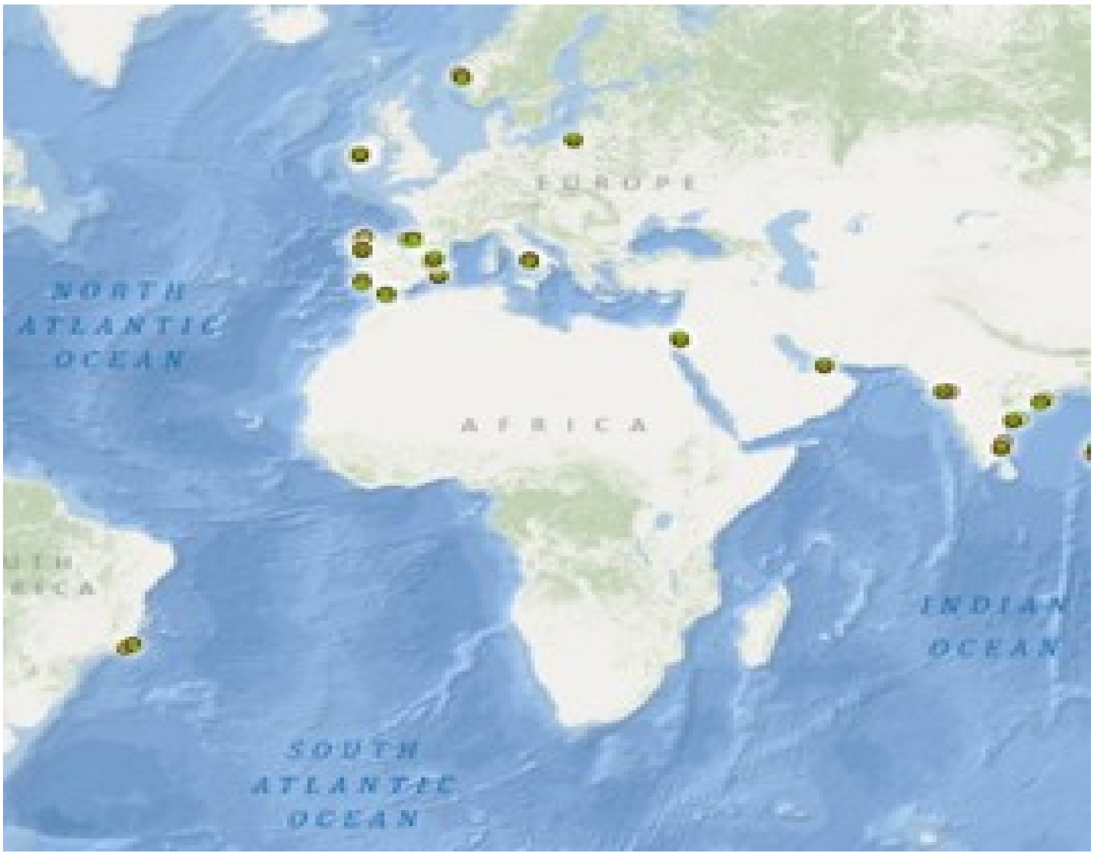

Figure 20 : the worldwide HF radars network (without US)

Aucune partie de ce document ne peut être reproduite sous quelque forme que ce soit, ni communiquée, ni utilisée, sans l'accord préalable de CLS.

HF radar systems use reflections of electromagnetic waves to probe the properties of the ocean surface. Although referred to by the term radar, they operate at much longer wavelengths than is typical for radar systems. The HF band wavelengths used by ocean radar systems typically range from 10 to 100 m. Through analysis of the Doppler spectrum, information can be extracted relating to:

- Near-surface currents [~2m deep]
- Wind speed and direction
- Ocean wave directional spectrum
- Ship activity

HF radar systems, typically deployed along the coast, use then Bragg peaks within a transmitted signal (3~42MHz) scattered off the ocean surface to calculate radial components of the total surface velocity at a given location (Barrick et al. 1977). The earliest recognition of resonant Bragg Scatter from the sea surface is attributed to Crombie (Crombie, 1955), while Barrick, Evans and Weber (Barrick et al., 1977) were among the first to exploit the phenomenon to sense oceanographic properties.

The radar is most sensitive to waves with wavelengths half that of the radar that propagate to or away from the radar (**Figure 21**). These waves are called Bragg waves.

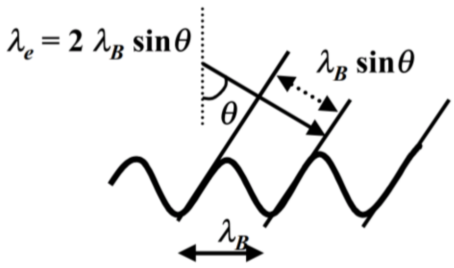

Figure 21 : Illustration of Bragg scattering. The radar electromagnetic wavelength is Le the wavelength of the surface wave is lB and the incident angle of the radar in theta. For the energy backscattered from the ocean wave peaks to be in phase (i.e., the wave is resonant with the radar radiation) the distance that the radiation travels between peaks (lB sin theta) must be equal to half the wavelength of the radiation.

Peaks in the backscattered signal are the result of an amplification of a transmitted wave(Figure 22), at grazing incidence, by surface gravity waves with a wavelength equal to half that of the transmitted signal (Crombie 1955).

Aucune partie de ce document ne peut être reproduite sous quelque forme que ce soit,
ni communiquée, ni utilisée, sans l'accord préalable de CLS.

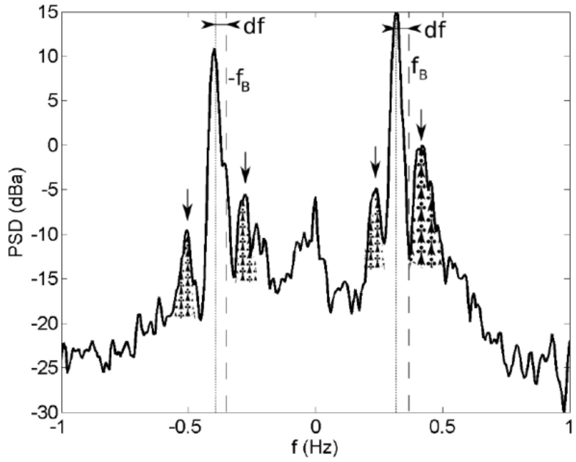

Figure 22 : Two prominent peaks due to waves (approaching and receding). Shift from linear wave frequency is due to surface current component in the direction of the antenna.

The frequency of the backscattered signal will be Doppler-shifted depending on the velocity of the scattering surface. Using the linear wave theory, the phase speed of the surface waves can be separated from the total frequency shift, leaving only that shift due to the surface current component in the direction of the antenna.

Over a given time period, sites along the coast generate radial maps of these component vectors with typical resolutions on the order of 1–6 km in range and 5° in azimuth. Since the Doppler shift can only resolve the component of the current moving toward or away from the site, information from at least two sites must be geometrically combined to generate total surface current maps.

Due to variations in signal-to-noise based on either the electromagnetic interference or sea state conditions, the available radial data can vary in both space and time. To overcome these data gaps, various interpolation techniques have been applied to HF radar total vector fields. These algorithms include 2DVAR (Yaremchuk and Sentchev 2009), normal modes (Lipphardt et al. 2000), open modal analysis (Kaplan and Lekien 2007), and statistical mapping (Barrick et al. 2012; O'Donnell et al. 2005). Recently, Kim et al. (2007) introduced a method that interpolates data as part of the combination step from radial component vectors to total vector maps. This approach weights radials based on the decorrelation scale of the observed current fields.

4.2. Limitations

<u>**For radial velocities**</u>

The conductivity of the seawater also plays an important role in the signal attenuation and the spectral quality of the sea-echo. The signal attenuation decreases with increasing sea water conductivity. This gives a larger range for saltier conditions and a smaller range for fresher water. T

The HF radar data quality also depends on the sea state, where the transmitted radio pulses were backscattered by resonant ocean surface waves. During extreme weather events and rough sea states, the significant wave height increases and the spectral quality of the seaecho decreases.

<u>**For total velocities**</u>

The main source of error in the geometric combination from radials to totals is based on the geometry of the network (Chapman et al. 1997). The contribution of the geometric error is based on the relative angles between the radial component vectors at the total grid point, commonly referred to as the geometric dilution of precision (GDOP). The geometric error increases as the angle between radials from contributing sites moves away from orthogonality.

Aucune partie de ce document ne peut être reproduite sous quelque forme que ce soit,
ni communiquée, ni utilisée, sans l'accord préalable de CLS.

The errors are seen to increase with a decrease in radar operating frequency and to fall between about 2 to 5 cm/s depending on frequency. For the lowest radar frequency, the error is seen to be greater by about a factor of two for the direction finding processed data. Errors with beam forming are more systematic in nature and errors with direction finding, more random in nature.

4.3. Which surface currents are measured by HF radar?

There has been some controversy about the ability of HF surface radar to measure Stokes drift. Many recent research projects were conducted with the assumption that Stokes drift is present in the HF radar surface current data (Graber and Haus 1997; Gremes-Cordero et al. 2003; Ullman et al. 2006). However, in a recent paper (Rohrs et al, submitted to Journal of Physical Oceanography) authors compare HF radar velocities to ADCP velocity measurements on one hand (Eulerian velocity measurement) and surface drifters on the other hand (Lagrangian velocity measurements) and conclude that HF radars do not measure the stokes drift.

In case of logarithmic and linear profile assumptions, the depth of the radar-derived current measurement depends only on the radar wavelength but in the case of a Stokes drift dominated current profile, the effective depth of the measurement depends on the wave energy spectrum as well.

4.4. Data available for the study

Coordinated through the United States Integrated Ocean Observing System, the Mid-Atlantic Regional Association Coastal Ocean Observing System (MARACOOS) deals with a 35-site triple-nested HF radar network that covers the continental shelf between Cape Hatteras, NC and Cape Cod, MA with higher resolution coverage nearshore and into the estuaries (Figure 23). This network is comprised of 13 long-range sites, 2 medium-45 range sites, and 12 standard-range sites (Table 1, extracted from Roarty et al., 2010).

Since the first sites were deployed in 1998, there have been evaluations to determine the optimal system configuration and associated vector uncertainty in the 5-, 13-, and 25-MHz bands (Kohut and Glenn 2003; Kohut et al. 2006; O'Donnell et al. 2005; Roarty et al. 2010). These frequencies cover the scales of the mid and outer shelf, inner shelf, and harbors/estuaries, respectively.

The HF radar sites in the MARACOOS network are all SeaSonde direction-finding systems manufactured by Codar Ocean sensors (Barrick 2008). The direction finding radars use a three element receive antenna mounted on a single post to determine the direction of the incoming signals. The angular resolution, set in the processing, is 5° (Barrick and Lipa 1996; Teague et al. 1997).

Aucune partie de ce document ne peut être reproduite sous quelque forme que ce soit,
ni communiquée, ni utilisée, sans l'accord préalable de CLS.

Figure 23 : Location of the long-range HF radar locations (circles) within the MARCOOS region with four letter site code next to station location

System Type	Radio Frequency (MHz)	Range (km)	Resolution (km)
Long range	4–6	200	6.0
Medium range	12–14	90	3.0
Standard range	24–26	40	1.5

Table 1: extracted from Roarty et al 2010

A concerted effort was made to increase the resiliency of the radar stations from the elements, power issues, and other issues that can disable the hardware of the system. The quality control and assurance activities in the Mid-Atlantic Bight have been guided by the needs of the Coast Guard Search and Rescue Office.

Each site described above collects hourly measurements of the radial surface currents and wave conditions within a footprint local to the antenna. For surface currents this footprint can be as large as 200 km from the site with 6-km resolution for the 5-MHz systems to higher resolution 25 MHz systems that stretch 50 km with a spatial resolution of 1 km.

The radial data from the long-range sites are then combined at Rutgers laboratory into total vectors on a low-resolution 6-km regional scale grid that covers coastal waters from Cape Cod to Cape Hatteras. The total vector fields are made available via Open-source Project for a Network Data Access Protocol (OPeNDAP)
The data used are quality controlledthrough a set of procedures done to instrumentation and a system of processing that ensure quality and measure uncertainties. Roarty et al. 2010 describes this QA. In particular, they provide normalized velocity uncertainty of velocity components. A threshold of 60% of the error variance for either the u or v component was chosen to remove any grid points in real-time data on the basis of this uncertainty threshold to maximize data coverage while preserving data quality (Kohut et al., 2009).
The geometric dilution of precision (GDOP) is a quality control measures used in the HF radar total vector processing The GDOP is defined as the spatial error associated with geometric combination of the radial vectors (Chapman, 1997; Graber et al. 1997). It increases with the distance from the HF radar stations and reaches a maximum along the periphery of the HF radar data footprint, and along the baseline (line connecting the HF radar stations)

This study relies on the following dataset, used over 2009-2013:

Aucune partie de ce document ne peut être reproduite sous quelque forme que ce soit, ni communiquée, ni utilisée, sans l'accord préalable de CLS.

http://tds.marine.rutgers.edu:8080/thredds/dodsC/cool/codar/totals/5Mhz_6km_realtime_fmrc/Maracoos_5MHz_6km_Totals-FMRC_best.ncd'

It deals with grids of total current vector on a hourly basis. At each grid point, both zonal and meridionnal velocity components are provided (unit= cm/s) associated with their respective error level (no units as normalized, so between 0 and 1)

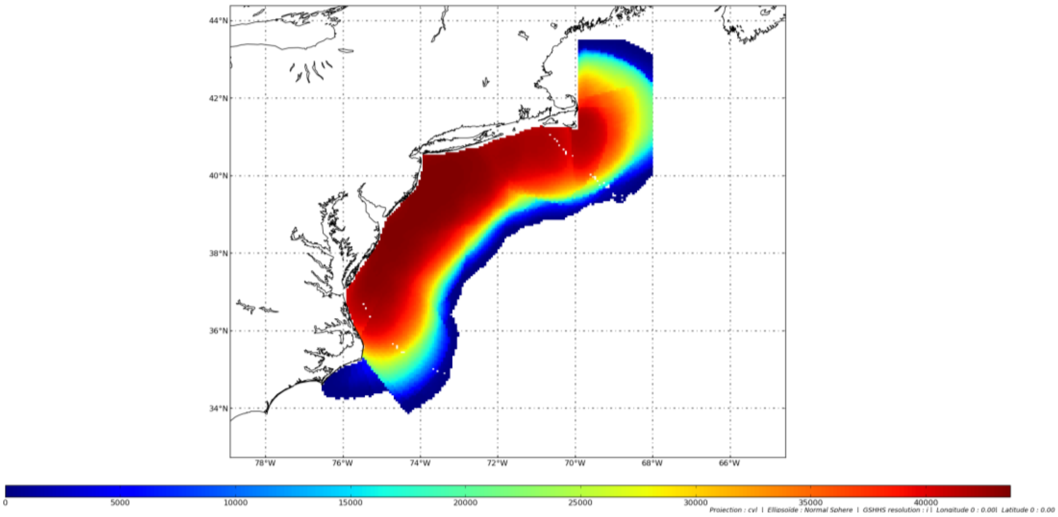

Figure 24 : number of measurements over2009-2013 at each grid point. Min=0.Max=45000.

4.5. Statistical temporal analysis of the HF radar velocities

HF radar observing system provides surface velocities including inertial, tidal and wind & wave – driven dynamics as well as low-frequency geostrophic components. The use of these in-situ measurements in the computation of a regional MDT is done through a time-average of the raw measurements over the time period covered by the array, namely 2009-2013. The number of measurements used for the computation is given by Figure 24.

This section evidences the time average of this array over this period and discusses its interannual variability as well as the need to filter the raw data in a pre-processing stage.

4.5.1. 2009-2013 temporal mean

The Mid-Atlantic Bight 5-years average surface currents are plotted in Figure 25. The mean flow is generally along-shelf to the south-west with mid-shelf surface current speeds in the 5- to 10-cms/s range. Faster currents between 10- and 15-cm/s are found along the shelf-break running alongshore over the central region. East of Cape Cod (70°W,42°N) a area of 6- to 10- cm/s currents is also detected running offshore. The strongest currents observed on the southern edge of the array deals with the Gulf Stream.

The time-variability of these surface currents is given by Figure 26. If the Gulf Stream dominates clearly the signal variance, the area east of Cape Cod presents also a strong time-variability compared to the shelf currents. Strong cross-shelf flows can occurred in this region, particularly during summer (Roarty et al. 2010)

The low-variability areas located in the outer shelf and in the array periphery are not real low-variability dynamics but areas where HF radar errors are strong and dominate the measurements. Figure 27 provides quadratic averaged errors for U and V over 2009-2013.

Aucune partie de ce document ne peut être reproduite sous quelque forme que ce soit,
ni communiquée, ni utilisée, sans l'accord préalable de CLS.

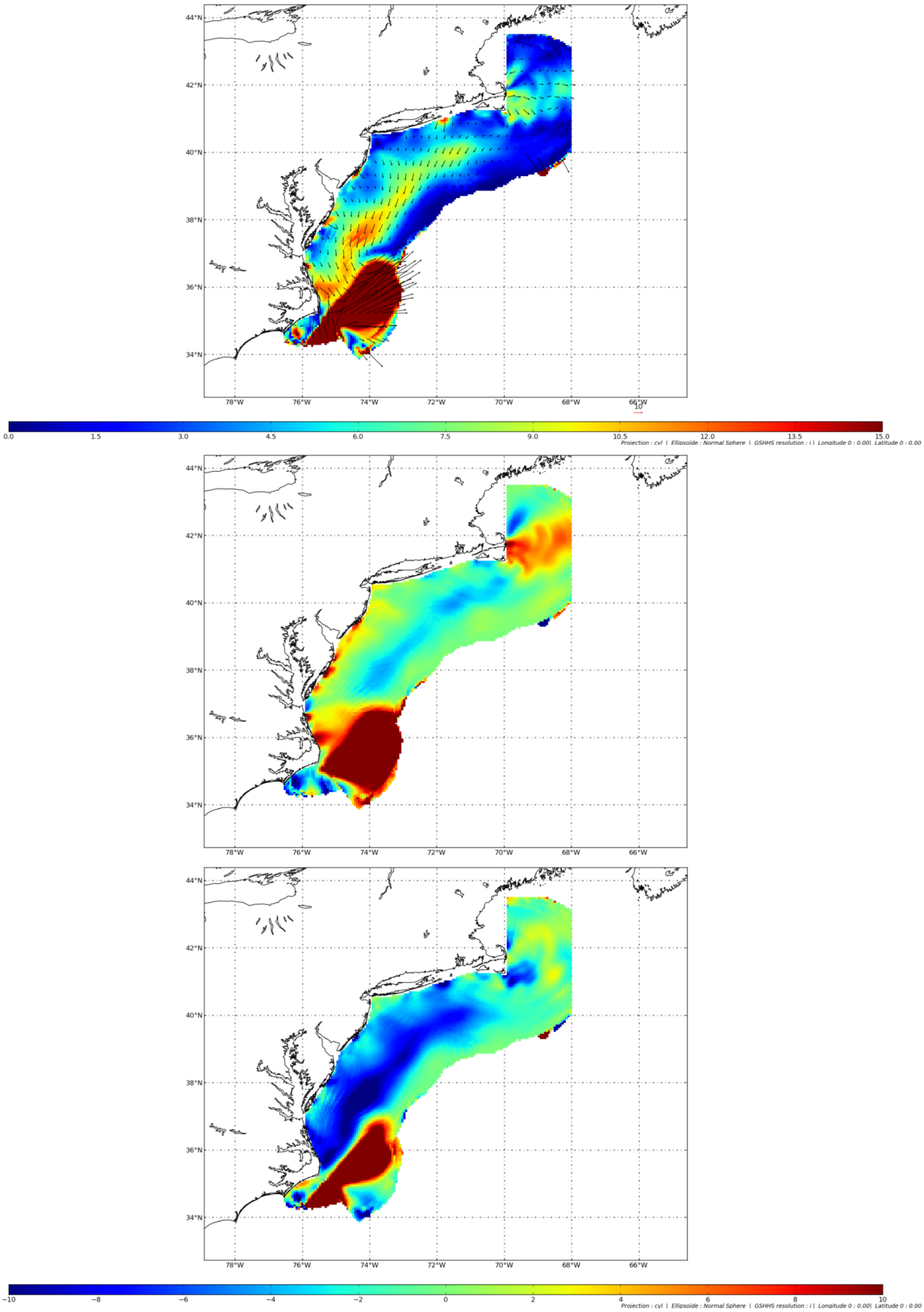

Figure 25 : HF radar surface velocities time-averaged over 2009-2013. Total Vectors in cm/s. min=0. Max=15. (top), U (middle) and V(bottom) in cm/s. min=-10.max=-10

Aucune partie de ce document ne peut être reproduite sous quelque forme que ce soit, ni communiquée, ni utilisée, sans l'accord préalable de CLS.

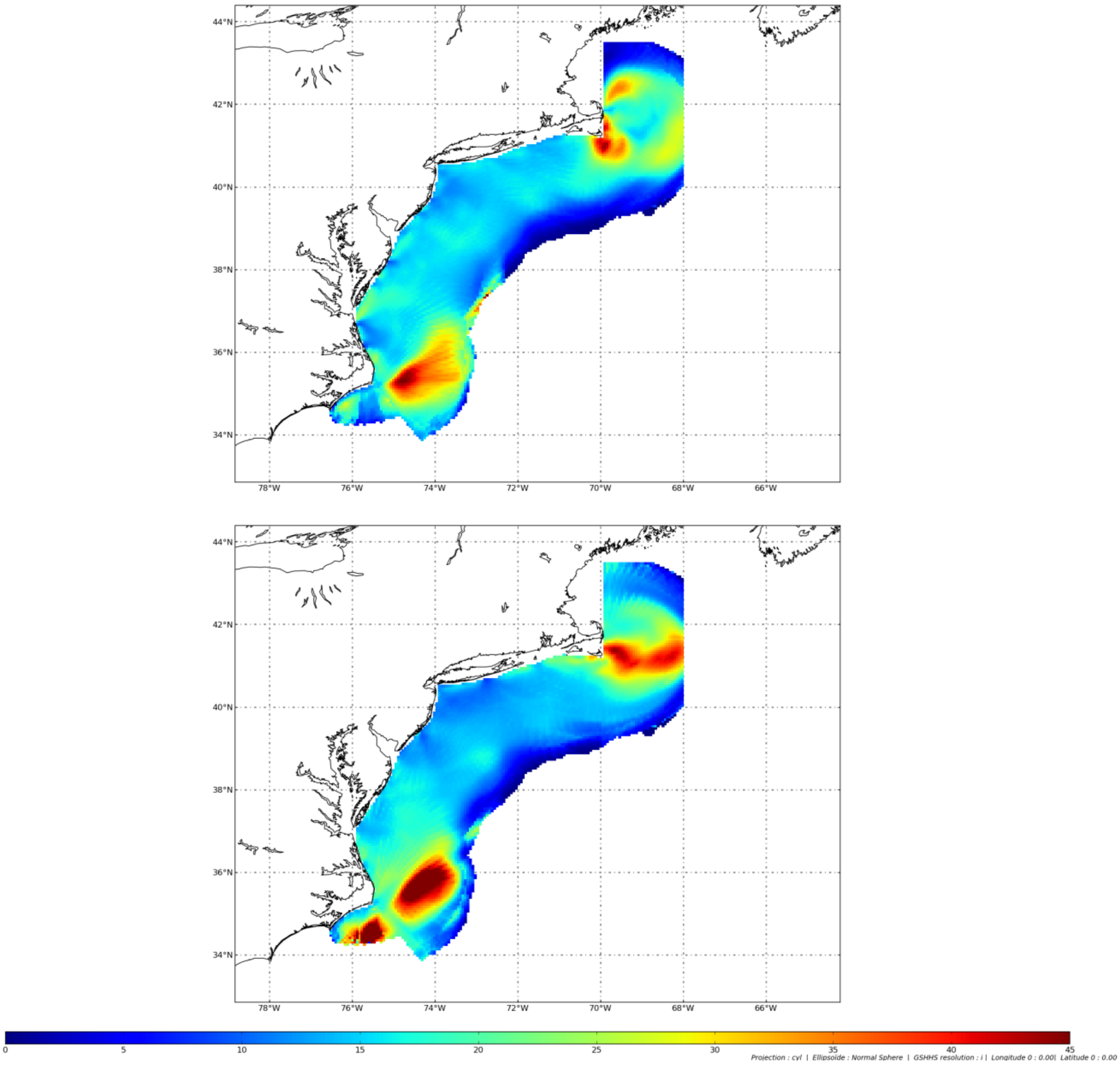

Figure 26 : HF radar surface velocities Standard Deviation over 2009-2013 in cm/s RMS. Min=0. Max=45cm/s RMS.

U (top) and V(bottom)

Aucune partie de ce document ne peut être reproduite sous quelque forme que ce soit, ni communiquée, ni utilisée, sans l'accord préalable de CLS.

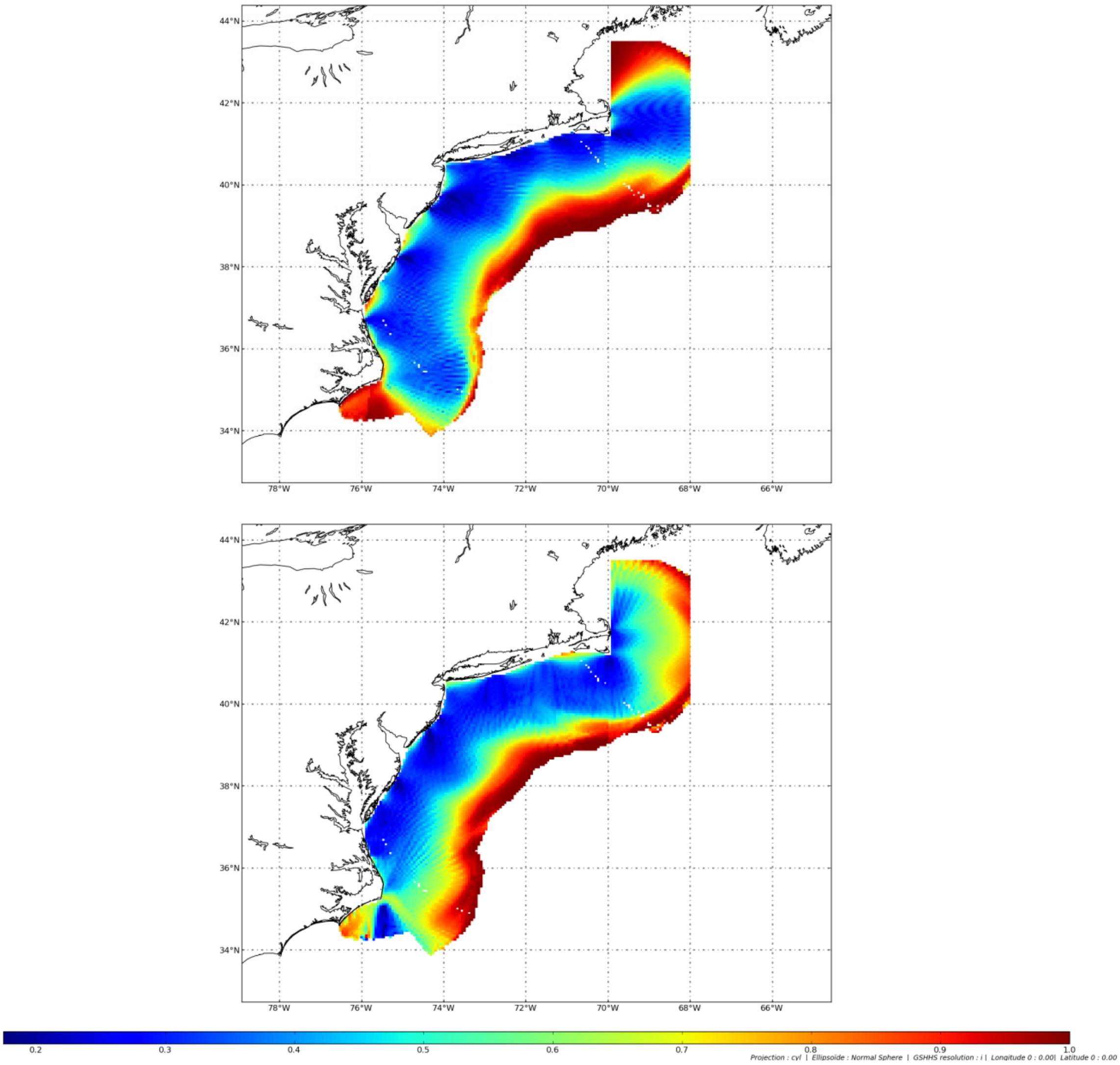

Figure 27 : HF radar surface velocities Normalized Error averaged over 2009-2013 . Min=0. Max=1. U (top) and V(bottom)

Aucune partie de ce document ne peut être reproduite sous quelque forme que ce soit,
ni communiquée, ni utilisée, sans l'accord préalable de CLS.

4.5.2. Interannual variability

Each annual mean within the 2009-2013 period is highlighted to evaluate the interannual variability of the surface mean dynamics of the Mid-Atlantic Bight. **Figure 28** and **Figure 29** show year after year the change in the annual mean U and mean V is sensitive.

It means that taking a 5-years average instead of a 1-year or 20-years will change drastically the mean state of the surface current in this region.

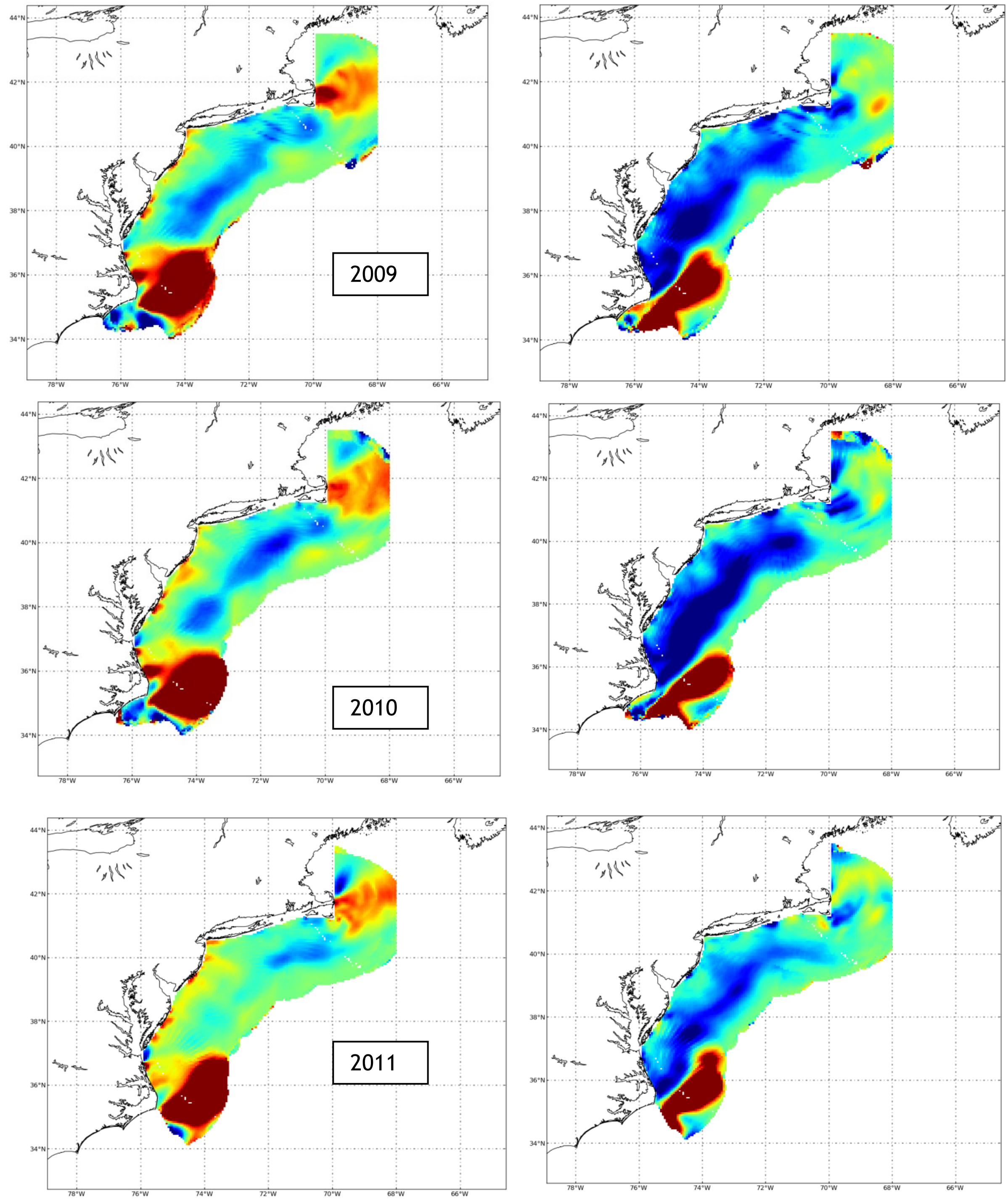

Figure 28 : HF radar surface velocities time-averaged over 1 y from 2009 to 2011. U (left) and V(right). colorbar from Figure 25

Aucune partie de ce document ne peut être reproduite sous quelque forme que ce soit, ni communiquée, ni utilisée, sans l'accord préalable de CLS.

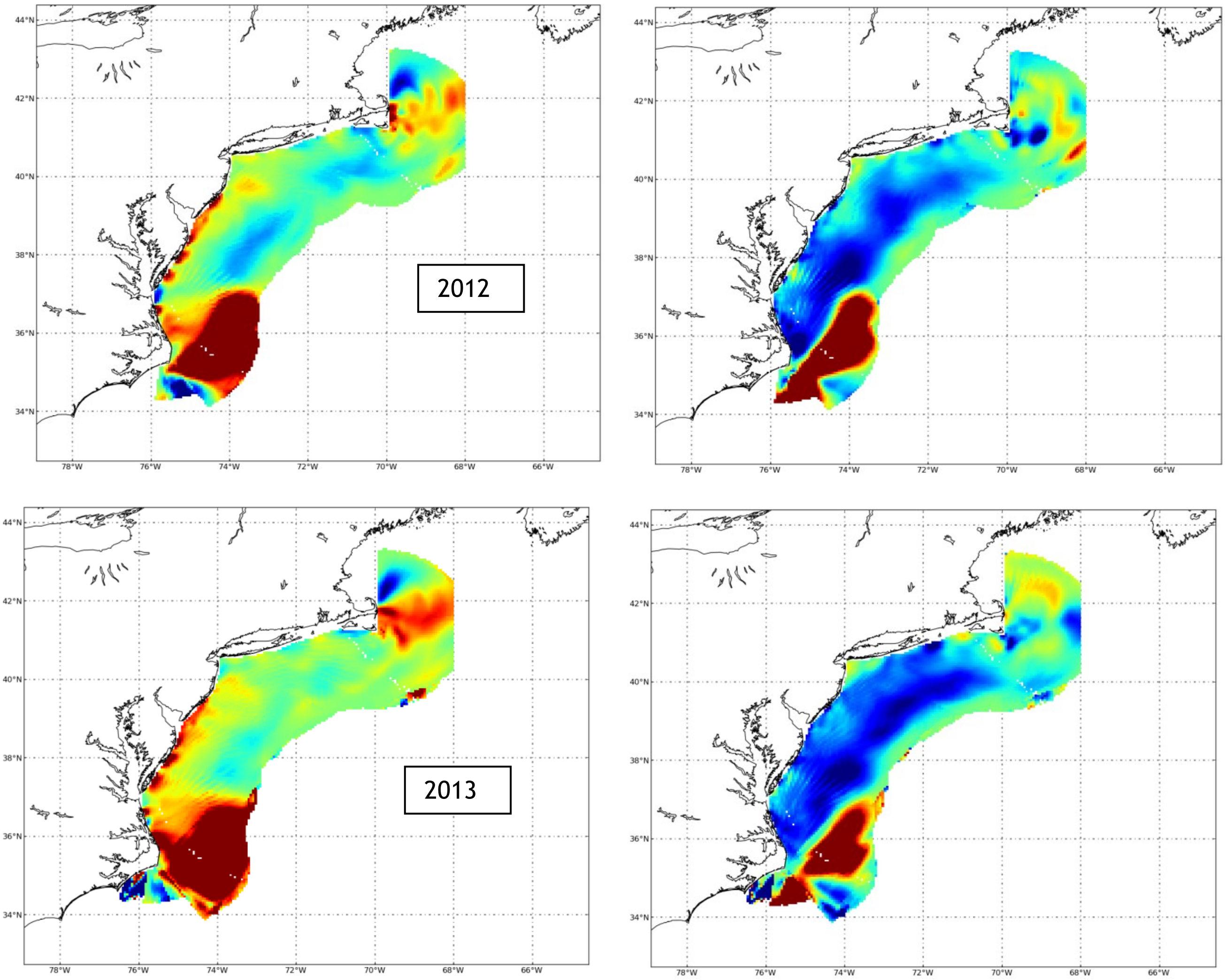

Figure 29 : HF radar surface velocities time-averaged over 1 y from 2012 to 2013. U (left) and V(right).Colorbar from Figure 25

4.5.3. Impact of temporal filtering

In order to remove HF signal in the raw measurements before computing the 5-years average, low-pass filtering has been applied with 24hours or 72 hours cut-off period. **Figure 30** illustrates the time series obtained in both cases (raw, 24h filtering and 72h filtering) in two distinct areas of the Mid-Atlantic Bight: one in the Gulf Stream path, one in the inner shelf in low amplitude mean currents.

A cut-off period of 24 hours was not sufficient to remove efficiently the high-frequency dynamics. Particularly, because at these latitudes, the inertial period is about 20 hours. A cut-off period of 72hours is much more efficient.

The 5-year mean surface currents are computed with the 72hours filtered data and result is given by **Figure 31** together with the difference with 5-year mean surface currents obtained with pre-filtering.

Time-filtering in this case does not change at all the 5-year mean surface currents and average of raw measurements seems a good approach.

Aucune partie de ce document ne peut être reproduite sous quelque forme que ce soit,
ni communiquée, ni utilisée, sans l'accord préalable de CLS.

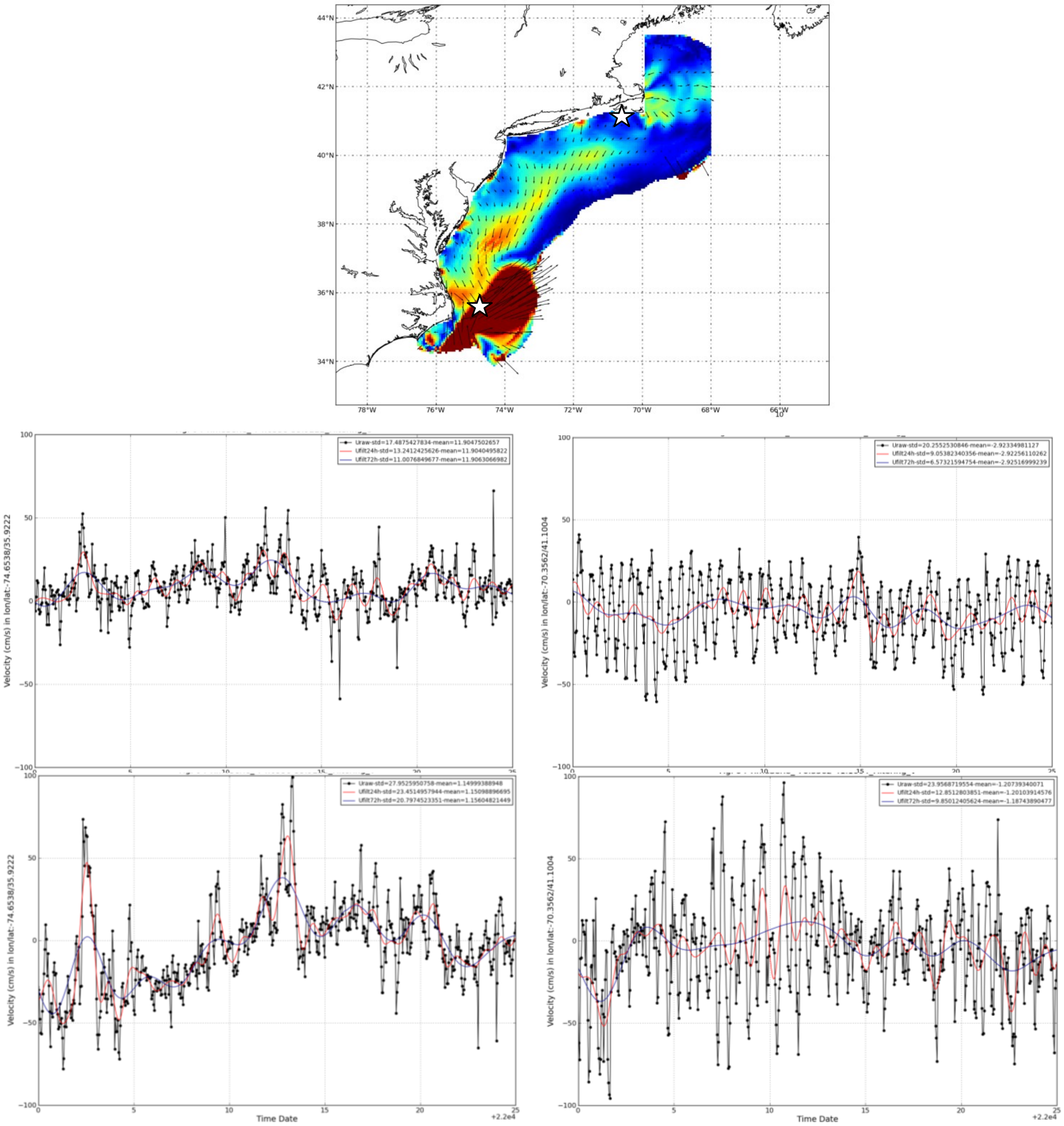

Figure 30 : HF radar surface velocities 25 days-extracted time Series for U (top) and V (bottom) : without time filtering (black), with 24h (red) and 72h low-pass filtering (blue). The white stars on the upper map of Mean Currents give the location of the 2 time series.

Aucune partie de ce document ne peut être reproduite sous quelque forme que ce soit,
ni communiquée, ni utilisée, sans l'accord préalable de CLS.

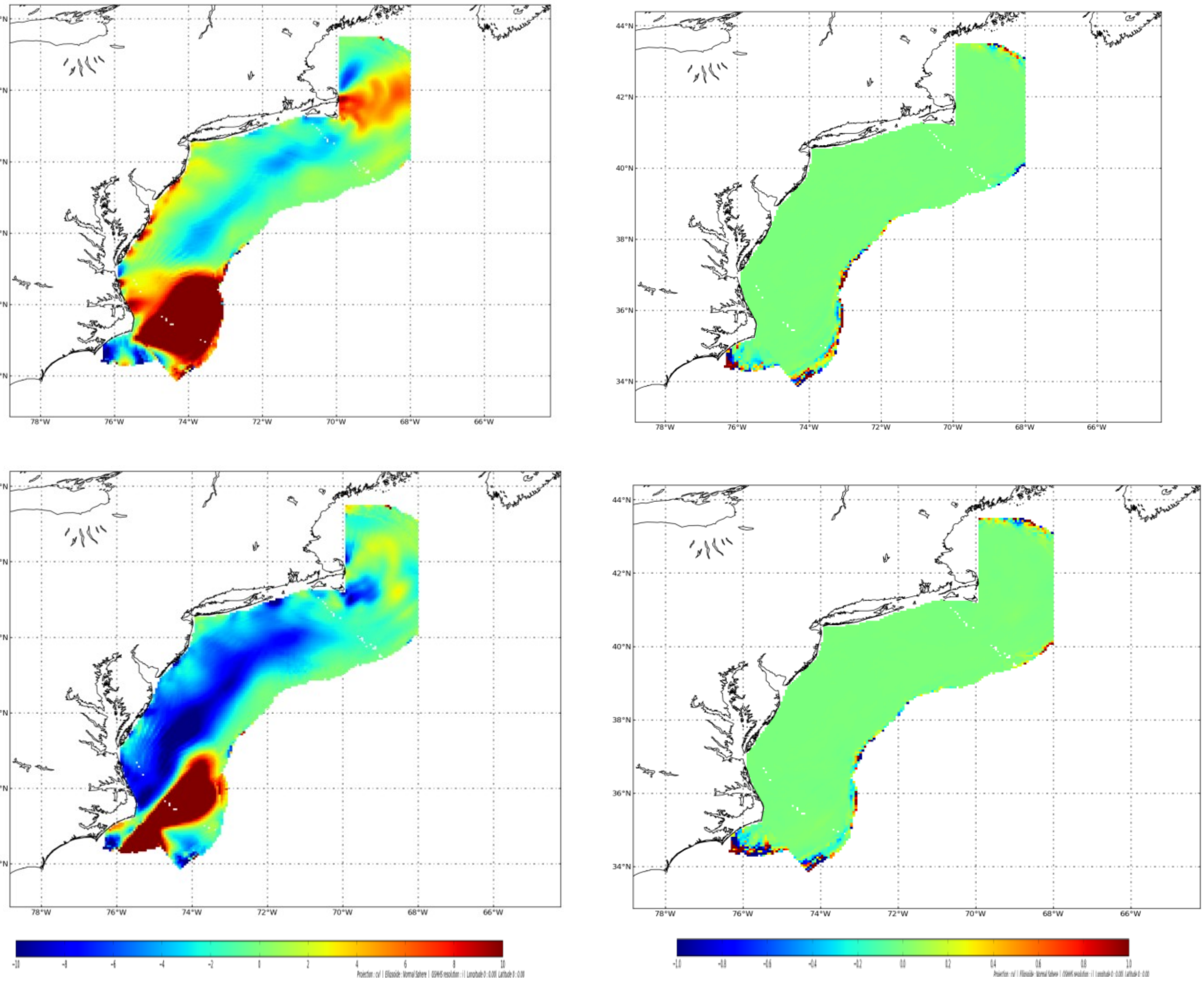

Figure 31 : HF radar surface velocities time-averaged over 2009-2013 after 72 hours low-pass filtering at each grid point (left) and their difference with the same average without time filtering (right). U (top) and V (bottom) in cm/s. |min,max|=10 cm/s for the mean, |min,max|=1 cm/s for the difference.

4.6. Calculation of mean synthetic velocities and potential impact for the calculation of regional MDT

4.6.1. Impact of removing the altimeter velocity anomaly to remove the signal temporal variability referenced to the 20 year period (1993-2012)

As the HF radar measurements are not available over 1993-2012 period, they can only provide an insight of mean geostrophic current over their time coverage, not of a 20 years average as foreseen in MDT field. As shown previously, the mean dynamics of this coastal area changes sensitively from year to year and removing the interannual signal is a mandatory stage.

Usually, this is done using geostrophic current anomalies coming from the Sea Level Anomalies fields: They are used to remove the time variable part over the non-coincident time period and come back to the 20y reference period.

Aucune partie de ce document ne peut être reproduite sous quelque forme que ce soit,
ni communiquée, ni utilisée, sans l'accord préalable de CLS.

Over coastal seas, like the one studied here, this method may be not accurate enough and removing geostrophic currents derived from the maps of SLA may bring much more false signal that right dynamics removal.

In order to evaluate the method, the standard deviation of the HF radar measurements at each grid point is computed after removing the geostrophic current anomalies from the last DUACS DT release interpolated in time and space to the HF radar grid point. Results are given for U and V by **Figure 32.**

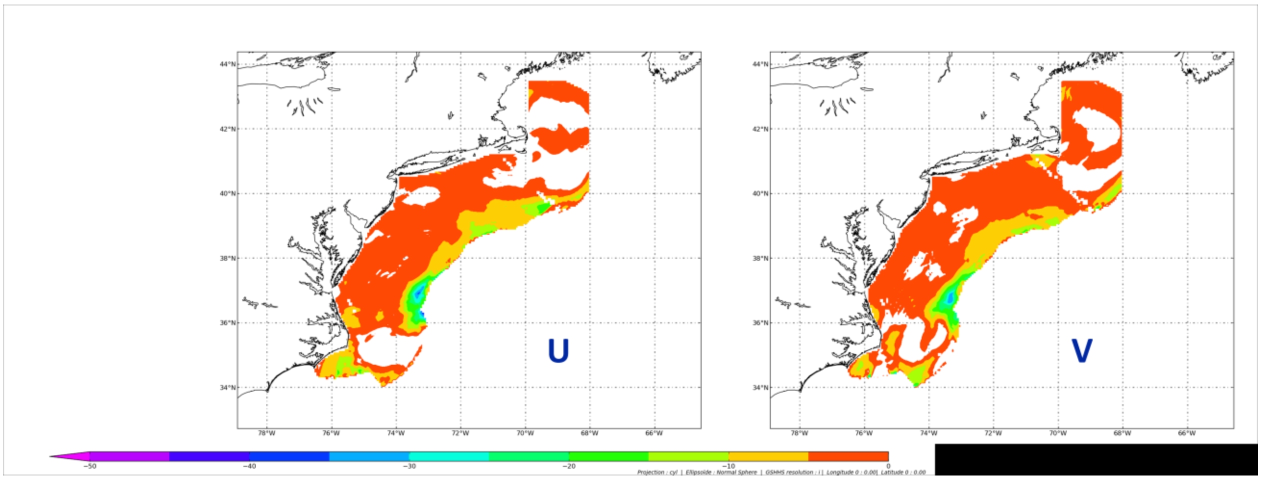

Figure 32 : STD [radar] - STD[radar-geostr_anomalies] over 2009-2013 in cm/s. min=-50cm/s. U (left) and V(right)

Only negative values are plotted dealing with location where removing geostrophic current anomalies adds false signal instead of removing it.

All the orange areas constitute location where the removal of geostrophic current anomalies before computing synthetic means is not appropriated. It concerns a large part of the shelf except the East Cap Cod area. The amplitude of the signal removes in average by this correction [**Figure 33** with a reduced colorbar extension compared to previous figures] is in the -5cm/s – 5cm/s range over the shelf for each component of the current.

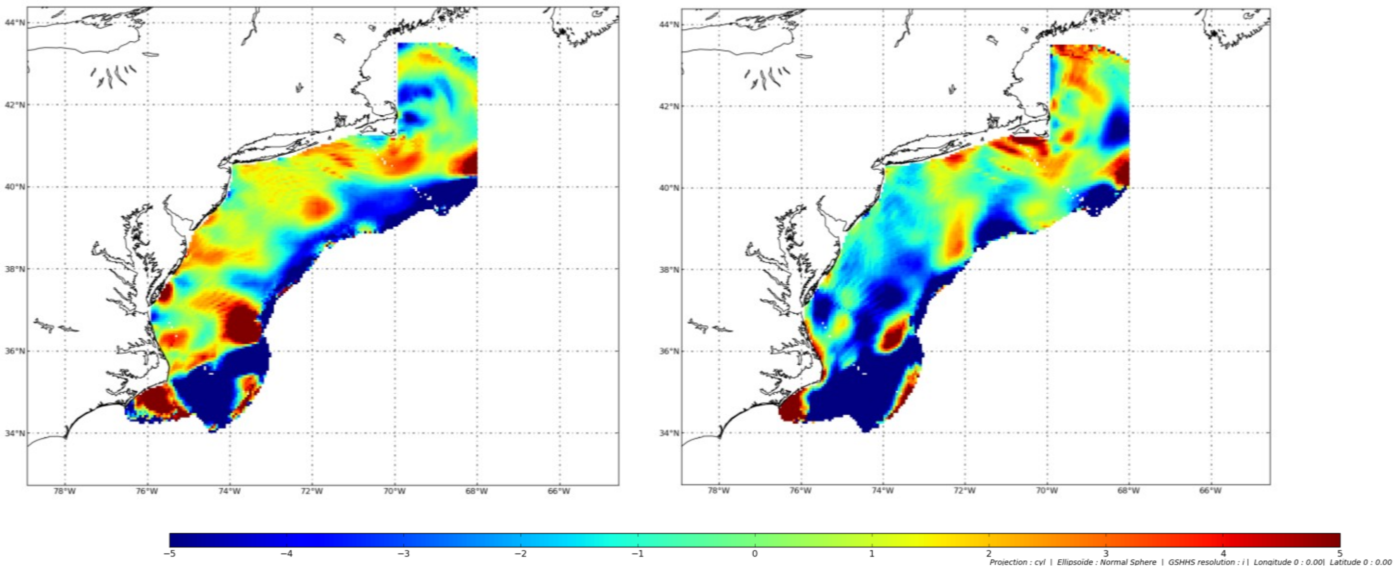

Figure 33 : MEAN [radar] - MEAN[radar-geostr_anomalies] over 2009-2013 in cm/s . U (left) and V(right)

Aucune partie de ce document ne peut être reproduite sous quelque forme que ce soit,
ni communiquée, ni utilisée, sans l'accord préalable de CLS.

4.6.2. Impact of using the surface Ekman model from the CNES-CLS13 MDT study

Another stage in data pre-processing is to remove the low-frequency ageostrophic signals contained in the data and not to figure in the MDT field. These signals are two wind-driven dynamics: The Ekman currents and the Stoke drift.

The computation of a regional MDT with HF radar relies mainly of the estimation of these two wind-driven low-frequency dynamics. In this feasibility study, we first test the new Ekman model estimated at the surface from ARGO floats (Rio et al. 2014) for the global CNES-CLS-2013 MDT computation.

In order to evaluate the method, the standard deviation of the HF radar measurements at each grid point is computed after removing these new surface Ekman currents interpolated in time and space to the HF radar grid point. Results are given for U and V by **Figure 34**..

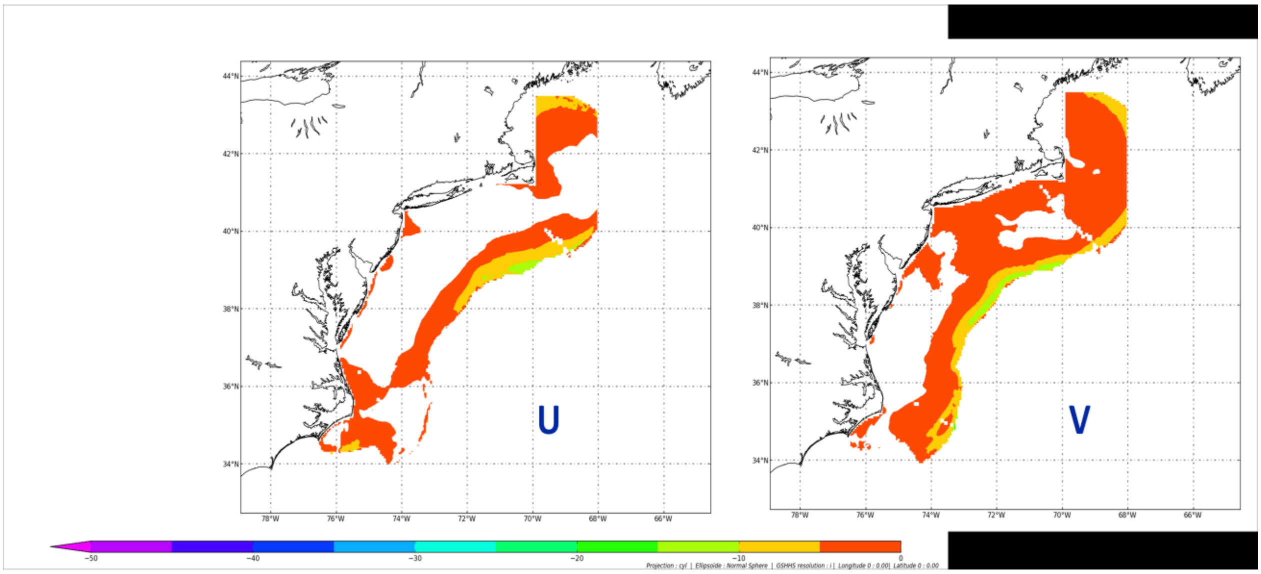

Figure 34 : STD [radar] - STD[radar-Ekman0m] over 2009-2013 in cm/s. min=-50cm/s. U (left) and V(right)

Only negative values are plotted dealing with location where removing Ekman currents adds false signal instead of removing it.

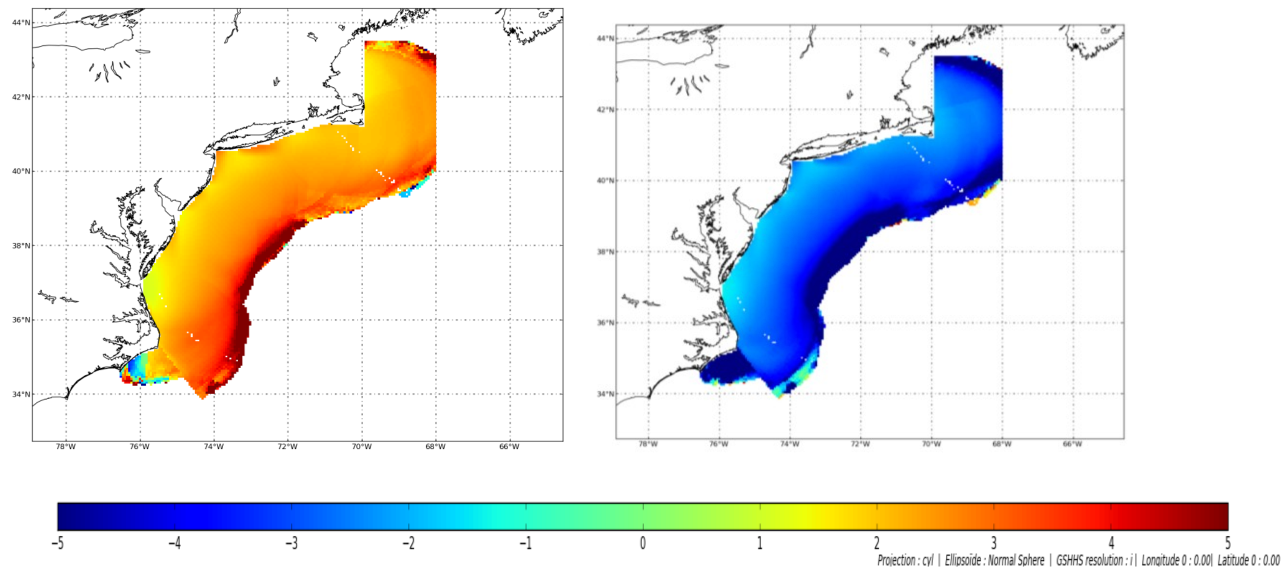

Figure 35 : MEAN [radar] - MEAN[radar-Surface Ekman] over 2009-2013 in cm/s. U (left) and V(right)

Aucune partie de ce document ne peut être reproduite sous quelque forme que ce soit,
ni communiquée, ni utilisée, sans l'accord préalable de CLS.

As for the previous analysis; the orange areas constitute location where the removal of surface Ekman current is not appropriated. Without considering areas where measurement errors are big, these orange regions concern only a very small part of the shelf, meaning that at first order the surface Ekman model fitted on surface drifters does work in this region for estimation Ekman currents.

The amplitude of the signal removes in average by this correction [**Figure 33** with a reduced colorbar extension compared to previous figures] is in the -5cm/s – 0cm/s range for V and 0- 5cm/s range for U over the shelf.

However, as noted in Rio et al (2014), computed angles are smaller than predicted by the Ekman theory (45° at the surface). This is partly due to the fact that Argo floats remain at the surface only few hours before diving again at depth for around 10 days. Consequently we were not able to filter the surface currents from the residual ageostrophic components (inertial oscillations, stokes drift…) and this residual signal in the wind direction leads to smaller deflection angles (10-45°) than theory. Actually, the present model is therefore more an Ekman/stokes model than a pure Ekman model, and is maybe more suited for our purpose since it removes both the Ekman and the Stokes components of the current.

4.6.3. Comparison to mean synthetic velocities from drifting buoys (used in the CNES-CLS13 MDT calculation).

Figure 36a shows the synthetic mean velocities calculated by removing the surface Ekman currents from the HF radar velocities and averaging into 1/8° boxes. We see that a quite coherent and clean signal is obtained in areas where the number of velocities is sufficient (inside the 40000 data isoline from Figure 24). The zonal velocities are rather consistent with the GOCE MDT derived velocities (Figure 36b), while some discrepancy is found between the meridional velocities (5 cm/s northward velocities are obtained with GOCE MDT in the Hudson shelf valley while 5 cm/s southward velocities are obtained in the HF radar measurements. The drifter velocities in this area (Figure 36c), although quite noisy, seems in agreement with the HF radar velocities, so that we might consider that this discrepancy is due to some error in the altimeter MSS used to calculate the GOCE MDT. Interestingly, along the coast between the Delaware Bay and the Cheasapeake bay, HF radar velocities resolve eastward velocities (5-10 cm/s) which are partly also resolved in the GOCE MDT (at least the southern part of the current), while the drifter velocities are quite noisy. From 40°N until North of Cape Hatteras a southeastward running slope current is resolved by all three observing systems (HF radar, GOCE MDT, drifters) even if the drifters see a stronger intensity current (up to -15 cm/s, compare to -10 cm/s for the HF radar velocities). This is most probably due to the fact that, as discussed previously, due to altimeter errors, it is difficult to remove correctly the temporal variability from the drifter velocities, and the sampling of the area by drifters is of course very inhomogeneous over the 1993-2012 time period. This strong drifter mean velocity values is therefore most probably a sampling issue and this highlights pretty well the strong potential impact of using HF radar velocities in this area to improve the MDT solution.

Aucune partie de ce document ne peut être reproduite sous quelque forme que ce soit,
ni communiquée, ni utilisée, sans l'accord préalable de CLS.

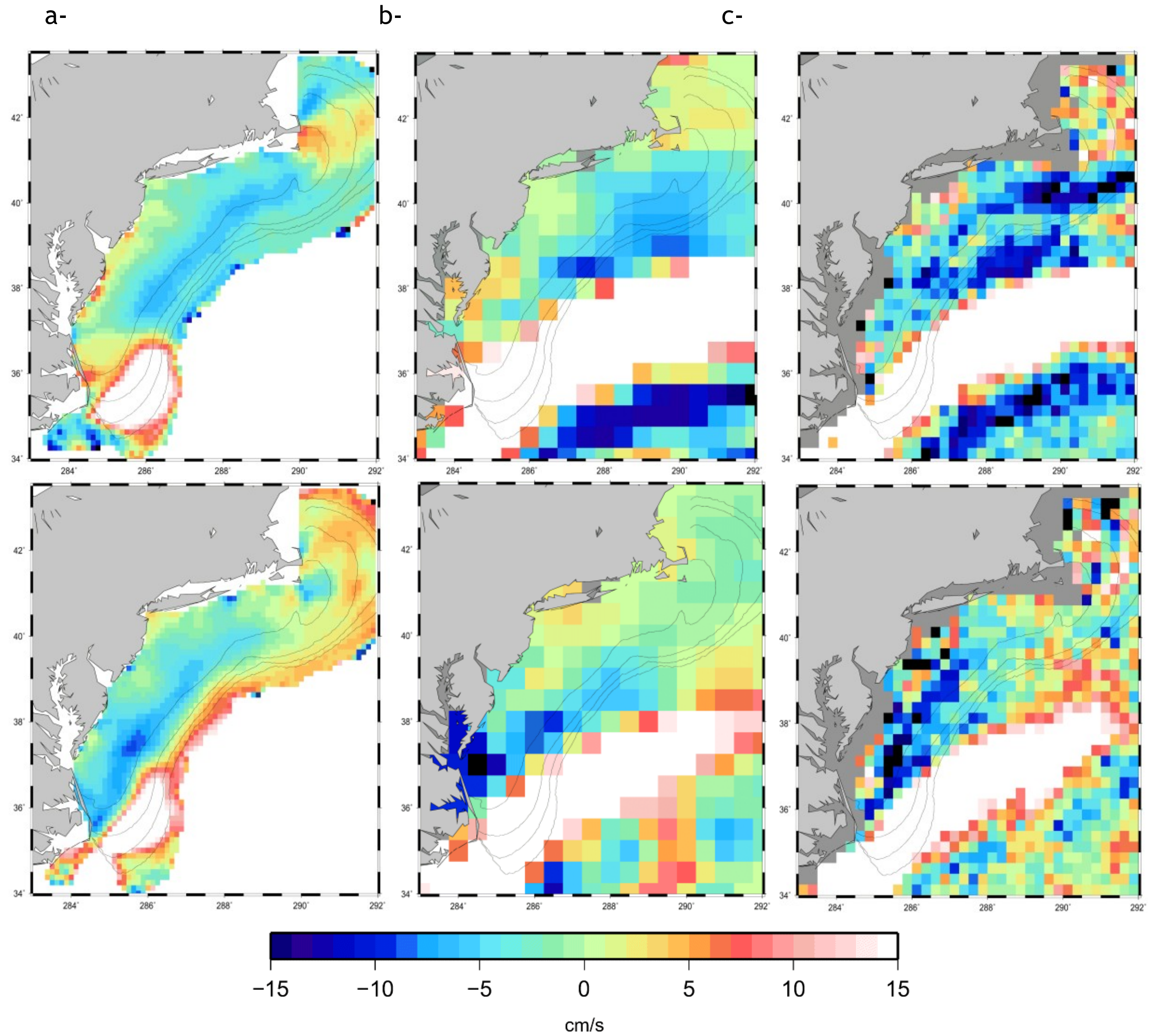

Figure 36 : a- synthetic mean radar velocities calculated by removing the Ekman surface currents from the radar-HF velocities and averaging into 1/8° boxes; b- mean velocities from the GOCE Mean Dynamid Topography; c- synthetic mean velocities from the SVP drifters. Top plots show the zonal velocities while bottom plots show the meridional velocities

4.7. Workplan for future regional MDT calculation

From this analysis, we conclude that the use of HF-radar velocities would strongly benefit the calculation of high resolution MDT in the MAB area. Being punctual, high temporal resolution measurements, the tidal and inertial oscillations average to zero when calculating temporal means. The Ekman currents, and in part the Stokes drift can be modelled and removed using the model by Rio et al (2014) based on the analysis of Argo floats. However, there is still some controversy in the literature about the measurement or not of the Stokes drift by radar HF. It might highly depend on the HF radar wavelength compared to the sea state. HF radar might well measure only part of the Stokes drift. To handle this issue, the priority is to prescribe correct errors on the HF radar velocities, using for instance the mean Stokes drift value as computed in this study.

Aucune partie de ce document ne peut être reproduite sous quelque forme que ce soit,
ni communiquée, ni utilisée, sans l'accord préalable de CLS.

A strong advantage of the HF radar current measurements over the drifting buoy velocities is their Eulerian characteristics. Temporal signal can therefore be removed (averaging) while for drifting buoy velocities, filtering along the drifter trajectory to remove temporal variability also smoothes spatially the velocities.

The HF-radar velocity measurements are therefore quite promising for high resolution MDT calculation.

The main issue however is the poor accuracy of the altimeter Sea Level Anomalies in coastal areas. This prevents us to correctly remove the temporal variability from the HF-radar measurements. Mean velocities from HF-radar would therefore represent the 2009-2013 time period, and not the required 1993-2012 time period. An additional error should therefore be prescribed on the HF radar mean velocities before inversion to handle this issue. A first indication of its amplitude (in the limit of validity of the altimeter measurement of course!) is given by the average, over 2009-2013, of the altimeter SLA (Figure 37). It does not exceed 2 cm/s.

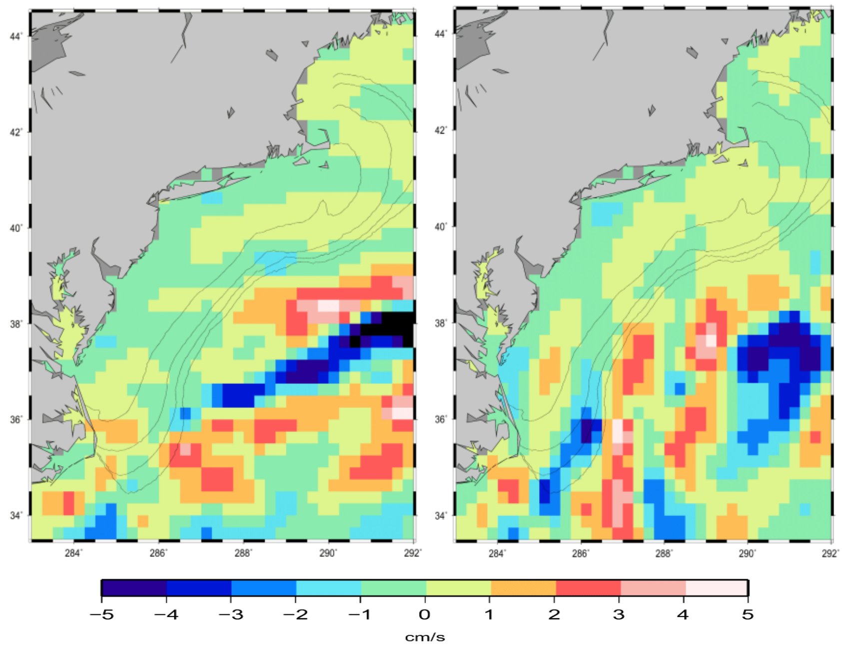

Figure 37 : Average, over the 2009-2013 time period of the SSALTO-DUACS altimeter velocity anomalies (referenced to the 1993-2012 time period). Left: zonal component; Right: meridional component.

Finally, the processed HF-radar velocities should be further averaged into 1/8° boxes before running the multivariate objective analysis. The spatial resolution of the HF radar system is around 6 km, so that we expect to be able to improve the MDT regionally at spatial resolution of the order of 1/10°-1/8° maximum.

Aucune partie de ce document ne peut être reproduite sous quelque forme que ce soit, ni communiquée, ni utilisée, sans l'accord préalable de CLS.

5. Feasibility of using SAR data for the calculation of regional MDT

5.1. SAR measurement principle

The analysis of the ASAR (Advanced Synthetic Aperture Radar) images from the ENVISAT mission has been shown to yield valuable near surface wind speed and ocean surface current information (Chapron et al. 2005; Johannessen et al. 2008; Rouault et al. 2010; Hansen et al. 2011; Mouche et al. 2012).

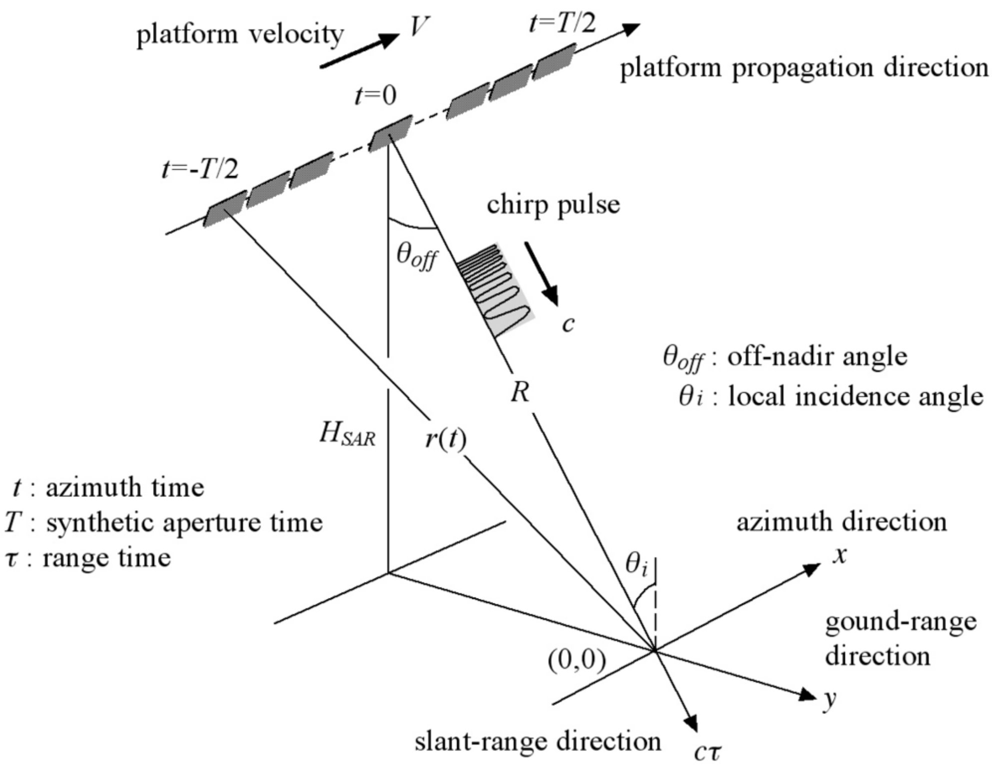

Figure 38 : SAR geometry

The measurement of the surface current velocities is based on the analysis of the phase change between the transmitted and received signal due to the Doppler effect: A Doppler shifts of C-band radar return signals is measured due to the relative motion between the sea surface scattering elements and the platform (see Figure 38 for the geometry of the SAR measurement). This relative motion is due both to the known movement of the satellite in orbit, and to the movement of the scattering elements of the sea surface by the underlying currents. Over the ocean, the predictable frequency shift associated with the motion of the satellite relative to the Earth dominates the Doppler shift. Removing this shift yields the residual ***Doppler centroïd anomaly***, related to the line-of-sight (range) Doppler velocity of the sea surface. This includes the phase velocity of short wind-waves at Bragg-scales, the circular motion and breaking of larger waves, and any surface current. At first order, this Doppler shift is highly correlated to the wind speed (Figure 39).

Aucune partie de ce document ne peut être reproduite sous quelque forme que ce soit,
ni communiquée, ni utilisée, sans l'accord préalable de CLS.

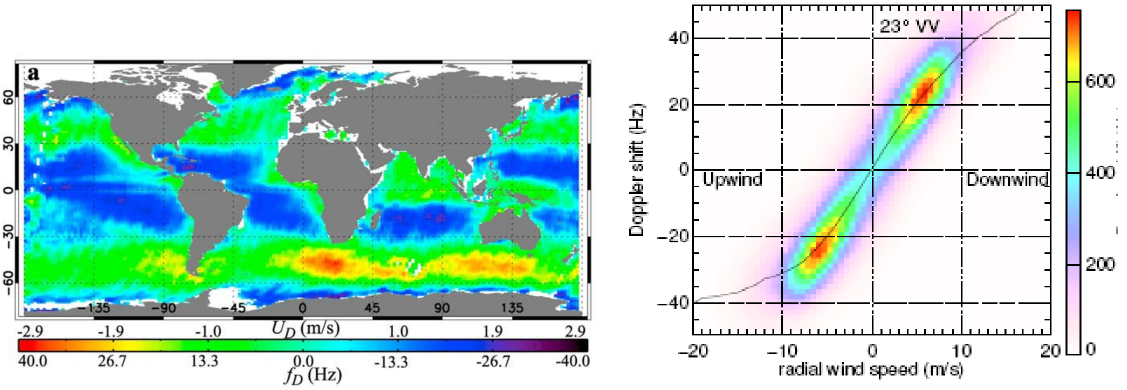

Figure 39 : Left: Gridded 35-day average (January-February 2004) of Doppler anomaly fDca, also converted to surface velocity UD (positive for directions away from the satellite) for imagettes acquired by ENVISAT over descending tracks, and thus looking to the west-northwest. The anomaly patterns are well correlated with the general atmospheric circulation. Right: Doppler shift as a function of radial wind speed. From Chapron et al (2005)

Chapron et al. (2005) revealed how the sensitivity of range Doppler velocity to surface current and wave motion depends on wind speed and direction in a manner that can be exploited to yield precise surface current estimates. Subsequent studies using a radar-imaging model (DopRIM; Johannessen et al. 2008, Hansen et al. 2012) found that range Doppler velocity can be approximated as a linear sum of wind induced sea surface velocities and the sea surface current in the radar line-of-sight direction. The wave-state contribution can then be estimated using an empirical relationship between the range Doppler velocity and the near surface wind field, as demonstrated by Mouche et al. (2012) with a C-band Doppler (CDOP) algorithm. **These local wind contributions are mainly from wave orbital motion, but also from Ekman and Stokes drift**. When this is subtracted from the observed Doppler centroïd anomaly, a measure of the sea surface current in the range direction is obtained that therefore contains the contributions, projected onto the range direction, of the geostrophic currents, the tidal currents, the inertial oscillations.

Aucune partie de ce document ne peut être reproduite sous quelque forme que ce soit, ni communiquée, ni utilisée, sans l'accord préalable de CLS.

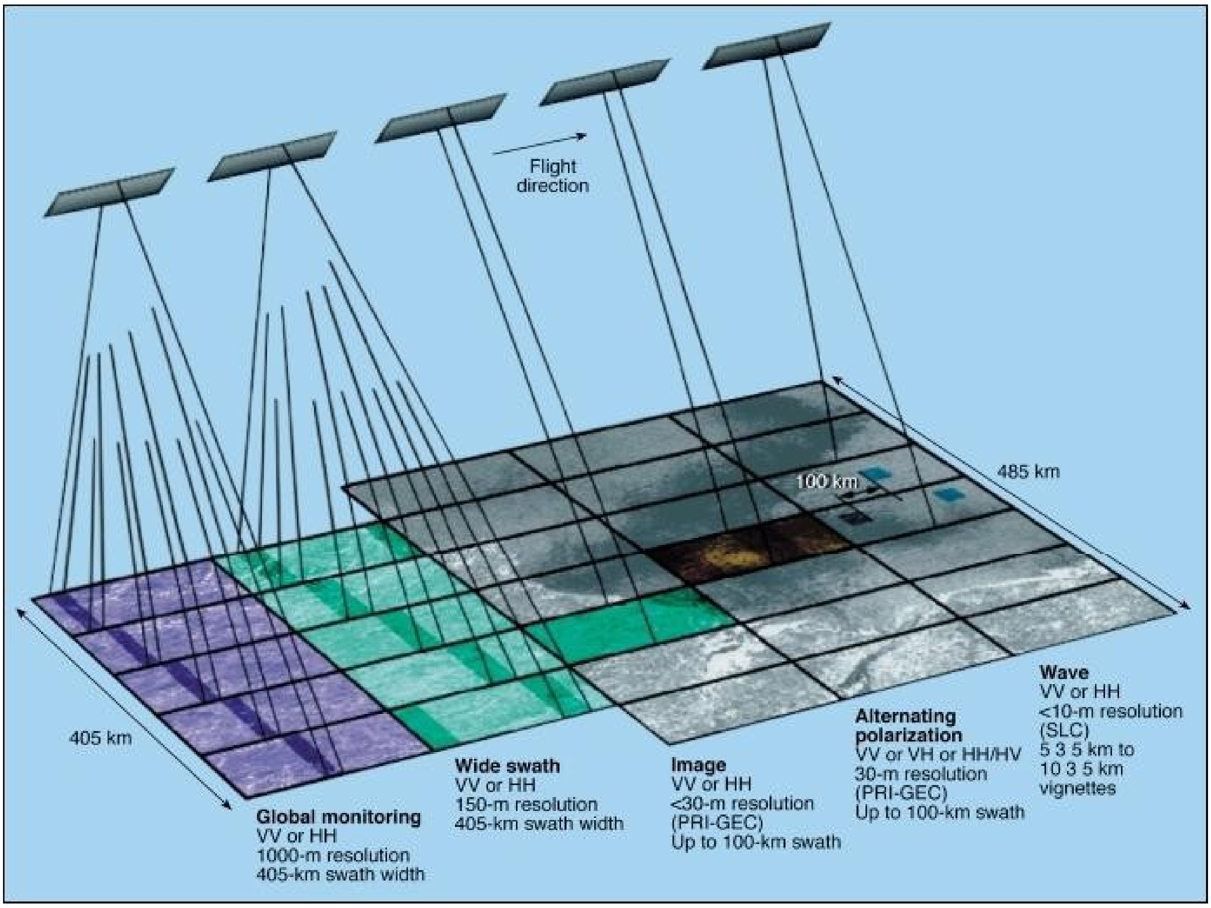

Figure 40 : ENVISAT ASAR mode. The Wide swath mode images are used in this study.

The derivation of surface current velocities from the Doppler centroïd anomaly can then be summarized as a three-step process: (1) calculating the Doppler centroïd anomaly by removing the relative motion of the satellite to the Earth, (2) removing the wind-induced contributions from the total Doppler centroïd anomaly and, (3) converting the Doppler centroïd anomalies to range-directed surface velocities. The ASAR-derived velocities provide a measure of the absolute surface current velocity across the track of the satellite, with positive values indicating a flow moving away from the radar. The ASAR range velocity product has a resolution of about 4 km in range and 8 km in azimuth [Collard et al., 2008]. Over the Agulhas Current region, one descending (morning) and one ascending (evening) ASAR Wide Swath Mode image (Figure 40) has been obtained every 3.5 days since July 2007.

Figure 41 illustrates the retrieval of these surface current velocities from the raw SAR images (top left).

In practice, uncertainty in the retrieved SAR range Doppler velocity fields from Envisat ASAR hampers the applicability of the range Doppler velocity method. As shown by (Hansen et al. 2011) a 5-Hz uncertainty is present in the Doppler shift retrieved from Envisat ASAR acquisitions. With the Sentinel-1 processor, the uncertainty in the retrieved geophysical Doppler shift is expectedly reduced to 2-3 Hz.

Aucune partie de ce document ne peut être reproduite sous quelque forme que ce soit,
ni communiquée, ni utilisée, sans l'accord préalable de CLS.

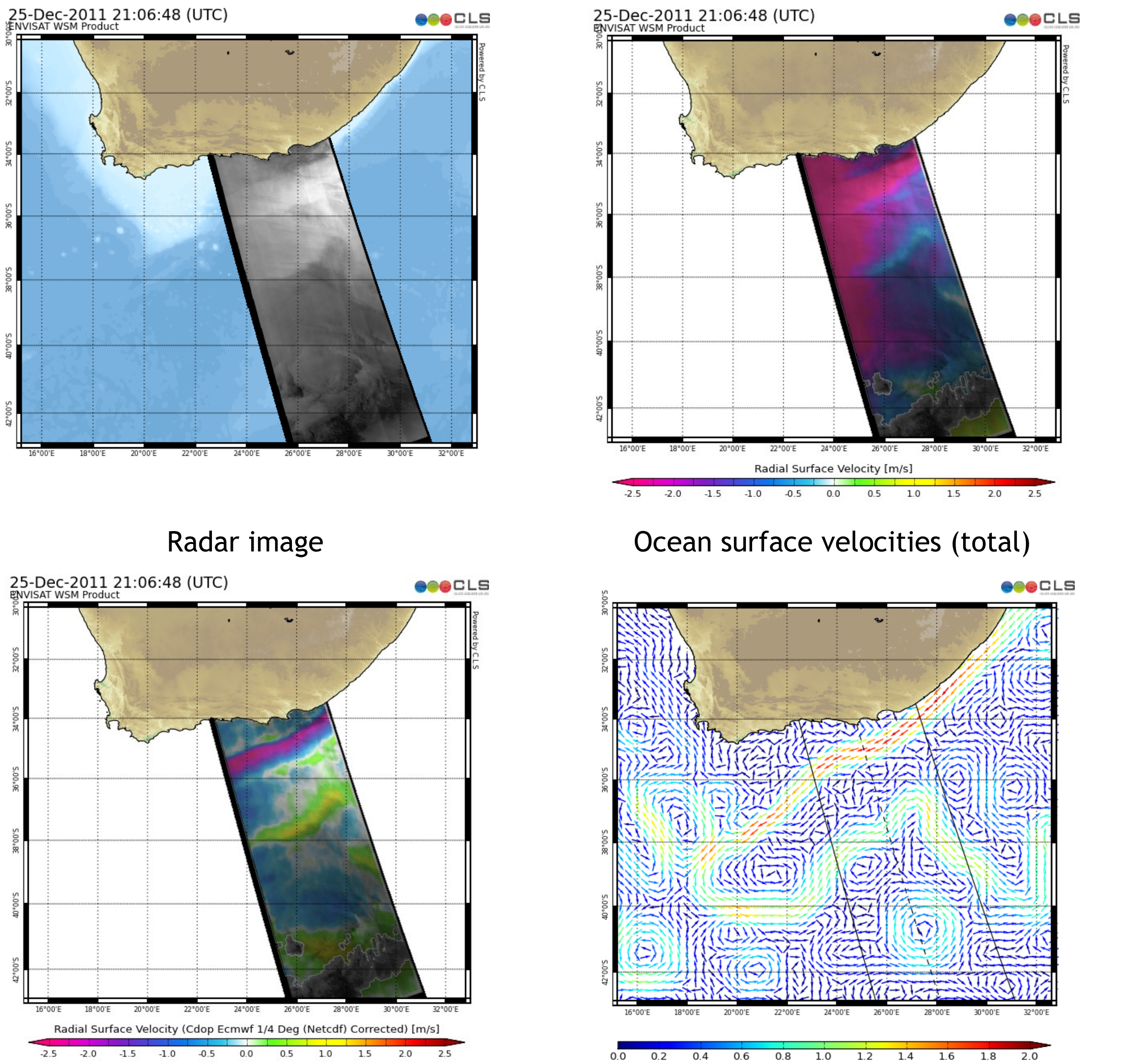

Radar image

Ocean surface velocities (total)

Ocean surface velocities (corrected from sea state)

Ocean surface current (Duacs)

Figure 41 : Illustration of the range velocity retrieval (lower left) from the initial SAR image (upper left) with intermediate ocean surface velocity field (upper right). A comparison with the colocated DUACS situation is shown (lower right). (Illustrations provided by A. Mouche).

As for land-based radar measurement systems, only one component of the surface current velocity (in the range direction) is therefore extracted from the analysis of the Doppler shift. However, radial velocities from ENVISAT ascending and descending paths may be combined to reconstruct the total current vector. Two main issues are encountered: First, both paths are obviously not simultaneous, which prevents from reconstructing instantaneous velocity vectors from SAR data. However, in our study, where the objective is to reconstruct mean currents, mean radial velocities can be estimated from ascending paths data and descending paths data separately and combined in a successive step. This processing will be described in section 5.3.3. Second, ideally the two paths should be perpendicular, which is not the case. The angle between the two paths in the Agulhas current area is 30°. This results in strong uncertainties on the reconstructed velocities (mainly the meridional component, due to the polar orbit of the satellite). A method is proposed in section 5.3.4 to overcome this limitation.

Aucune partie de ce document ne peut être reproduite sous quelque forme que ce soit,
ni communiquée, ni utilisée, sans l'accord préalable de CLS.

5.2. Data available for the study

Over the Agulhas current and for years 2009, 2010 and 2011, we dispose of 563, 403 and 243 SAR images, respectively. The region of interest is limited by lon/lat coordinates [17.5°, 32.5°], [-42.5°, -27.5°]. The range velocities derived from the ASAR measurements are originally available in the SAR image geometry. First, only SAR measurements at incidence angles larger than 30° have been considered in the time averages. Indeed, a potential source of error in the SAR-derived range velocity comes from inaccurate wind field predictions at low incidence angles [Roualt et al. 2010].

Then, in order to be combined with other ASAR measurements, range velocities are all interpolated to a 1/8° regular grid. All the following analysis will be presented on this regular grid. As for the drifter velocities, they are provided on a 1/8° regular grid. The altimeter velocities are provided on a 1/4° regular grid and are thus extrapolated.

5.3. Analysis

5.3.1. Analysis of SAR range velocities from ascending/descending passes

The Agulhas Current area has been identified by ESA as a super-site with quasi-systematic acquisition starting in 2007. The geographical coverage of the SAR data acquired between January 2009 and December 2011 is shown on **Figure 42** for ascending and descending passes.

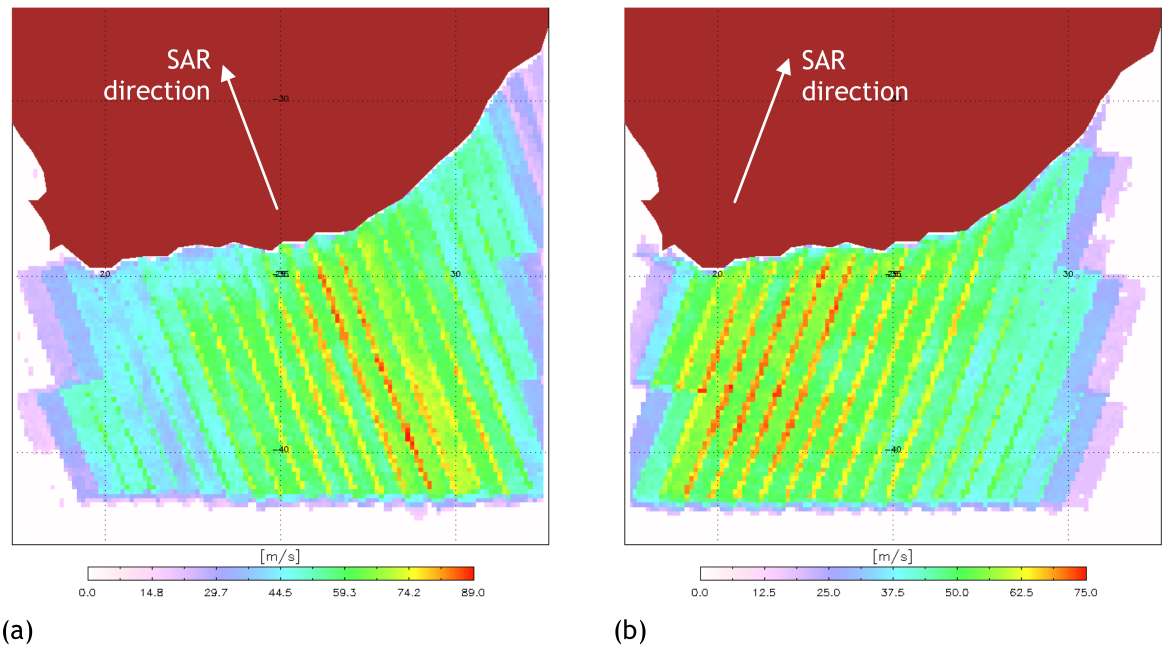

Figure 42: Data samples over the Agulhas Current area for Ascending (a) and Descending (b) passes.

The corresponding mean range velocities are presented in **Figure 43**. From **Figure 43**-a and -b, both the main Agulhas current and Agulhas current retroflection can be identified. Since the current velocity is available in range direction only, the sensor geometry is of great matter for surface currents observation. For the Agulhas main and retroflection currents, the range direction given by the ascending passes is best suited.

The standard deviation is also estimated for ascending and descending passes on From **Figure 43**-c and -d. Larges values can be found for mainly three reasons:

- In some regions, there are not enough data samples to derive signal statistics. This is especially true on the map boundaries.

Aucune partie de ce document ne peut être reproduite sous quelque forme que ce soit,
ni communiquée, ni utilisée, sans l'accord préalable de CLS.

- The mean stream of the Agulhas current can move in space and time, which increases the standard deviation. The largest value is obtained for the edge of the main current (map center) which also corresponds to the maximum velocities.
- Errors in the range velocity estimates.

Also the effects of tidal currents and inertial oscillations are not removed from the range velocities measurements. In order to do so, a *priori* information would be necessary, possibly taken from a model. Possibilities are to retrieve the tidal current from a global model such as FES 2012 and to estimate the mean amplitude of the inertial oscillations to prescript this error when comparing altimeter or drifters to SAR.

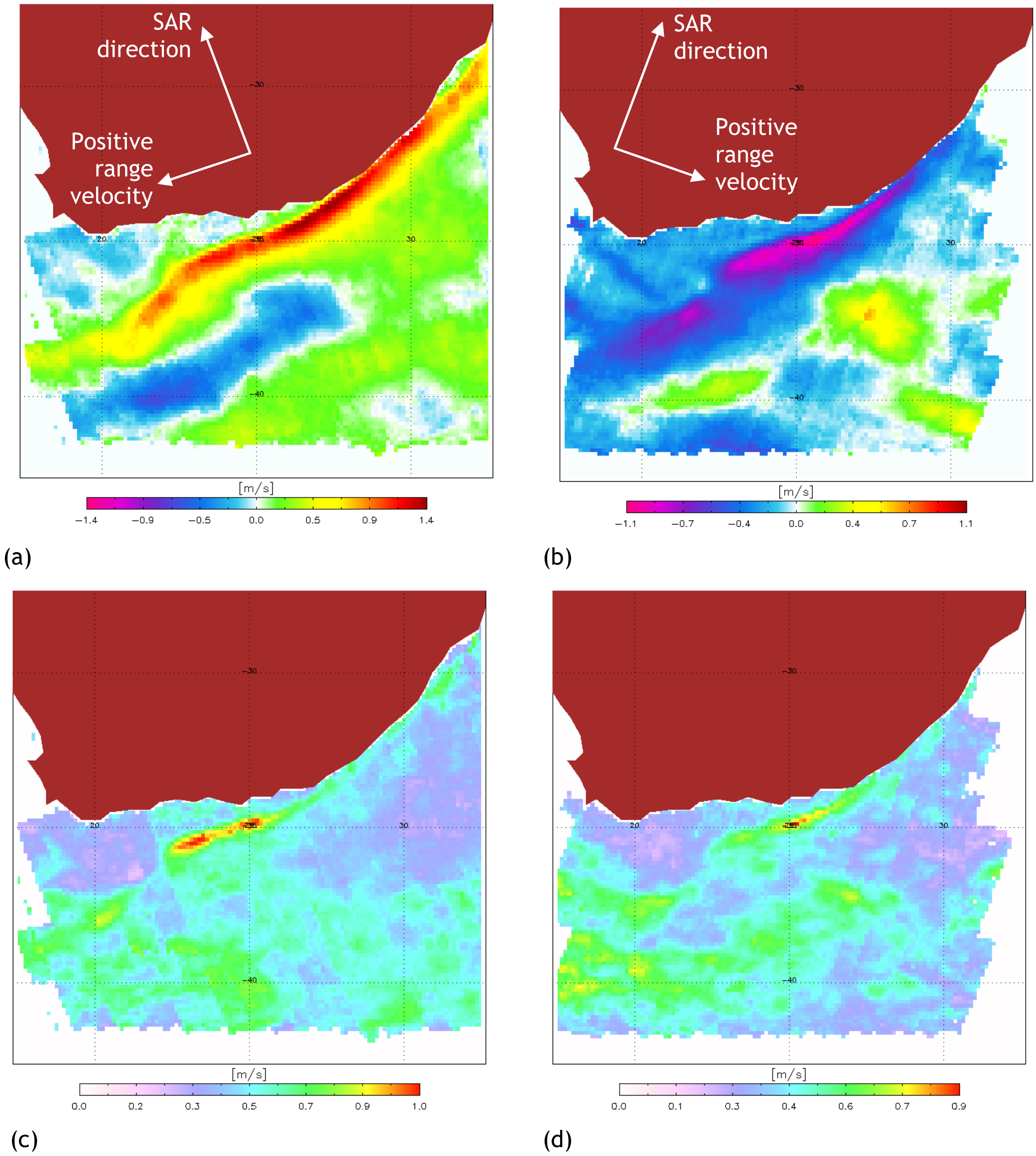

Figure 43: Average range velocities over the Agulhas Current area for Ascending (a) and Descending (b) passes, and associated standard deviations (c) and (d). Range velocities are positive for currents directed toward the sensor.

Aucune partie de ce document ne peut être reproduite sous quelque forme que ce soit, ni communiquée, ni utilisée, sans l'accord préalable de CLS.

5.3.2. Comparison with velocities given by drifters and altimeters projected along the SAR range axis

In order to compare these velocity measurements to the one provided by drifters and altimeters, they need to be projected on the same axis. This operation is done taking into account the track angle of the SAR platform at the SAR image location.

Differences between these three velocity measurements can partly be explained by:

- Estimation methodology: the fact that tidal currents and inertial oscillations are not taken into account in the SAR-derived range velocities differ from drifters and altimeters. This is not corrected in the present study.
- Different space/time sampling between the three observing systems: time averaged range velocities with different time sampling can be compared only if it is assumed that the time variability is small. Thus, we choose to limit the comparison to regions where the relative standard deviation of the total current velocity is smaller than 200%. Since altimeters provide the best space/time sampling, this parameter is estimated as follows:

$$\frac{\sigma^{alti}}{V^{alti}} = \frac{\sigma_u^{alti}\left|u^{alti}\right| + \sigma_v^{alti}\left|v^{alti}\right|}{\left(V^{alti}\right)^2}$$

Where, σ^{alti} is the standard deviation of the surface current velocity given by the altimeters

σ_u^{alti} is the standard deviation of the zonal component of the surface current velocity given by altimeters

σ_v^{alti} is the standard deviation of the meridional component of the surface current velocity given by altimeters

V^{alti} is the absolute surface current velocity given by altimeters

- Error estimates related to each of these velocity measurements: the signal to noise ratio in the time averaged signal increases with the number of samples. We choose to limit the comparison to regions with a minimum data samples equal to 50.

A mask is derived from these last two conditions and used to restrict the matchups between SAR and altimeter-derived measurements on one hand and SAR and drifters-derived measurements on the other hand. Average velocities projected along range direction are shown for altimeters and drifter-derived measurements on **Figure 44**. For comparison, the SAR-derived measurements restricted to the corresponding mask are also shown on **Figure 45**.

From these different measurements, it can be seen that the Agulhas main and retroflection current patterns are visible on the range velocities given by SAR, drifters and altimeters. However, they differ in shape and amplitude. The sharp edge and the large amplitude of the Agulhas main current is well represented by the SAR and the drifter measurements both for ascending and descending passes while altimeters exhibit a smoother edge, which directly results from the data resolution. Also, some significant differences are visible:

- The retroflection part of the current part exhibits the largest differences. Specifically, the South-East side of the map, within the green box for the ascending passes, shows a different sign between the SAR and the altimeter or the drifter measurements.

Aucune partie de ce document ne peut être reproduite sous quelque forme que ce soit,
ni communiquée, ni utilisée, sans l'accord préalable de CLS.

- The southward boundary of the Agulhas main current between 20 and 30°W latitudes (region within the black box for the ascending passes on **Figure 45**) has higher amplitude in the SAR signal.

These two regions also correspond to the area where the standard deviation of the altimetric current velocity reaches its highest relative values (**Figure 46**). The particular SAR temporal sampling could therefore explain these differences.

Altimeter

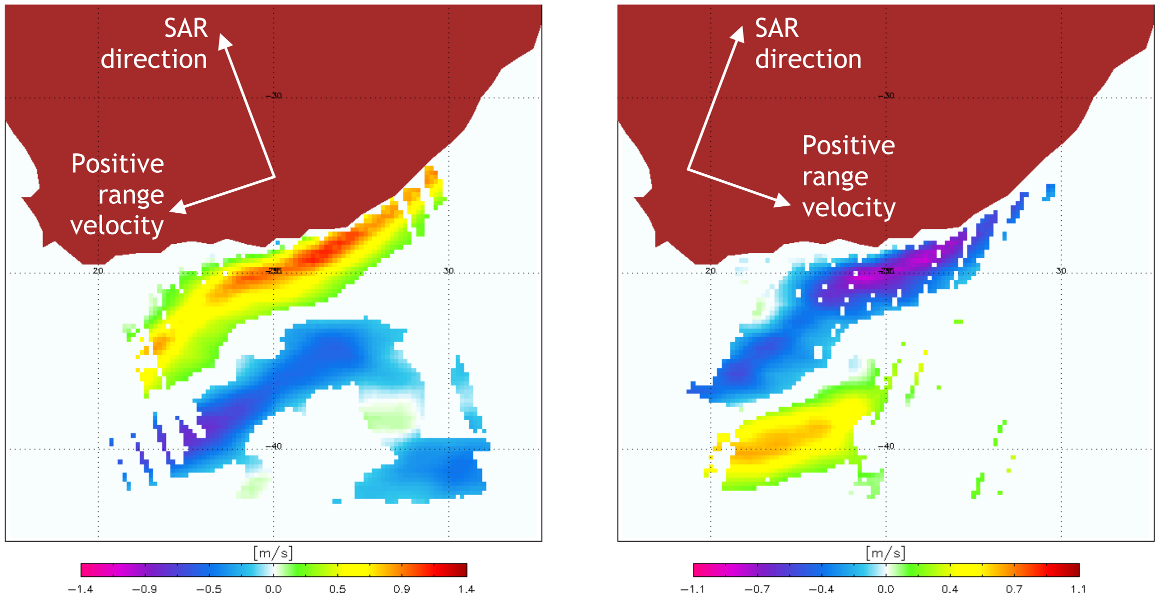

(a) (b)

Drifters

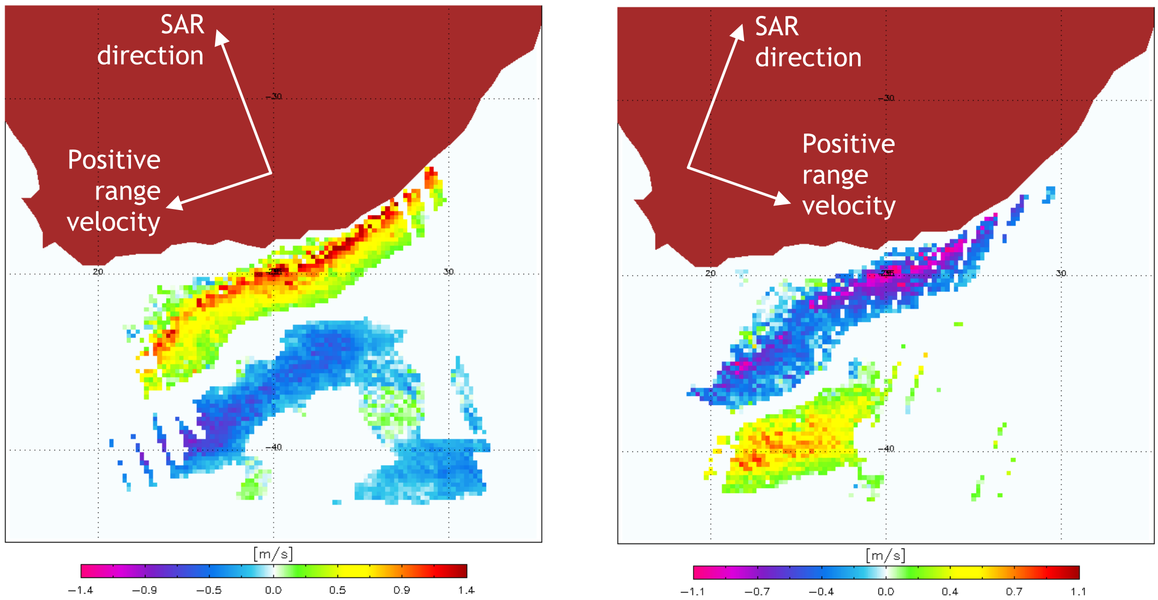

(c) (d)

Figure 44: Masked average velocities over the Agulhas Current area given by the altimeter and projected along the SAR range direction for Ascending (a) and Descending (b) passes, and given by the drifters and projected along the SAR range direction for Ascending (c) and Descending (d) passes. Range velocities are positive for currents directed toward the sensor.

Aucune partie de ce document ne peut être reproduite sous quelque forme que ce soit,
ni communiquée, ni utilisée, sans l'accord préalable de CLS.

SAR

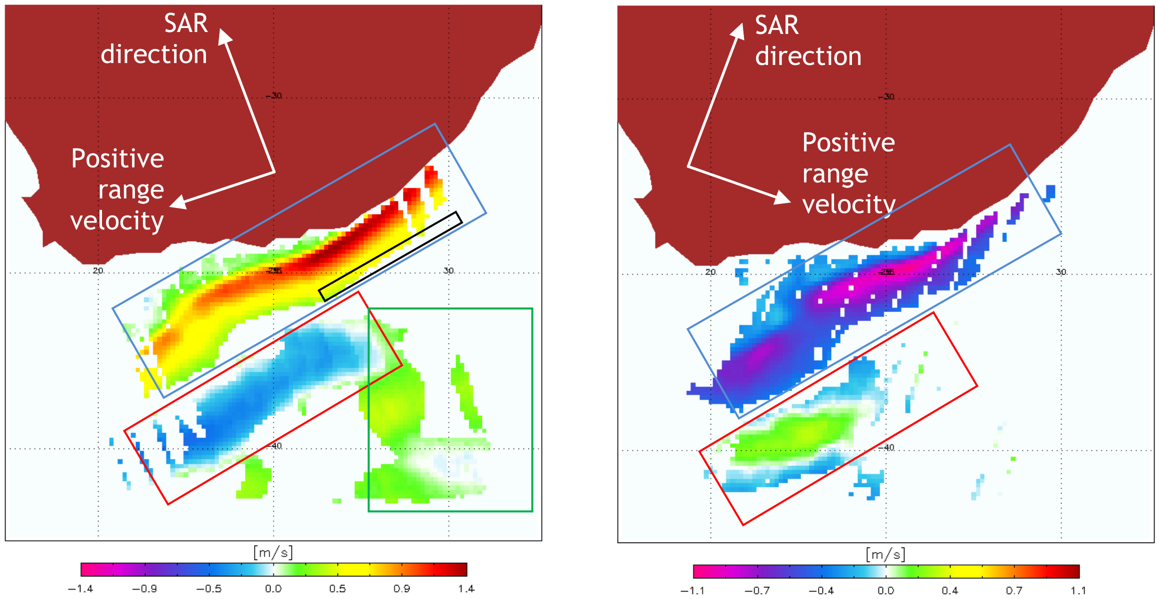

(a) (b)

Figure 45: Masked average range velocities given by SAR-derived measurements over the Agulhas Current area for Ascending (a) and Descending (b) passes. The blue, red and green boxes have statistical characteristics shown in Figure 47.

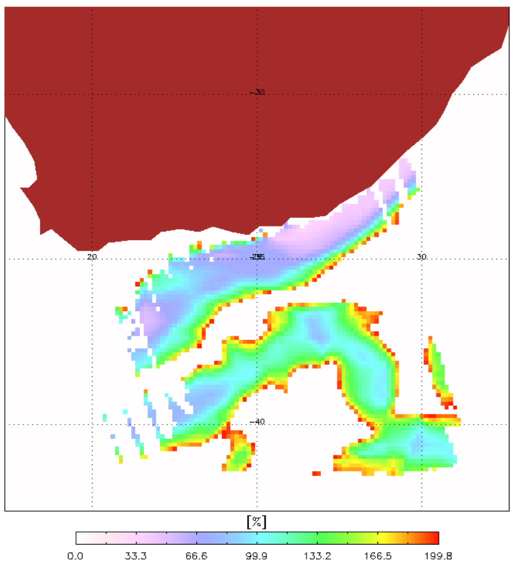

Figure 46: Standard deviation of the altimeter-derived range velocity measurements relatively to the range velocity absolute value, limited to the masked area for ascending passes.

Scatter plots are provided on **Figure 47** in order to compare SAR and altimeter-derived on one hand and SAR and drifter-derived measurements on the other hand.

Aucune partie de ce document ne peut être reproduite sous quelque forme que ce soit, ni communiquée, ni utilisée, sans l'accord préalable de CLS.

Altimeter

Ascending

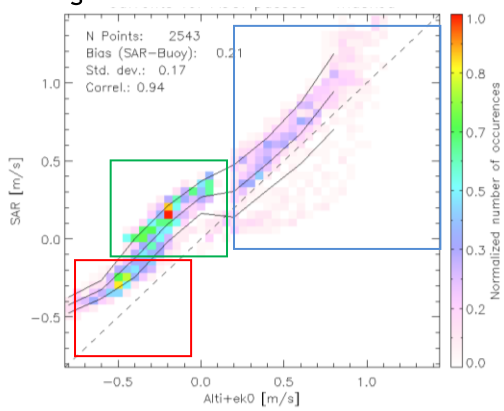

(a)

Descending

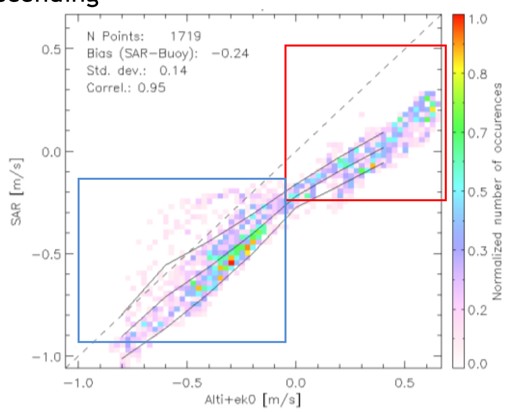

(b)

Drifters

Ascending

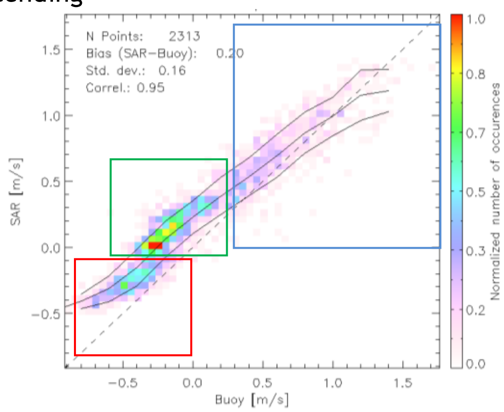

(c)

Descending

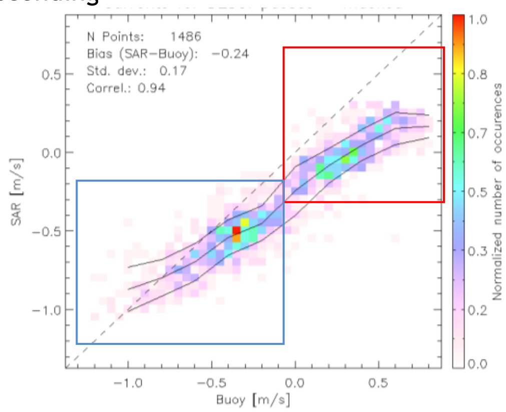

(d)

Figure 47: Scatterplots of masked average range velocities over the Agulhas Current area for SAR to altimeter-derived measurements for Ascending (a) and Descending (b) passes, and SAR to drifter-derived measurements for Ascending (c) and Descending (d) passes. Range velocities are positive for currents directed toward the sensor. The blue, red and green boxes have statistical characteristics corresponding to regions shown in Figure 45.

The different behavior described in the previous map comparison can be identified in the scatterplots. They are represented on the top two graphs:

- The Agulhas main current (blue box), shows positive and larger (smaller) value for the SAR than for the altimeter for ascending passes (for descending passes). For the ascending passes, a significant number of points are located under the X-Y axis bisector. They correspond to the sharp edge signal well represented in the SAR and drifter signal but smoothed in the altimeter signal. The largest values (positive for ascending passes and negative for descending passes) correspond to the strongest currents of the Agulhas circulation and are in good agreement between the SAR and the drifters. Both SAR and drifters resolve stronger intensity in this current than altimetry. This is therefore where we expect the use of SAR velocities to contribute to the calculation of high resolution regional MDTs.

Aucune partie de ce document ne peut être reproduite sous quelque forme que ce soit, ni communiquée, ni utilisée, sans l'accord préalable de CLS.

- The tip of the retroflection current (green box) shows small amplitude signal of opposite signs for the SAR and the altimeter or drifters.
- The beginning of the retroflection current (red box) shows under-estimated range velocities for the SAR compared to the altimeter or the drifters.

Because each part of the scatterplot corresponds to regions of the Agulhas region with different characteristics in term of time-persistency, signal intensity, spatial resolution ..., statistics need to be estimated for each of them rather than globally. They are presented for the red and blue boxes in Table 2.

Table 2: Statistics for the blue and red boxes for SAR vs. Altimeter and SAR vs. Drifter range velocities

Ascending		
	Altimeter	Drifter
Points	983	770
Bias	0.10	0.09
Std. Dev	0.19	0.17
Correlation coefficient	0.81	0.84

Descending		
	Altimeter	Drifter
Points	978	754
Bias	0.17	-0.14
Std. Dev	0.11	0.15
Correlation coefficient	0.82	0.77

Ascending		
	Altimeter	Drifter
Points	539	534
Bias	0.23	0.19
Std. Dev	0.07	0.11
Correlation coefficient	0.86	0.72

Descending		
	Altimeter	Drifter
Points	667	660
Bias	-0.36	-0.34
Std. Dev	0.08	0.14
Correlation coefficient	0.89	0.73

Aucune partie de ce document ne peut être reproduite sous quelque forme que ce soit, ni communiquée, ni utilisée, sans l'accord préalable de CLS.

5.3.3. Current velocity vector estimates using a combination of the ascending and descending range velocities from SAR.

Since SAR-derived range velocities are provided in two non-collinear directions, it is theoretically possible to reconstruct a current vector using a combination of the ascending and descending averages. The zonal and meridional components of the current can be estimated as follows:

$$u = \frac{(V_a - V_d)}{2\cos(\alpha_d)}$$

$$v = \frac{(V_a + V_d)}{2\sin(\alpha_d)}$$

Where, α_d is the track angle for descending passes. It is approximately equal to -165°

V_a and V_d are the mean range velocities for ascending and descending passes

Since the range and zonal direction form an angle of 15°, the zonal component is a much more appropriate for this reconstruction than the meridional one. Still, they are both represented for SAR, altimeter and drifters on **Figure 48** and **Figure 49**.

SAR

Zonal Meridional

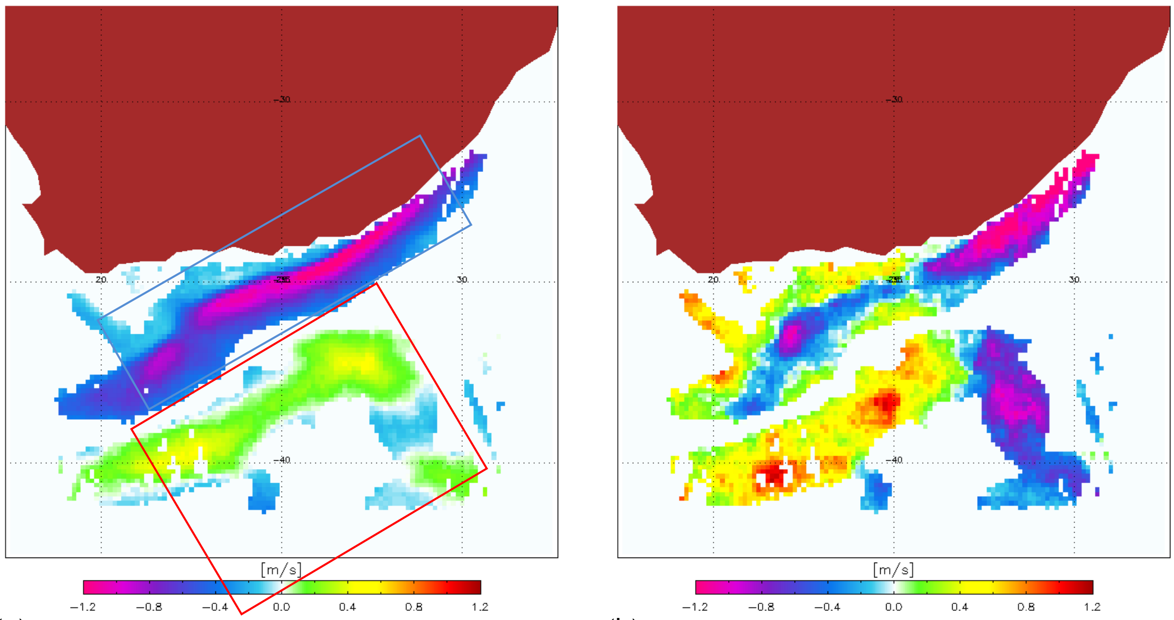

(a) (b)

Figure 48 : Masked average zonal (a) and meridional (b) velocity over the Agulhas Current area given by the SAR. The blue and red boxes have statistical characteristics shown in Figure 50.

Aucune partie de ce document ne peut être reproduite sous quelque forme que ce soit, ni communiquée, ni utilisée, sans l'accord préalable de CLS.

Altimeter

Zonal

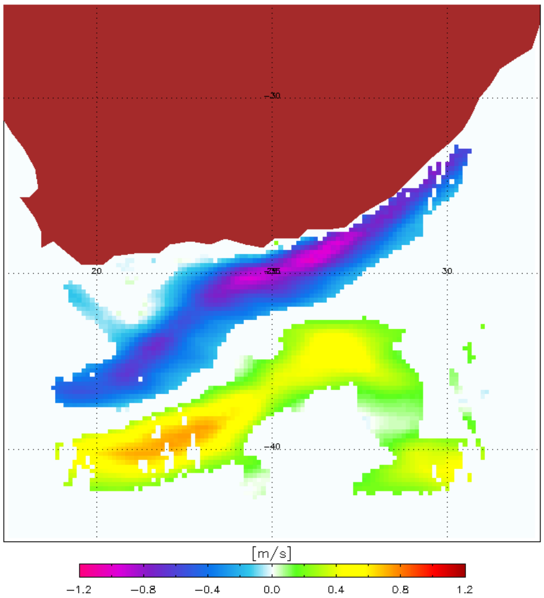

(a)

Meridional

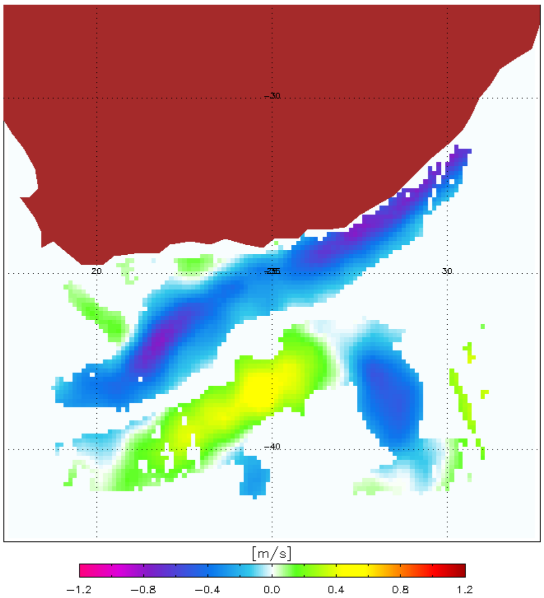

(b)

Buoy

Zonal

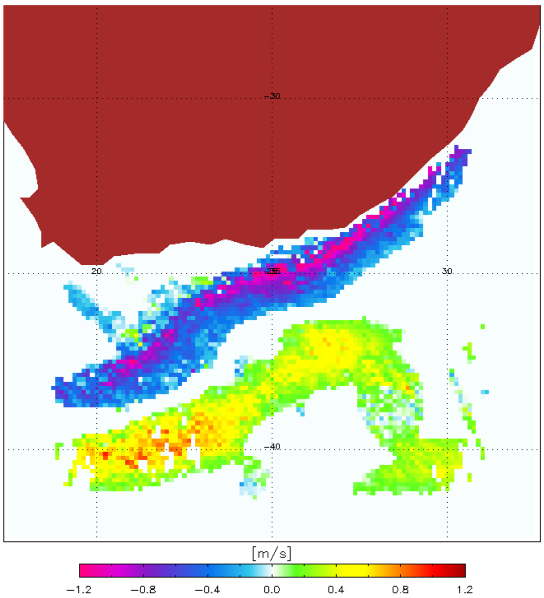

(c)

Meridional

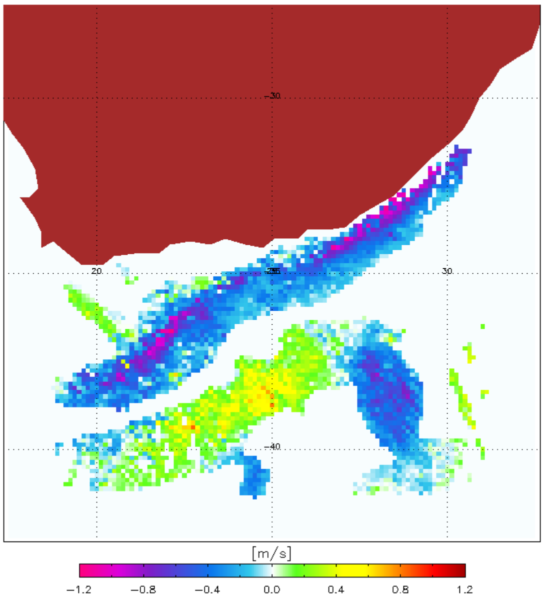

(d)

Figure 49: Masked average zonal (left) and meridional (right) velocities over the Agulhas Current area given by altimeters (top) and drifter (bottom)

The scatterplots corresponding to these maps are shown on **Figure 50**.

Aucune partie de ce document ne peut être reproduite sous quelque forme que ce soit, ni communiquée, ni utilisée, sans l'accord préalable de CLS.

Altimeter

Zonal

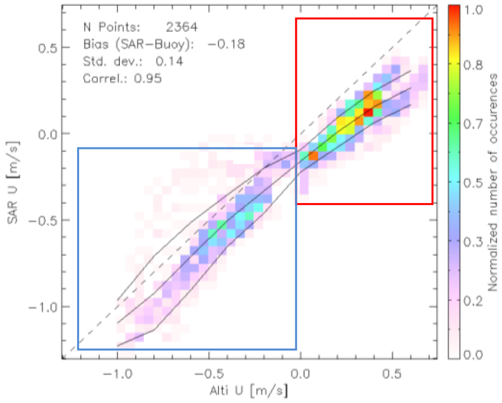

(a)

Meridional

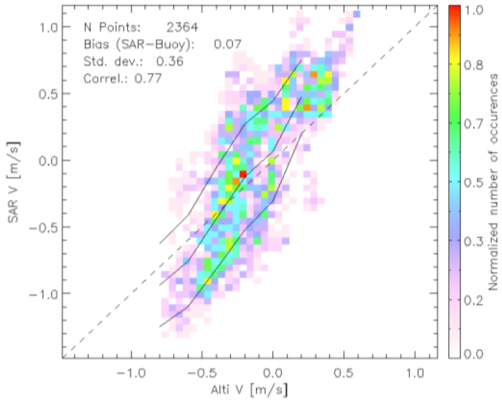

(b)

Drifters

Zonal

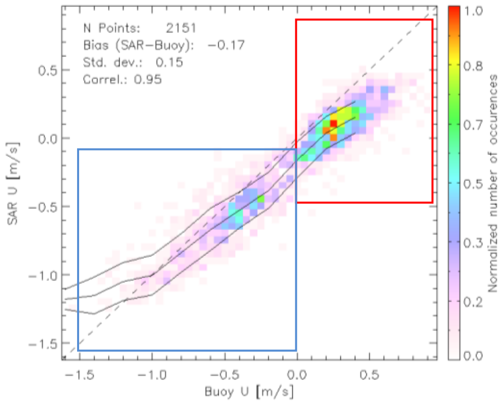

(c)

Meridional

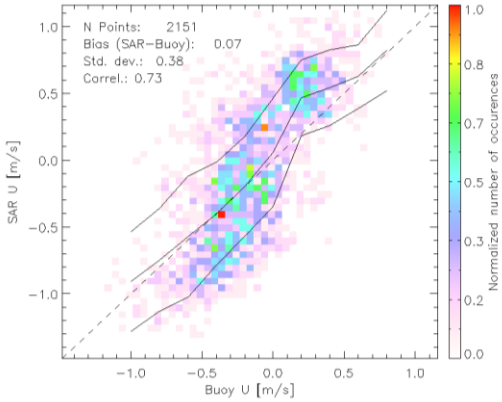

(d)

Figure 50: Scatterplots of masked zonal (left) and meridional (right) velocities over the Agulhas current area for SAR to altimeter measurements (top) and SAR to drifter measurements (bottom). The blue and red boxes have statistical characteristics corresponding to regions shown in Figure 48.

Aucune partie de ce document ne peut être reproduite sous quelque forme que ce soit, ni communiquée, ni utilisée, sans l'accord préalable de CLS.

Table 3: Statistics for the blue and red boxes for SAR vs. Altimeter and SAR vs. Drifter velocities in zonal component.

	Altimeter	Drifter
Points	1098	955
Bias	-0.11	-0.11
Std. Dev	0.15	0.15
Correlation coefficient	0.85	0.86

	Altimeter	Drifter
Points	1266	1196
Bias	-0.23	-0.22
Std. Dev	0.09	0.13
Correlation coefficient	0.86	0.70

From Table 3, it can be seen that

- First, the meridional velocity has a much worse correlation than the zonal component, which is expected given the geometry of the SAR sensor.
- Second, the SAR to drifter comparison and the SAR to altimeter comparison have very close biases and standard deviations. For the blue box, this is actually hiding two opposite behaviors: altimeter-derived measurements miss the general dynamic of the Agulhas main current. The bias is negative within the core of the current. However, because altimeter also misses the sharp current edge, there is a strong positive bias on the side of the main current. Since two biases have opposite signs, the total bias does not render the overall fit of the SAR to altimeter comparison.
- Third, the SAR to altimeter comparison gives a better correlation for the red box, of 0.86, compared to the 0.70 correlation for SAR to drifters comparison. This can partly be explained by the fact that the drifter measurements, even though they better assess the overall dynamic of the Agulhas current, have a larger spread than the altimeter, which is a rather smooth signal.

This methodology advantageously increases the number of samples used in the zonal estimation by combining the ascending and descending averages. The comparisons to altimeter and drifter-derived measurements show that the zonal component can be used to improve the dynamic of the altimeter signal and better image the high resolution patterns of the Agulhas current. Still, the meridional component, estimated using 150°-separated components, looks difficult to use judging by the bad correlation it presents compared to the zonal one.

5.3.4. Current velocity vector estimates using a combination of SAR and altimeter measurements - methodology

Here, we present a methodology in which the SAR measurements are combined with altimeter measurements. In the previously presented methodology, it appears inappropriate to reconstruct a SAR-derived current vector. Neither should the ascending and descending passes be used to infer the current direction. Instead, we now investigate the possibility to use the direction given by the altimeter measurements to modify the current velocity only. From the SAR-derived range velocities in ascending and descending passes (V_a^{SAR} and V_d^{SAR}), we can use the angle between the SAR range

Aucune partie de ce document ne peut être reproduite sous quelque forme que ce soit,
ni communiquée, ni utilisée, sans l'accord préalable de CLS.

direction and the altimeter-derived current direction for ascending and descending passes (β_a and β_d) to estimate the norm of the new altimeter current vector:

$$\overset{*}{V}_d = \frac{V_d^{SAR}}{\cos(\beta_d)}$$

$$\overset{*}{V}_a = \frac{V_a^{SAR}}{\cos(\beta_a)}$$

Several methods can then be used to combine these two different estimations of the vector norm. In our case, we have investigated two:

1. The vector norm is a linear combination of $\overset{*}{V}_d$ and $\overset{*}{V}_a$:

$$\overset{*}{V} = \frac{\overset{*}{V}_a \cos(\beta_a) + \overset{*}{V}_d \cos(\beta_d)}{\cos(\beta_a) + \cos(\beta_d)}$$

2. The vector norm is equal to the component for which the SAR range to altimeter current direction forms the smallest angle.

The 'updated' estimation of the current vector, $\overset{*}{V}$, is referred to as *synthetic* current vector. The standard deviation of the *synthetic* current vector is also estimated. It is impacted by two main parameters:

- The standard deviation of the SAR-derived range velocity in ascending and descending passes
- The standard deviation of the angle between the SAR range to altimeter current directions, which is here estimated considering the altimeter current direction variability.

For the ascending and descending components, the standard deviation of the *synthetic* current vector is estimated as follows:

$$\overset{*}{\sigma}_{a/d} = \left|\frac{\sigma_{a/d}^{SAR}}{\cos(\beta_{a/d})}\right| + \left|\frac{V_{a/d}^{SAR} \sin(\beta_{a/d})\sigma_\theta^{Alti}}{\cos^2(\beta_{a/d})}\right|$$

Where, $\sigma_{a/d}^{SAR}$ is the standard deviation of the SAR range velocity given for ascending (descending) passes,

$\beta_{a/d}$ is the angle between the SAR range direction for ascending (descending) passes and the altimeter-derived current direction,

$V_{a/d}^{SAR}$ is the SAR range velocity given for ascending (descending) passes.

σ_θ^{Alti} is the standard deviation of the altimeter-derived surface current direction,

Aucune partie de ce document ne peut être reproduite sous quelque forme que ce soit,
ni communiquée, ni utilisée, sans l'accord préalable de CLS.

Furthermore, we decided to limit the synthetic current estimates to regions where:

- The relative standard deviation is smaller than 250% : only regions where the current is relatively constant are then kept,
- The angle $\beta_{a/d}$ is smaller than 45° : this is to avoid the issues encountered in the previous section when estimating the meridional component of the current.

The standard deviation map and standard deviation map relatively to the synthetic current velocity are shown on **Figure 51**.

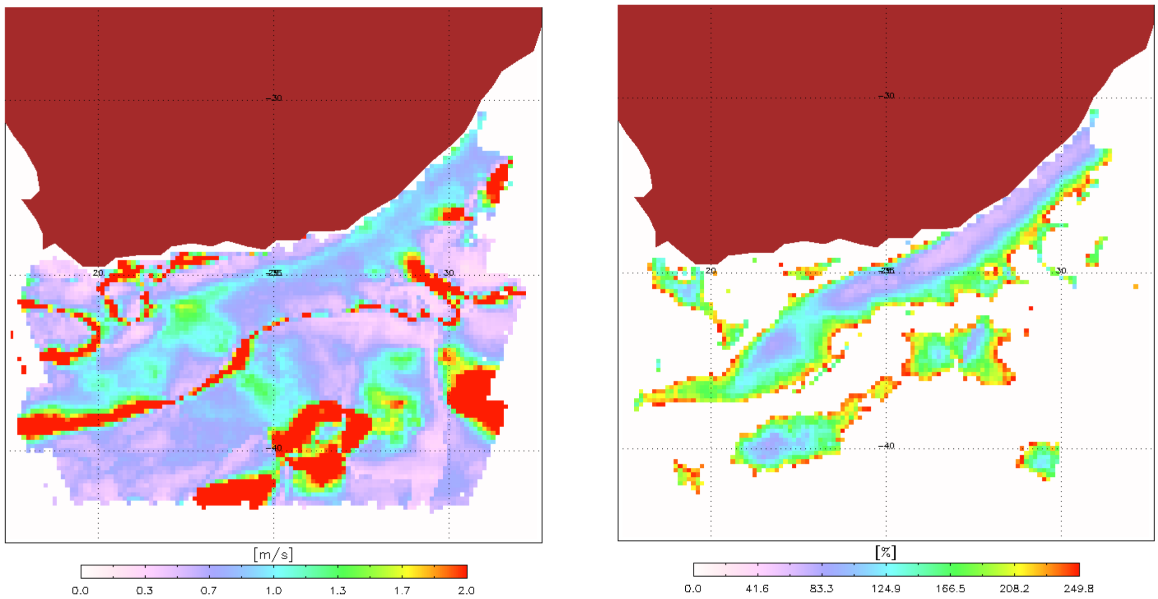

(a) (b)

Figure 51: Standard deviation (a) and Standard deviation relatively to the current velocity (b) of the synthetic current velocity estimated from the SAR ascending and descending passes combined with the altimeter-derived current direction

5.3.5. Current velocity vector estimates using a combination of SAR and altimeter measurements - results

On **Figure 52**, the synthetic current velocity map is plotted using method 2. Since differences between methods 1 and 2 are quite small, only the differences between method 1 and 2 are plotted on subplot (b).

Figure 53 shows the mean velocities from drifters (right) and altimeter (left). We see clearly the good consistency between SAR and drifter mean velocities and the less intense Agulhas current resolved by altimetry. There is therefore a strong potential in using these reconstructed SAR mean velocities for the calculation of regional high resolution MDT.

Aucune partie de ce document ne peut être reproduite sous quelque forme que ce soit,
ni communiquée, ni utilisée, sans l'accord préalable de CLS.

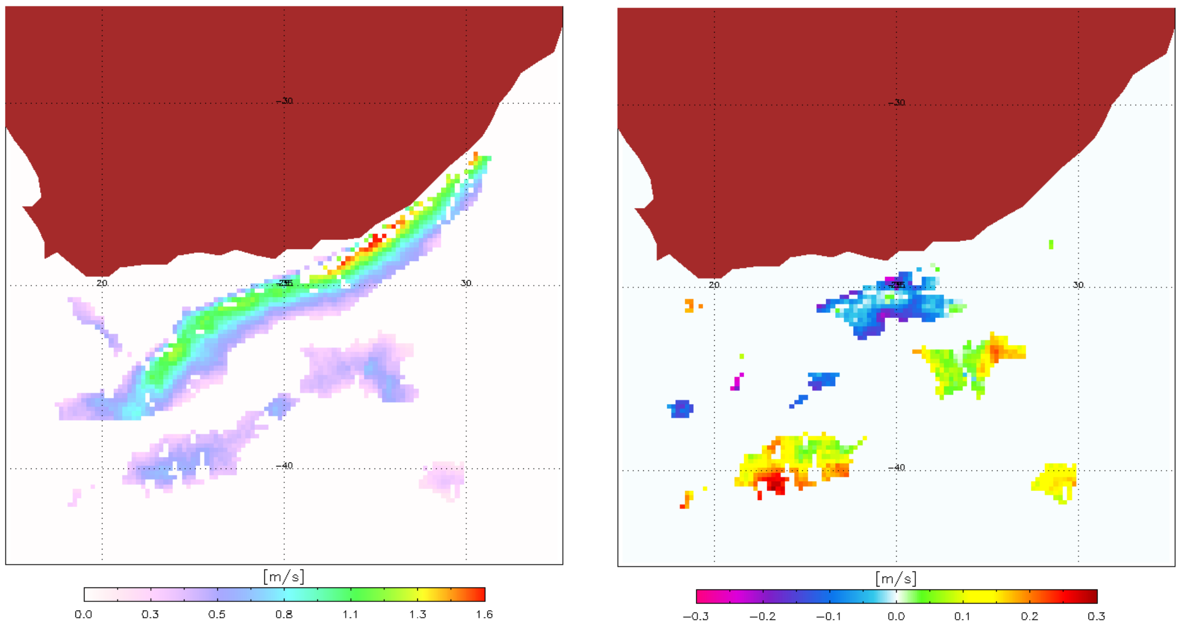

(a) (b)

Figure 52: Masked synthetic current velocity estimated from the SAR ascending and descending passes combined with the altimeter-derived current direction using method 2 (a). Subplot (b) presented the differences between method 1 and 2.

Altimeter Drifters

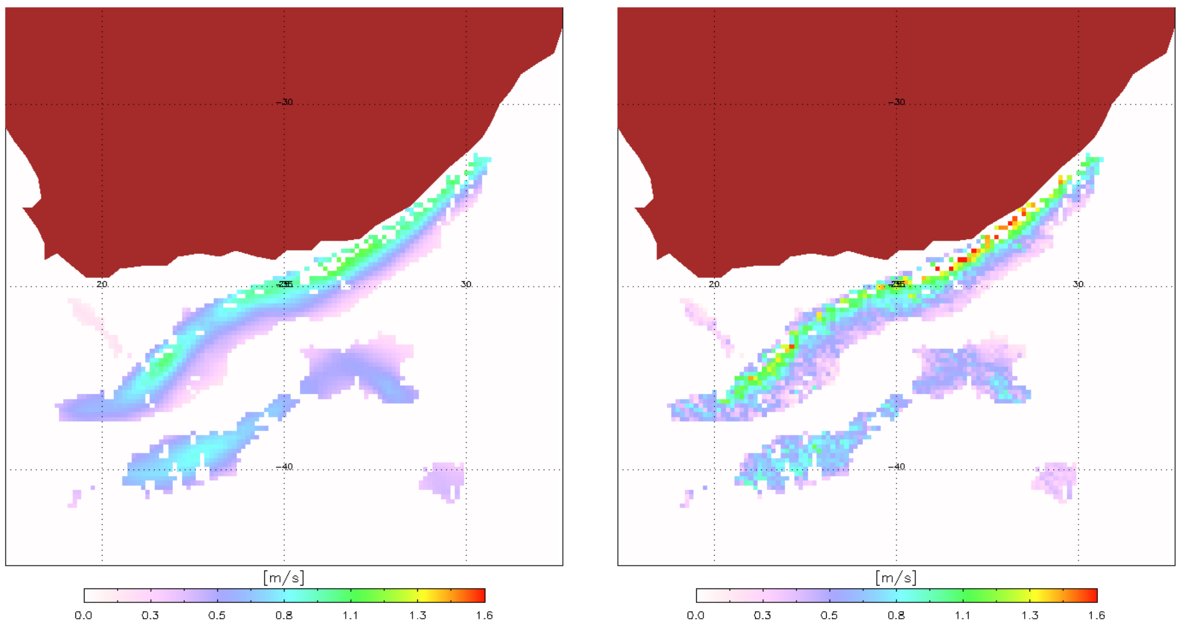

(a) (b)

Figure 53: Masked current velocity estimated from the altimeter (a) and the drifters (b).

Aucune partie de ce document ne peut être reproduite sous quelque forme que ce soit,
ni communiquée, ni utilisée, sans l'accord préalable de CLS.

The scatterplots for the corresponding zonal and meridional components of these maps are shown on **Figure 54**. Statistics for methods 1 and 2 are very close, but a little worse for method 1. For this reason, statistics and scatterplots are only given for the estimation of the synthetic current using method 2.

Altimeter

Zonal

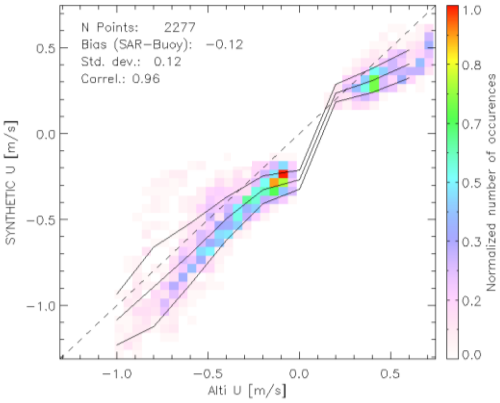

(a)

Meridional

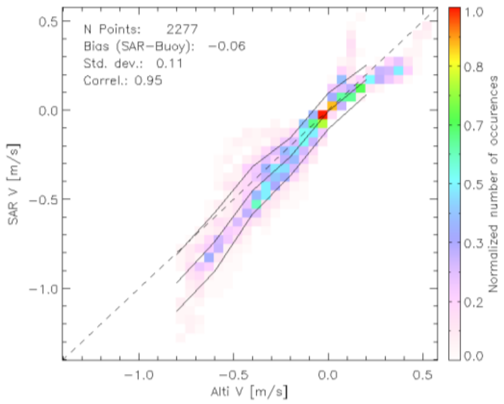

(b)

Drifters

Zonal

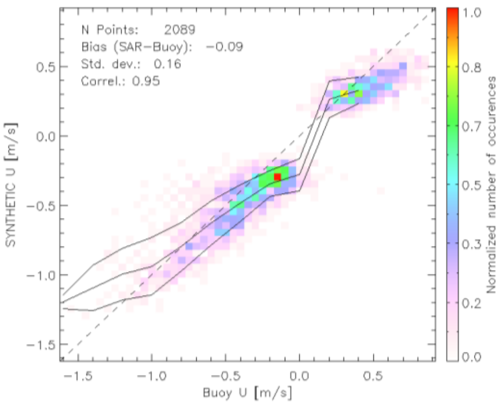

(c)

Meridional

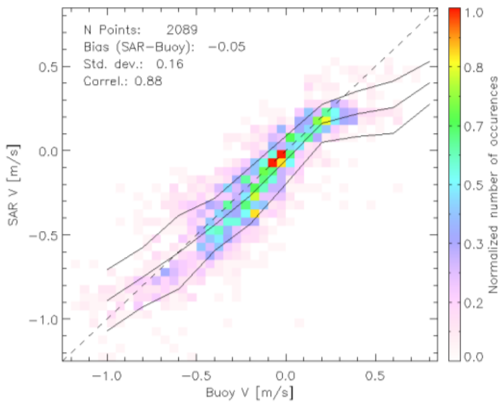

(d)

Figure 54: Scatterplots of masked zonal (left) and meridional (right) velocities over the Agulhas current area for Synthetic to altimeter-derived measurements (top) and Synthetic to drifter-derived measurements (bottom).

First, there is a great improvement of the meridional component estimation. The correlation coefficient respectively reaches 0.88 and 0.95 for drifters and altimeter measurements while it is equal to 0.77 and 0.73 when using the SAR measurements alone. Similarly, the standard deviation reaches 0.16 and 0.11 m/s for drifters and altimeter measurements while they are equal to 0.38 and 0.37 when using the SAR measurements alone.

Second, the estimation of the zonal component is also improved with respect to the first method using SAR measurements alone. Correlation and standard deviation are almost the same but the bias

Aucune partie de ce document ne peut être reproduite sous quelque forme que ce soit,
ni communiquée, ni utilisée, sans l'accord préalable de CLS.

is reduced considering both the altimeter and the drifters-derived measurements: from -0.18 to -0.12 m/s for altimeter and from -0.17 to -0.09 m/s for drifters.

This shows that the proposed combination method provides a better assessment of the Agulhas current full dynamic. Still, some discrepancies remain:

- The retroflection current is under-estimated by the synthetic current, as compared to the altimeter or the drifters-derived measurements.
- Even if the sharp edge of the Agulhas main current is well depicted by the synthetic current, the main stream is larger than what the drifters or the altimeter show.

5.4. Perspectives for regional MDT

In the present study, year-long averages of the SAR-derived range velocities have been used to estimate a mean surface geostrophic current to be compared to altimeters and drifters-derived geostrophic measurements.

The main issue for using the SAR Doppler velocities in the Agulhas current area is the reconstruction of the total vector current from radial velocities of the ascending and descending paths, which both resolve much better the zonal component than the meridional component of the velocity. A novel method has therefore been proposed where the altimeter direction is used together with the SAR-derived range velocity to estimate a synthetic current field. Results are quite promising. Still, in view of estimating a better resolved regional mean dynamical topography, several points shall be addressed:

- Large errors in the SAR-derived range velocities arise from the rain cells and inaccurate wind field hindcasts or forecasts at low radar incidence angles (less than 30°). Here, no measurements with incidence angles lower than 30° has been considered. On average, this reduces the bias in the zonal component of the synthetic current of 4 cm/s. Still, the presence of rain cells on the SAR images and the way it modifies the SAR-estimated surface wind field and then, the SAR-estimated range velocity has to be further investigated, as well as possible ways to filter them out.
- The tidal currents and the inertial oscillations that are part of the surface range velocities measured by SAR shall be removed using appropriate models.
- Finally, issues related to different time sampling have to be tackled by estimating daily synthetic currents. They shall then be integrated to collocated altimeter-derived velocity measurements and finally averaged over year-long periods.

As for the HF radar observing system, we expect the SAR velocities to highly contribute to regional MDT at resolutions of around 1/10° - 1/8° (the spatial resolution of SAR images being around 4-8 km).

Aucune partie de ce document ne peut être reproduite sous quelque forme que ce soit,
ni communiquée, ni utilisée, sans l'accord préalable de CLS.

6. References

Barrick DE (2008) 30 Years of CMTC and CODAR. In: Current measurement technology (2008). CMTC 2008. IEEE/OES 9th Working Conference on, Charleston, SC, 17–19 March 2008. pp 131–136. doi:10.1109/CCM.2008.4480856

Barrick D, Fernandez V, Ferrer M, Whelan C, Breivik O (2012): A short-term predictive system for surface currents from a rapidly deployed coastal HF radar network. Ocean Dyn. doi:10.1007/s10236-012-0521-0

Barrick DE, Lipa BJ (1996) Comparison of direction-finding and beam-forming in HF radar ocean surface current mapping. Phase 1 SBIR final report.National Oceanic and Atmospheric Administration, Rockville

Chaigneau, A., O. Pizarro, and W. Rojas (2008), Global climatology of near-inertial current characteristics from Lagrangian observations, Geophys. Res. Lett., 35, L13603, doi:10.1029/2008GL034060.

Chapman RD, Shay LK, Graber HC, Edson JB, Karachintsev A, Trump CL, Ross DB (1997): On the accuracy of HF radar surface current measurements: intercomparisons with ship-based sensors. J Geophys Res 102:18737–18748

Chapron, B., Collard, F. & Ardhuin, F., 2005. Direct measurements of ocean surface velocity from space: Interpretation and validation. Journal of Geophysical Research -- Oceans, 110(C9), p.7008-+.

F. Collard, A. Mouche, B. Chapron, C. Danilo, and J. A. Johannessen. Routine High Resolution Observation of Selected Major Surface Currents from Space. In Proceedings of SeaSAR 2008, 2008.

Crombie DD (1955) : Doppler spectrum of sea echo at 13.56 Mc./s. Nature 175:681–682
Barrick DE, Evans MW, Weber BL (1977) Ocean surface currents mapped by radar. Science 198(4313):138–144. doi:10.1126/science.198.4313.138

Ekman, V. W. 1905. On the influence of the Earth's rotation on ocean currents. Arch. Math. Astron. Phys., 2, 1-52.

Fu L., and E. Rodriguez, 2004. High-resolution measurement of ocean surface topography by radar interferometry for oceanographic and geophysical applications. The State of the Planet: Frontiers

Aucune partie de ce document ne peut être reproduite sous quelque forme que ce soit, ni communiquée, ni utilisée, sans l'accord préalable de CLS.

and Challenges in Geophysics, International Union of Geophysical Union, IUGG Geophysical Monograph, 338 Vol. 19, 209-224.

Graber, H. C., and B. K. Haus (1997): HF radar comparisons with moored estimates of current speed and direction: Expected differences and implications. J. Geophys. Res., 102 (C8), 18 749–18 766.

Gremes-Cordero, S., B. Haus, and H. Graber (2003): Determination of wind-driven coastal currents from local weather station. Geophys. Res. Abstracts, 5, 751.

Hansen, M.W. et al., 2011. Retrieval of Sea Surface Range Velocities From Envisat ASAR Doppler Centroid Measurements. IEEE Transactions on Geoscience and Remote Sensing, 49(10), pp.3582-3592.

Hansen, M.W., Kudryavtsev, V., et al., 2012. A Simulation of Combined Backscatter and Doppler Shifts of Wave-Current Interaction in the Presence of Strong Tidal Currents. Remote Sensing of the Environment.

Johannessen, J.A. et al., 2008. Direct ocean surface velocity measurements from space: Improved quantitative interpretation of Envisat ASAR observations. Geophysical Research Letters, 35, p.22608–+.

Kaplan D, Lekien F (2007): Spatial interpolation and filtering of surface current data based on open-boundary modal analysis. J Geophys Res 112(C12):C12007

Kim SY, Terrill E, Cornuelle B (2007) Objectively mapping HF radar derived surface current data using measured and idealized data covariance matrices. J Geophys Res 12(C6):C06021

Kohut JT, Glenn SM (2003): Improving HF radar surface current measurements with measured antenna beam patterns. J Atmos Ocean Technol 20(9):1303–1316

Kohut JT, Roarty HJ, Glenn SM (2006) : Characterizing observed environmental variability with HF Doppler radar surface current mappers and acoustic Doppler current profilers: environmental variability in the coastal ocean. IEEE J Ocean Eng 31(4):876–884

Kohut, J., Roarty, H.J., Rivera Lemus, E. (2009). Optimizing HF radar for SAR using USCG surface drifters and moored ADCPs. The 4th Radiowave Operators Working Group (ROWG) Meeting, Norfolk, VA.

Aucune partie de ce document ne peut être reproduite sous quelque forme que ce soit,
ni communiquée, ni utilisée, sans l'accord préalable de CLS.

Lipphardt, B.L., Kirwan, A.D., Grosch, C.E., Lewis, J.K. and Paduan, J.D. (2000). Blending HF radar and model velocities in Monterey Bay through normal mode analysis. Journal of Geophysical Research 105: doi: 10.1029/1999JC900295. issn: 0148-0227.

Mao and Heron (2008) : The Influence of Fetch on the Response of Surface Currents to Wind Studied by HF Ocean Surface Radar, JPO, DOI: 10.1175/2007JPO3709.1

Mouche, A.A. et al., 2012. On the Use of Doppler Shift for Sea Surface Wind Retrieval From SAR. IEEE Transactions on Geoscience and Remote Sensing, 50(7), pp.2901–2909.

O'Donnell J, Ullman DS, Spaulding M, Howlett E, Fake T, Hall P, Isaji T, Edwards C, Anderson E, McClay T, Kohut JT, Allen A, Lester S, Lewandowski M (2005) : Integration of Coastal Ocean Dynamics Application Radar (CODAR) and Short-Term Predictive System
(STPS) surface current estimates into the Search and Rescue Optimal Planning System (SAROPS). U.S. Coast Guard Research and Development Center, Washington.

Park, J.J., K. Kim, and B.A. King (2005), Global statistics of inertial motions, Geophys. Res. Lett., 32, L14612, doi:10.1029/2005GL023258.

Pujol, M., G. Dibarboure, P. Le Traon, and P. Klein, 2012: Using high resolution altimetry to observe mesoscale signals. J. Atmos. Oceanic Technol. doi:10.1175/JTECH-D-12-00032.1

Rascle, N. and F. Ardhuin (2013), A global wave parameter database for geophysical applications. Part 2: model validation with improved source term parameterization. Ocean Modelling 70 (2013) 174-188.

Rio, M. H., S. Guinehut, and G. Larnicol (2011), New CNES-CLS09 global mean dynamic topography computed from the combination of GRACE data, altimetry, and in situ measurements, J. Geophys. Res., 116, C07018, doi:10.1029/2010JC006505.

Rio, M-H, 2012: Use of altimeter and wind data to detect the anomalous loss of SVP-type drifter's drogue. Journal of Atmospheric and Oceanic Technology DOI:10.1175/JTECH-D-12-00008.1

Rio, M-H, S. Mulet, N. Picot (2014), Beyond GOCE for the ocean circulation estimate: Synergetic use of altimetry, gravimetry and in-situ measurements provides new insight into Geostrophic and Ekman currents. Geophysical Research Letter.

Aucune partie de ce document ne peut être reproduite sous quelque forme que ce soit,
ni communiquée, ni utilisée, sans l'accord préalable de CLS.

Roarty HJ, Glenn SM, Kohut JT, Gong D, Handel E, Rivera Lemus E, Garner T, Atkinson L, Jakubiak C, Brown W, Muglia M, Haines S, Seim H (2010) Operation and application of a regional high frequency radar network in the Mid Atlantic Bight. Mar Technol Soc J 44(6):133–145

J. Röhrs, A.Kristin Sperrevik, K. Håkon Christensen, G. Broström and O. Breivik (submitted) : Comparison of HF radar measurements with Eulerian and Lagrangian surface currents, Journal of Physical Oceanography

Rouault, M. et al., 2010. Mapping the Agulhas Current from Space: an assessment of ASAR surface current velocities. Journal of Geophysical Research, 115(C10026).

Stammer, D., et al. (2014), Accuracy assessment of global barotropic ocean tide models, Rev. Geophys., 52, 243-282, doi:10.1002/2014RG000450

Stokes, G. G. 1847, Trans. Cambridge Phil. Soc., 8, 441

Teague CC, Vesecky JF, Fernandez DM (1997) HF radar instruments, past to present. Oceanography 10(2):40–43

Ullman, D. S., J. O'Donnell, J. Kohut, T. Fake, and A. Allen (2006): Trajectory prediction using HF radar surface currents: Monte Carlo simulations of prediction uncertainties. J. Geophys. Res., 111, C12005, doi:10.1029/2006JC003715.

M. Yaremchuk and A. Sentchev (2009): Mapping radar-derived sea surface currents with a variational method, Continental Shelf Research 29,1711–1722

Aucune partie de ce document ne peut être reproduite sous quelque forme que ce soit,
ni communiquée, ni utilisée, sans l'accord préalable de CLS.